DETERMINATION OF CORRELATIONS INDUCED BY THE SENSE AND GRAPPA PMRI MODELS WITH AN APPLICATION TO MRI RF COIL DESIGN

by

Iain Peter Bruce, B.S., M.Sc.

A Dissertation submitted to the Faculty of the Graduate School,
Marquette University,
in Partial Fulfillment of the Requirements for
the Degree of Doctor of Philosophy

Milwaukee, Wisconsin

May, 2014

ABSTRACT
DETERMINATION OF CORRELATIONS INDUCED BY THE SENSE AND GRAPPA PMRI MODELS WITH AN APPLICATION TO MRI RF COIL DESIGN

Iain Peter Bruce, B.S., M.Sc.

Marquette University, 2014

Functional connectivity MRI is fast becoming a widely used non-invasive means of observing the connectivity between regions of the brain. In order to more accurately observe fluctuations in the blood oxygenation level of hemoglobin, parallel MRI reconstruction models such as SENSE and GRAPPA can be used to reduce data acquisition time, effectively increasing spatial and temporal resolution. However, the statistical implications of these models are not generally known or considered in the final analysis of the reconstructed data. In this dissertation, the non-biological correlations artificially induced by the SENSE and GRAPPA models are precisely quantified through the development of a real-valued isomorphism that represents each model in terms of a series of linear matrix operators. Using both theoretical and experimentally acquired functional connectivity data, these artificial correlations are shown to corrupt functional connectivity conclusions by incurring false positives, where regions of the brain appear to be correlated when they are not, and false negatives, where regions of the brain appear to be uncorrelated when they actually are. With a precise quantification of the artificial correlations induced by SENSE, a new cost function for optimizing the design of RF coil arrays has also been developed and implemented to generate more favorable magnetic fields for functional connectivity studies in specific brain regions. Images reconstructed with such arrays have an improved signal-to-noise ratio and a minimal SENSE induced correlation within the regions of interest, effectively improving the accuracy and reliability of functional connectivity studies.

ACKNOWLEDGMENTS

Iain Peter Bruce, B.S., M.Sc.

I would like to express my most sincere appreciation and thanks to my advisor, Dr. Daniel B. Rowe, for been such a remarkable mentor. You have provided the perfect balance of aid, guidance and encouragement for me to find it within myself to achieve my goals and establish myself as a scientist. The work outlined in this manuscript is testament to the remarkable collaboration that we established from my very first day.

I would like to thank Dr. L. Tugan Muftuler for the help and advice that he has given me throughout our work together. The approach that we developed together was very innovative and novel. I would also like to thank Dr. Gary S. Krenz, Dr. Stephen Merrill and Dr. Kristina M. Ropella for serving on my doctoral committee. Your words of advice and encouragement have actually made my dissertation defense an enjoyable experience, for which I am eternally grateful.

I owe my most heartfelt thanks to my family and friends. To Mom and Dad, throughout the best and worst of these five years, your daily support has never wavered. I can scarcely say that I would have reached this point without either of your encouragement. To my lab partners, M. Muge Karaman and Mary C. Kociuba, you two have offered tremendous support in working through both research and personal challenges throughout my time here at Marquette. I couldn't ask for two better people to share this experience with. Finally, I would like to thank Dr. Benjamin L. Brown. As my undergraduate advisor and mentor, you have always offered tremendous advice and guidance. If it were not for you, I would never have started this journey at Marquette.

TABLE OF CONTENTS

LIST OF TABLES

LIST OF FIGURES

Chapter 1: Introduction

Magnetic Resonance Imaging (MRI) is a radiological medical imaging technique that uses radiofrequency waves and magnetic fields to investigate the anatomical structure and functional activity of the human body. In neuroscience, MRI techniques provide a non-invasive means of observing the human brain in action without the need for surgery or exposing the subject to radiation. As with all medical imaging methodologies, the data acquired in an MRI scanner is both plagued by "noise" from various sources and can take an appreciable amount of time to be acquired. To alleviate the acquired MRI data of noise, neuroscientists have a great many image processing software packages at their disposal, and various techniques have been developed and incorporated into scanning protocols for accelerating the acquisition of MRI data. As it is only after a neuroscientist applies these tools to their data that a statistical analysis is performed, the underlying question upon which the work outlined in this dissertation is based is whether or not one can reap the benefits of such tools without suffering from the statistical implications that they may incur.

The work outlined in this dissertation is organized in five chapters. In the first chapter, a literature review is provided to outline the theory and background upon which this dissertation is based. To accelerate MRI data acquisition, SENSitivity Encoding (SENSE) (Pruessmann et al., 1999) and Generalized Auto-calibrating Partially Parallel Acquisition (GRAPPA) (Griswold et al., 2002) are the two most common parallel MRI (pMRI) techniques used in most medical MRI scanners. As such, the second and third chapters of this dissertation outline a novel method for precisely quantifying the statistical implications of the respective models using real-valued linear isomorphisms. In

both chapters, the theoretical correlations artificially induced by the SENSE and GRAPPA models are validated through both theoretical Monte Carlo simulations as well as experimentally acquired data. Given the previously unexplored correlation structure of the SENSE model outlined in the second chapter, the fourth chapter introduces a novel approach for designing phased arrays of radiofrequency coils that improve the statistical properties of SENSE imaging in specific brain regions. The final chapter summarizes the results obtained by the work outlined in this dissertation and projects the direction that this line of research could follow in the future.

1.1 Background

The discovery that magnetic field gradients can be used to encode the spatial information of an object in the resonance spectrum is the fundamental basis for image formation in MRI (Lauterbur, 1973; Haacke et al., 1999). While multiple mathematical basis sets exist to encode the spatial information of an object, Fourier encoding is by far the most prominent. When a real-valued object is placed into an MRI scanner, the magnetic field gradients Fourier encode the spatial information of the object into complex-valued spatial frequencies. When measurements of the spatial frequency domain (*k*-space) are acquired, additional factors such as magnetic field inhomogeneities (resulting from respiration, improper field shimming, etc.), transverse relaxation, and chemical shifts (Hahn et al., 2009; Hahn and Rowe, 2012; Hahn et al., 2012; Jezzard and Balaban, 1995) invoke a phase distortion that breaks the Hermitian symmetry of *k*-space. Although the object placed in the scanner is real-valued, the images of the object obtained by inverse Fourier reconstructing a *k*-space array without Hermitian symmetry become complex-valued, with both a magnitude and phase.

By collecting a time series of low-resolution complex-valued images in quick succession, one can observe changes in the blood oxygenation level dependent (BOLD) contrast, a metabolic correlate to neuronal activity (Ogawa et al., 1993). The BOLD contrast mechanism is the most commonly used form of contrast in mapping brain function and connectivity. The hemoglobin molecule in blood has different magnetic properties depending on whether or not it is bound to oxygen. When blood flows to different regions of the brain, the contrast between deoxygenated hemoglobin, which is paramagnetic, and oxygenated hemoglobin, which is diamagnetic, results in an observable change in the MR signal. This change is due to fluctuations in the bloods magnetic susceptibility, as indicated by the BOLD contrast mechanism (Ogawa et al., 1993).

1.1.1 Functional and Connectivity MRI

By tracking fluctuations in the BOLD contrast, functional MRI (fMRI) (Bandettini et al., 1993) and functional connectivity MRI (fcMRI) (Friston et al., 1993; Biswal et al., 1995) have become incredibly popular non-invasive means of observing both task related and spontaneous activity in the human brain. Functional studies investigate task related changes in the hemodynamic response that result from neuronal activity. When a human subject performs a task, the vascular system supplies glucose to the region of the brain associated with the task. The metabolic demands of the neuronal activity in this region results in an increased flow of oxygenated blood, thereby decreasing the magnetic susceptibility of the blood. This change is noted by a peak that forms in the BOLD signal for several seconds, before returning to a baseline level (Huettel & Song, 2008).

In fMRI, a time series of images is acquired while the subject alternates between laying at rest and performing a task in predefined intervals of time. As the BOLD signal's response to the stimulus is not instantaneous, the duration of the interval in which the subject performs the task is typically longer than the time it takes for the BOLD level to reach its peak, plateau, and drop off again. By repeating this process several times, an fMRI experiment tracks changes in the BOLD contrast in a time series of images using statistical models to develop maps of brain regions that are activated by the stimulus.

While the activity maps in fMRI are an innovative means of observing the regions of the brain that exhibit task related signal changes, they do not provide information on the relationship between brain regions, or connectivity. In fcMRI, a cross-correlation analysis is performed to determine which regions of the brain exhibit a correlation in low frequency BOLD activity over the course of a time series, even in the absence of the subject performing a task. Two regions that exhibit a correlation of this kind would suggest that the regions are functionally connected.

In recent years, both fMRI and fcMRI have become broadly recognized to have tremendous clinical advantages, effectively enabling neuroscientists to observe cognitive brain activity without the need for either surgery or subjecting patients to radiation. In 2009, the National Institute of Health granted more than $35m to sponsor the five-year Human Connectome Project (Sporns et al., 2006; Raichle et al., 2007; Jo et al., 2010; Deschpande et al., 2009) and, more recently in 2013, a $100m Brain Research through Advancing Innovative Neurotechnologies (BRAIN) Presidential initiative was unveiled. Both of these initiatives are aimed at better understanding the human mind, developing a

map of brain networks, and uncovering new means of treating degenerative brain disorders and traumatic brain injury. With such tremendous funding and effort devoted towards using techniques of this kind for observing cognitive brain activity, it is important to ensure that the models and tools developed to "improve" the quality of images do not inadvertently and unknowingly alter the statistical properties of the data.

1.1.2 MRI Data Acquisition

In an MRI scanner, a powerful superconducting magnet is used to align the magnetization of the hydrogen nuclei in the object being scanned. With the nuclei aligned in the same direction, radiofrequency (RF) pulses are emitted to the atoms in the object, effectively tipping the magnetic moment of the hydrogen nuclei into the transverse plane and causing the nuclei to precess around the alignment of the main magnetic field. The rate at which the nuclei re-align themselves with the main magnetic field is tissue dependent, and thus provides the contrast between tissues in the reconstructed images. Once the RF pulse excites the atoms in a typical MRI pulse sequence, magnetic field gradients are used to navigate through *k*-space such that spatial frequency measurements can be discretely recorded. While a variety of trajectories (such as a spiral or propeller) can be employed to shift through *k*-space, acquiring measurements along the way, the most typical method involves acquiring spatial frequencies on a Cartesian grid. Beginning in the lower left corner of the field of view (FOV) in Fig. 1.1a, the frequency encoding (FE) gradient moves the position in *k*-space from left to right until it reaches the right edge of the FOV, at which point the phase encoding (PE) gradient is applied to shift the position one increment towards the top. The FE gradient is then reapplied in the opposite direction, moving from right to left, and

this process is repeated until a complete array of spatial frequencies are acquired. Given the Fourier encoding nature of the gradients, an image of the object being scanned can be obtained by taking the inverse Fourier transform of the acquired spatial frequencies.

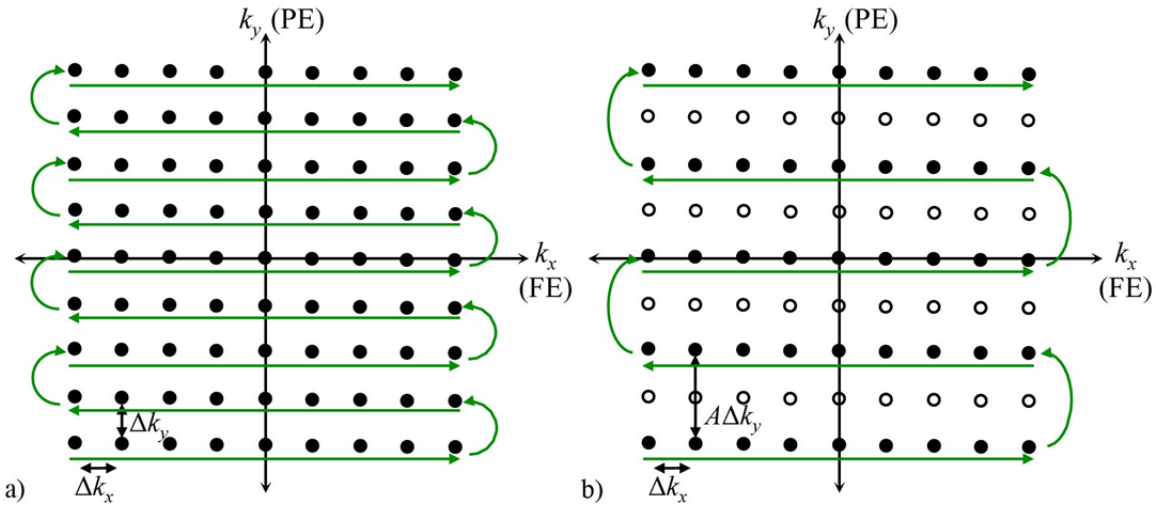

Figure 1.1: Acquisition of a) full *k*-space, and b) *k*-space sub-sampled by A=2 in the PE direction. Acquired frequencies are marked in black, while sub-sampled frequencies are marked in white.

One of the biggest hurdles faced in MR imaging is the fact that all spatial frequency measurements are not acquired instantaneously. The laborious process of Fourier encoding a volume in *k*-space takes an appreciable amount of time. In order to observe changes in the BOLD contrast most effectively, it is therefore imperative that data acquisition is performed in a minimal amount of time. It is for this reason that fMRI and fcMRI images are traditionally of a low resolution. The resolution of the reconstructed image is directly determined by the number of sampled frequencies, while the FOV in *k*-space is defined by the frequency range one can sample, which is in turn determined by the sampling rates in the k_x and k_y directions, Δk_x and Δk_y. In order to acquire a full FOV image, the Shannon-Nyquist sampling criteria requires that the

increments between measurements are $\Delta k_x \geq 1/(N_x \Delta x)$ and $\Delta k_y \geq 1/(N_y \Delta y)$, where N_x and N_y are the number of volume elements (voxels) in the x and y dimensions of the reconstructed image, and Δx and Δy are the dimensions of each voxel.

In a Cartesian acquisition of k-space, such as that in Fig. 1.1, the greatest amount of time is wasted in the application of the PE gradient. In order to shift one increment of Δk_y in the PE dimension, it can take on the order of 80% of the time it takes to acquire an entire line of k-space with the FE gradient. This is because the FE and PE gradients have to work together in switching the direction of the FE gradient, while simultaneously shifting upwards with the PE gradient. As such, it can be beneficial to minimize the number of PE steps required to traverse the FOV by skipping lines of k-space, thereby lowering the resolution of the reconstructed image in the y-dimension, as illustrated in Fig. 1.1b. The factor by which the PE dimension of k-space is sub-sampled is commonly referred to as the acceleration factor (or reduction factor), A. Sub-sampling by this factor effectively only acquires every A^{th} line, with each increment between acquired lines of $A\Delta k_y$, skipping the A-1 lines between acquired lines. The consequence of skipping A-1 lines of k-space is what is commonly referred to as aliasing. When a full FOV array of k-space is acquired, such as that in Fig. 1.2a, the result is a full FOV inverse Fourier reconstructed image. When the sub-sampling scheme in Fig. 1.1b is carried out with an acceleration factor of A=2, such as that in Fig. 1.2b, and by A=3, such as that in Fig. 1.2c, the reconstructed aliased images appear to be folded over on themselves A times (similar to a letter being folded to fit into an envelope) as a result of failure to meet the Shannon-Nyquist sampling criteria.

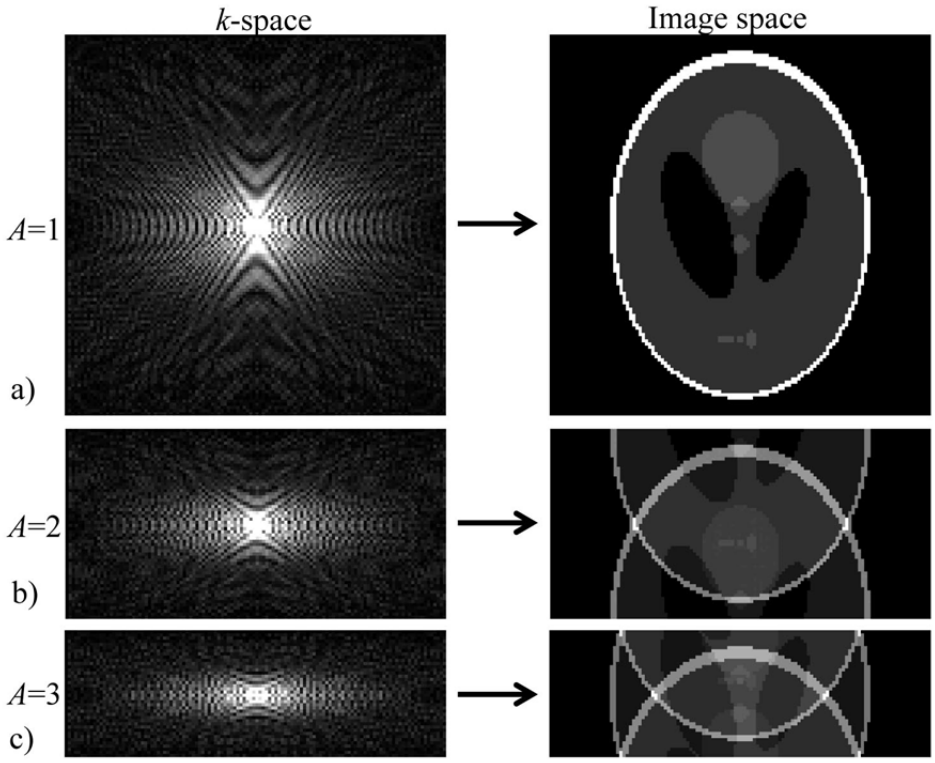

Figure 1.2: When *k*-space is a) fully sampled with *A*=1 the result is a full FOV image. When sub-sampled by b) *A*=2 and c) *A*=3, the result is an image that appears folded over on itself *A* times.

1.1.3 Parallel MRI

In many recent studies, great efforts have been spent on developing techniques for unfolding the aliased images that result from accelerated acquisitions of *k*-space using parallel MRI models. In pMRI, a phased array of multiple receiver coils is placed around the object in the scanner, and all receiver coils measure spatial frequencies concurrently after a single RF pulse excitation (Hyde et al., 1986; Roemer et al., 1990). As each receiver coil has a unique magnetic field (B-field), represented through a sensitivity profile that describes the B-field strength in the space surrounding the coil, the resulting aliased image acquired by each coil is locally weighted by the coil sensitivities. By acquiring spatial frequencies in all coils concurrently, one can therefore exploit the

overlap of the full FOV sensitivity profiles in the corresponding voxels in each aliased coil image and obtain an estimation of the unfolded and combined image. The un-aliasing of coil images can then be performed in either the image domain with techniques such as SENSE (Pruessmann et al., 1999), where the aliased coil images are "unfolded" into a single combined full FOV image, or in *k*-space with techniques such as SMASH (Sodickson & Manning, 1997), VD-AUTO SMASH (Heidermann et al., 2001) or GRAPPA (Griswold et al., 2002), where the missing spatial-frequency measurements are interpolated from the neighboring acquired frequencies.

1.2 Linear Image Reconstruction Framework

The ability to perform a complex-valued inverse Fourier reconstruction by means of a real-valued isomorphism, a process for performing a complex-valued operation through a mathematically equivalent real-valued operation, as derived in (Rowe & Logan, 2005; Rowe et al., 2007), paves the way for a statistical analysis of the pre-processing, post-processing, and image reconstruction operations performed on the acquired data. Consider a $p_y \times p_x$ matrix of two-dimensional complex-valued spatial frequencies, F_C, comprised of the sum of a true noiseless complex-valued spatial frequency matrix, F_{0C}, and a matrix of complex-valued measurement error, E_C, $F_C = F_{0C} + E_C$.

Since the spatial frequency array, F_C, is obtained by magnetic field gradients Fourier encoding the real-valued object placed in the MRI scanner, the reconstructed complex-valued image array, Y_C, is ideally derived through an inverse Fourier transform by

$$Y_C(q_x\Delta x, q_y\Delta y) = \sum_{q_y=-m}^{m-1}\sum_{q_x=-n}^{n-1} F_C(p_x\Delta x, p_y\Delta y)\exp\left(i2\pi\left(\frac{p_x q_x}{2n} + \frac{p_y q_y}{2m}\right)\right). \qquad [1.1]$$

Upon closer observation, the 2-dimensional inverse Fourier transform operation used to obtain the $p_x \times p_y$ reconstructed image, Y_C, in Eq. [1.1] is a linear operation in both the x and y dimensions. If indices j and k both vary from 1 to p_x, then the jk^{th} element of the inverse Fourier transform matrix in the x dimension, Ω_{xC}, can be expressed as

$$(\Omega_{xC})_{jk} = \exp\left(\frac{i2\pi}{p_x} + \left(j - \left(\frac{p_x}{2} + 1\right)\right) * \left(k - \left(\frac{p_x}{2} + 1\right)\right)\right),$$

and a similar inverse Fourier transform matrix can be expressed for the y dimension, Ω_{yC}, that is of dimension p_y (Nencka et al., 2009). With complex-valued inverse Fourier transform matrices,

$\Omega_{xC} = \Omega_{xR} + i\Omega_{xI}$, and $\Omega_{yC} = \Omega_{yR} + i\Omega_{yI}$,

the complex-valued inverse Fourier transformation of F_C in Eq. [1.1] can be written in matrix form as

$$Y_C = \Omega_{yC} F_C \Omega_{xC}^{T}. \qquad [1.2]$$

The inverse Fourier transformation of spatial frequencies used in Eq. [1.2] is illustrated in Fig. 1.3. When the inverse Fourier transform matrix for the vertical dimension, Ω_{yC}, in Fig. 1.3a pre-multiplies the complex-valued acquired spatial frequency array, F_C, in Fig. 1.3b, and is subsequently post-multiplied by the inverse Fourier transform matrix for the horizontal dimension, Ω_{xC}, in Fig. 1.3c, the result is the complex valued image space array, Y_C, in Fig. 1.3d.

For simplicity in representation, it can be shown that the pre- and post-multiplication of inverse Fourier matrices in Fig. 1.3 and Eq. [1.2] can be combined into a single reconstruction matrix,

$$\Omega = \begin{bmatrix} \Omega_R & -\Omega_I \\ \Omega_I & \Omega_R \end{bmatrix},$$

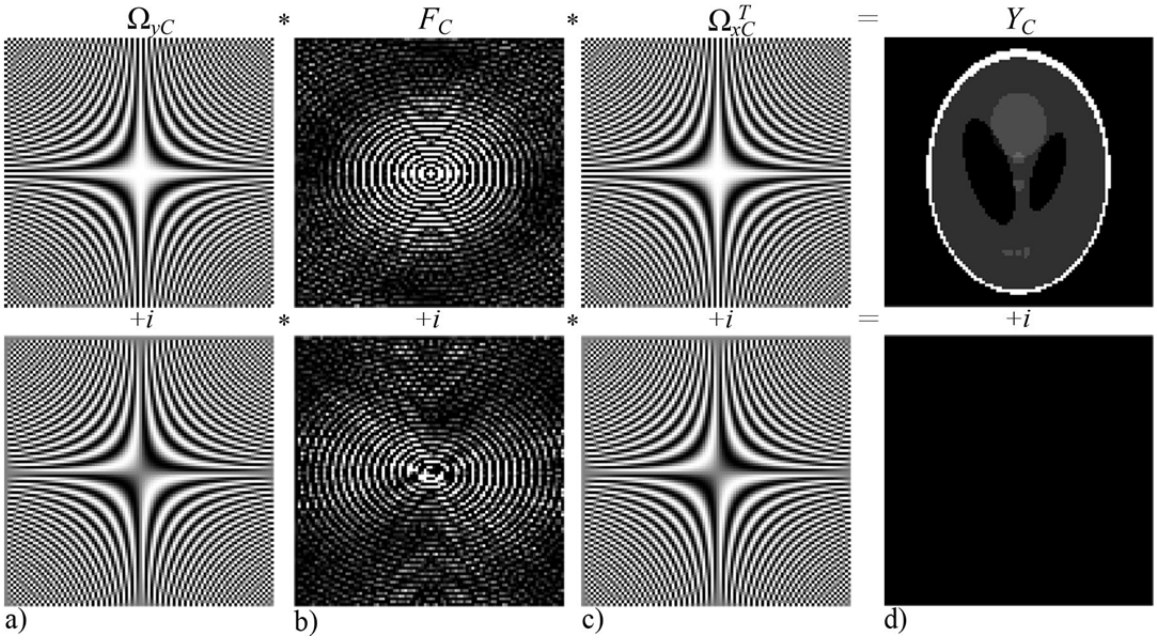

Figure 1.3: The real and imaginary components of a) the inverse Fourier transform in the *y* direction, Ω_{yC}, b) the spatial frequency array, F_C, c) the inverse Fourier transform in the *x* direction, Ω_{xC}, and d) the resulting image space array when multiplying $Y_C = \Omega_{yC} F_C \Omega_{xC}^T$.

where the real and imaginary components are formed using the Kronecker product, ⊗, by

$\Omega_R = [(\Omega_{yR} \otimes \Omega_{xR}) - (\Omega_{yI} \otimes \Omega_{xI})]$, $\Omega_I = [(\Omega_{yR} \otimes \Omega_{xI}) - (\Omega_{yI} \otimes \Omega_{xR})]$.

The Kronecker product operator, ⊗, multiplies every element of its first matrix argument by its entire second matrix argument. To use a single inverse Fourier transform operator, Ω, a vector of observed *k*-space spatial frequencies, *f*, is first formed by stacking the $p_x p_y$ real spatial frequencies on top of the $p_x p_y$ imaginary spatial frequencies,

$f = vec(\mathrm{Re}(F_C^T), \mathrm{Im}(F_C^T)) = f_0 + \varepsilon$,

where $vec(\cdot)$ is a vectorization operator that stacks the columns of its matrix argument, Re denotes the real part of F_C^T, and Im denotes the imaginary part of F_C^T. This vectorization therefore concatenates the rows of the real and imaginary matrices into separate vectors, which are in turn concatenated into a vector, *f*, of length $2p_x p_y$. As with F_C, *f* is the sum of a vector of true noiseless (complex-valued) spatial frequencies, f_0, and a vector of

(complex-valued) measurement error, ε. With the complex-valued spatial frequencies in a real-valued vector form, a real-valued image vector, y, is thus obtained by

$$y = \Omega f. \quad [1.3]$$

Similarly to the observed k-space data, if the complex-valued reconstructed image is of dimensions $p_y \times p_x$, then the reconstructed image vector, y, will consist of $p_x p_y$ real reconstructed voxel values stacked above $p_x p_y$ imaginary reconstructed voxel values, making the reconstructed image vector, y, in Eq. [1.3], of length $2p_x p_y$.

The advantage of representing Eq. [1.1] in terms of Eq. [1.3] is that it allows one to easily observe the exact linear combination of spatial frequency measurements in f that result in each reconstructed voxel value in y. While it can be shown that the formalism of the linear reconstruction operator, Ω, in Eq. [1.3] holds true for any linear reconstruction process (Hadamard, wavelet, singular value decomposition), the inverse Fourier transform is the most commonly used image reconstruction algorithm in MRI, and will therefore be utilized throughout the remainder of this dissertation. While not in the scope of this dissertation, the Ω operator can be adjusted to account for intra-acquisition decay (T_2^*) and magnetic field inhomogeneities (ΔB) acquired in the k-space signal if T_2^* or ΔB maps can be obtained (Nencka et al., 2009; Hahn et al., 2009).

1.2.1 Statistical Implications of Processing and Reconstruction Operations

If the spatial frequency vector, f, is comprised of real and imaginary values, with a covariance between the real measurements, between the imaginary measurements, and between the real and imaginary measurements, then an application of the inverse Fourier transform operator,

$$\begin{pmatrix} y_R \\ y_I \end{pmatrix} = \begin{bmatrix} \Omega_R & -\Omega_I \\ \Omega_I & \Omega_R \end{bmatrix} \begin{pmatrix} f_{0R} + \varepsilon_R \\ f_{0I} + \varepsilon_I \end{pmatrix}, \quad [1.4]$$

will result in an image vector, y, that is also comprised of real and imaginary values with a covariance between the real voxel values, between the imaginary voxel values, and between the real and imaginary voxel values. Eq. [1.4] lays the groundwork for the framework in A Mathematical Model for Understanding the STatistical properties (AMMUST) of pre- and post- reconstruction processing operations (Nencka et al., 2009) that is necessary to analyze the statistical implications of operations involved in image reconstruction for data that is fully sampled with a single receiver coil. If the observed k-space data vector, f, has a mean of $E[f]=f_0$ and a covariance represented by the matrix Γ, then the inverse Fourier reconstructed image vector, y, has a mean and covariance that are modified by the reconstruction operator, Ω, to become

$$E[y]=\Omega f_0 \text{ and } \text{cov}(y) = \Omega\Gamma\Omega^T. \quad [1.5]$$

If the vector f is $p_x p_y$ in length and assumed to have an identity covariance structure, $\Gamma=I$, the orthogonal nature of the Ω operator would simplify the covariance structure of the reconstructed image vector, y, in Eq. [1.5] to being an identity matrix scaled by the reciprocal of the length of f,

$$\text{cov}(y) = \Omega I \Omega^T = \frac{1}{p_x p_y} I. \quad [1.6]$$

In almost all fMRI and fcMRI studies, various pre- and post-processing operations are applied to the acquired data prior to statistical analysis. These processes are performed to alleviate the data of Nyquist ghosting, motion, respiration, nuisance signal from various tissue types (such as cerebral spinal fluid), and various other sources of artifacts. Irrespective of the type of operation being performed on the data, the

covariance structure of the processed data (which is observed in the statistical analysis) will not be the same as that of the un-processed acquired data. To observe the implications of either a single arbitrary processing or reconstruction operation, or a collection of operations, represented in matrix form, O, the reconstruction in Eq. [1.3] can be generalized by

$$y = Of. \quad [1.7]$$

Just as in Eq. [1.5], the mean of the vector y in Eq. [1.7] is $E[y]=Of_0$, and the covariance matrix of the vector f is modified by the operator, O, to become

$$\Sigma = \mathrm{cov}(y) = O\Gamma O^T. \quad [1.8]$$

In a conventional study on the analysis of image and signal processing, the covariance induced by the operator, O, would typically be estimated using Markov Chain Monte Carlo (MCMC) simulations (Barry & Strother, 2011; Strother, 2006; Della-Maggiore et al., 2009). As a heuristic rule, if the data vector f is $p_x p_y$ in length, these studies would simulate a time series with at least $10p_x p_y$ data vectors from which the covariance in Eq. [1.8] would be estimated. As the dimensions of f increase, this approach calls for an increasingly larger numbers of simulated data arrays to determine what is only an approximation of the true induced covariance structure. The formalism in Eq. [1.8], however, is able to determine the exact induced covariance structure directly, without the need to generate a single data vector. While the covariance of the originally acquired data vector, Γ, might only have a covariance between the real measurements and a covariance between the imaginary measurements, it is important to note that the covariance matrix, Σ, might also have a covariance between the real and imaginary (real/imaginary)

measurements that is induced by the operator O. Given the covariance structure in Eq. [1.8], the correlation structure between voxels is derived by

$$\text{corr}(\Sigma) = D_O^{-1/2} O \, \Gamma O^T D_O^{-1/2}, \qquad [1.9]$$

where $D_O = diag(\Sigma)$ is a diagonal matrix of the variances drawn from the diagonal of the covariance matrix in Eq. [1.8], and the -1/2 superscript denotes that the diagonal elements are inverted after taking the square root. With the real and imaginary components of vectors y and f stored in vectors of the form in Eq. [1.4], the real-valued representation of the correlation matrix produced by Eq. [1.9] can be partitioned into quadrants as

$$\text{corr}(\Sigma) = \begin{bmatrix} RR & RI \\ IR & II \end{bmatrix}, \qquad [1.10]$$

where the quadrant RR denotes the correlation between the real components of y, II denotes the correlation between the imaginary components of y, and $RI = IR^T$ denotes the correlations between the real and imaginary components of y. Any row, j, of the each quadrant in Eq. [1.10] represents the correlation between voxel j and all other voxels in the reconstructed image. The correlation about voxel j can thus be observed by partitioning the j^{th} row of each quadrant in Eq. [1.10] into p_x vectors of length $1 \times p_y$, each of which represent a column of the reconstructed image, stacking the row vectors into a matrix, and finally transposing.

Under the assumption of normality, the derivation outlined in the Appendices of (Nencka & Rowe, 2007) allows for the covariance structure of the square of magnitude-only data (magnitude-squared data) to be derived from the covariance matrix Σ in Eq. [1.8]. Magnitude-squared data is considered in the analysis of the covariance and correlation induced by operators involved in image reconstruction because an analytical solution exists for the linear framework in this dissertation, while magnitude-only data is

not considered because magnitude operations are not linear in nature. It can be shown that the correlation of magnitude-squared data is asymptotically equivalent to the correlation of magnitude-only data, and thus magnitude-squared data will be used along with complex-valued data to observe properties of real, imaginary, and real/imaginary correlation structures.

In many fMRI and fcMRI studies, data is first acquired by one person who can choose from a variety of acquisition and processing options available in the scanner's software. The data is then reconstructed and processed by another person who can choose between numerous software packages to try and rid the data of various types of noise and artifacts. Finally, inferences are made about the processed data (often by a third person) without taking into account the degree to which the true statistical properties of the acquired data have been changed by each process. In an attempt to draw statistical inferences about the originally acquired data from the reconstructed and processed data, an analyst would need to model data with considerably more complicated statistical properties than merely observing the statistical properties of the processed data. Recent studies, such as that by Nencka et al. (2009), have used the formalism in Eqs. [1.8]-[1.10] to quantify the degree to which various spatial processing operations modify the correlation structure of the original acquired data. These studies have shown that commonly used processing operations such as apodization in *k*-space and spatial filtering in image space induce local correlations between a voxel and its neighbors, while processes such as slice timing corrections can induce a correlation between voxels in different slices of a volume. These artificially induced correlations are of no biological

origin, and can therefore corrupt the statistical measures of the biological interpretations made in both fMRI and fcMRI studies.

While the use of pMRI models such as SENSE and GRAPPA offers a significant advantage in being able to increase spatial or temporal resolution by accelerating data acquisition, the degree to which these models alter the statistical properties of the acquired data have not been quantified. When each coil in a phased array acquires an aliased image, such as those in Fig. 1.4 for accelerations of A=2 and A=3, each aliased voxel value contains spatial information for voxels in all of the A folds of the image that are aliased in that location. This means that when the aliased voxels are un-aliased through either SENSE or GRAPPA, the voxels that were previously aliased will be correlated as a result of the un-aliasing process. Unlike the correlations induced by processes such as spatial filtering, where voxels become correlated with their neighbors, the SENSE and GRAPPA un-aliasing processes induce long-range correlations between different regions of the reconstructed images. Such correlations, which are artificial and of no biological origin, could potentially lead to Type I/II errors in fcMRI studies, where regions of the brain are assumed to be either correlated or uncorrelated with one another when they are not. As the statistical implications of the SENSE and GRAPPA models have not been previously explored, the work performed in this dissertation is aimed at developing linear isomorphic representations of each complex-valued model to precisely quantify the correlations induced in the images reconstructed by the respective model.

1.3 RF Coil Design for SENSE Imaging

The simultaneous acquisition of spatial frequencies in pMRI studies is typically performed using a phased array of surface coils, such as the array illustrated in Fig. 1.4.

Each surface coil in the array in Figs. 1.4a and 1.4b is comprised of a small loop of wire placed near the surface of the object being scanned and receives RF signals emitted by the spins of atomic nuclei that are in close proximity to the coil. The reception sensitivity of an RF coil can be deduced from the principle of reciprocity. With a current flowing through the wire loop, the B-field generated by the coil projects into the object with an effective depth of sensitivity that is proportional to the width of the coil, as illustrated in Fig. 1.4b. While the B-field for an individual surface coil is inhomogeneous throughout the volume being imaged, when multiple surface coils are phased together in an array there is a relatively homogeneous field generated by the array as a whole. It is this overlap of coil B-fields that allows for *k*-space to be sub-sampled concurrently by each coil, as the resulting aliased coil images can be un-aliased with models such as SENSE that use B-field sensitivity profiles for spatial localization.

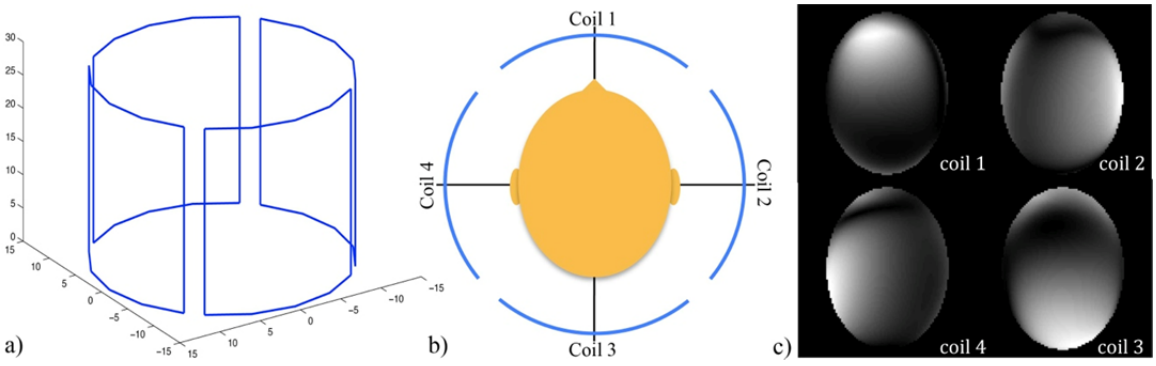

Figure 1.4: a) An array of N_C=4 rectangular coils b) placed around a human head, c) each with its own B-field sensitivity profile. Coil sensitivities are greatest in strength in the vicinity of the coil, shown in white, and decrease in strength with distance from the coil.

Unlike images derived from a full FOV acquisition of *k*-space, images reconstructed from accelerated acquisitions of *k*-space, using models such as SENSE, exhibit an inhomogenous noise distribution. This is a result of the inhomogeneous B-

field sensitivity profiles of the coils, used for spatial localization, when combined with the standard Fourier encoding performed by the magnetic field gradients. By comparison to a full FOV acquisition, pMRI techniques generally yield reconstructed images with a reduced signal-to-noise ratio (SNR). The ratio

$$\mathrm{SNR}_{SE} = \frac{\mathrm{SNR}_{full}}{g\sqrt{A}}. \qquad [1.11]$$

quantifies the loss in SNR in the SENSE reconstructed images, SNR_{SE}, by contrast to the SNR in images reconstructed from a fully sampled array of *k*-space, SNR_{full} (Pruessmann et al., 1999). If the full FOV $p_y \times p_x$ array of spatial frequencies, F_C, in Eq. [1.1] has an identity covariance structure prior to being inverse Fourier reconstructed, the covariance of the reconstructed image, Y_C, is equivalent to that of F_C, scaled by $1/p_y p_x$. Therefore, when a $(p_y/A) \times p_x$ sub-sampled array of spatial frequencies is inverse Fourier reconstructed, the resulting covariance is scaled by a factor of $A/p_y p_x$. Since SNR is typically the ratio of the magnitude and standard deviation, the SNR_{SE} therefore becomes inversely proportional to the square root of the acceleration factor by which *k*-space was sub-sampled, and consequently SNR_{SE} is also inversely proportional to the data acquisition time. The additional factor *g* in the denominator of Eq. [1.11] is commonly referred to as the geometry-factor (or *g*-factor). For a collection of N_C receiver coils, such as those in Fig. 1.4a, each with a unique B-field profile, the *g*-factor represents the amplification of noise (standard deviation) in each voxel of the un-aliased SENSE reconstructed image that results from the overlap of coil B-fields in Fig. 1.4c. The B-field sensitivities in Fig. 1.4c are greatest in strength in the vicinity of each coil (illustrated in white), and decrease in strength with distance from the coil. For a voxel in which there is no aliasing, there is no amplification of noise, and thus the *g*-factor is one. For voxels that

experience aliasing with multiple regions of the object being scanned, the measurement noise (the denominator of SNR) in the un-aliased voxels is scaled by $g>1$. As this amplification of noise arises from an overlap of the coil B-fields, the *g*-factor has become the de facto metric used in the assessment of parallel RF coils designed for SENSE imaging, especially when a high SNR is needed in a particular region of interest (ROI).

1.3.1 Methods of RF Coil Design

In an ideal situation, a phased array of RF surface coils would be comprised of independent receiver coils with sensitivity profiles that neither overlap nor decrease in strength with distance from the coil (i.e. similar to that of a pie with wedge slices of equal size and constant throughout). While such an array would result in a *g*-factor of one in every voxel, this coil arrangement is virtually impossible to achieve. Coil B-fields will therefore always have some level of overlap in order to obtain an image, reconstructed with the SENSE model, that exhibits a uniform signal intensity throughout. In recent years, many studies have therefore been aimed at improving SENSE reconstructed images through advancements in hardware. Until recently, most approaches have been characterized as direct methods, in which several coil configurations are defined, and the arrangement that yields the best *g*-factor in a ROI is selected (Weiger et al., 2001; Zwart et al., 2002). While this approach could progressively produce better and better arrays, through multiple iterations of designs, the probability of achieving an optimal design is low. Alternatively, recent studies have described each coil in the array by a collection of connected vertices in a 3-dimensional space, and performed brute-force methods through simulated annealing to systematically shift the vertices, thereby varying the size and shape of each coil. For each coil configuration, the SNR in a ROI is estimated and the

arrangement with the highest SNR is considered as the optimal coil layout. This approach offers greater potential for achieving an optimal layout than the initial trial and error methods, but could be very time consuming to appropriately simulate as many coil geometries as possible, while accurately simulating the B-fields for each geometry.

The most promising methods of determining optimal RF coil designs in recent years have adopted an inverse approach that is predicated on the fact that the SNR in an ROI is directly determined by the distribution of coil B-fields in that region. By establishing a desired distribution of the B-fields in the ROI, early methods aimed to solve the inverse problem of determining the surface current distribution necessary to generate the desired distribution (Lawrence et al., 2002; Xu et al., 2005). Using a finite element analysis, the optimal current density distribution for a coil can be determined using a least squares approach to minimize a cost function, such as the *g*-factor or $1/SNR_{SE}$ (Muftuler et al., 2005). Once the optimal surface current distribution that achieves maximal SNR_{SE} is defined, an RF coil design is then determined that will produce the desired distribution. A disadvantage of this approach lies in the potential for complicated and unrealistic coil designs in order to achieve the desired current distribution. In more recent studies, such as those by Chen et al. (2007), the geometry of a supplemental RF coil array was modeled by a set of connected conductor segments, with each coil in the shape of a butterfly. The SNR_{SE} was then formulated as a function of the coil vertices, and a least squares estimation was performed to determine the optimal vertex locations that would define an array with a minimal cost function and in turn a maximal SNR_{SE}.

1.3.2 The Limitations of Current RF Coil Designs

In both fMRI and fcMRI studies, the same generic RF coil arrays are often used for imaging all regions of the brain. Most typically, "birdcage" arrays with rectangular coil elements, such as the array in Fig. 1.4a, are used. These arrays are radially symmetric, from back to front, from left to right, and from top to bottom. The resulting B-fields generated by such a symmetric array are relatively homogeneous in the center of the volume. As the human brain is not fully symmetric, and ROIs are not typically in the very center, using the same coil for all regions may not be beneficial. As the overlap of coil B-fields is unavoidable in order to achieve a reconstructed image with a uniform signal distribution, there will always be areas in which the noise is amplified, as measured through the *g*-factor. If a conventional birdcage array of rectangular coils is used for acquiring images in all studies, these areas with a high *g*-factor will always be in the same spatial location. By changing the geometry of an RF coil array when imaging a specific ROI, however, these areas with a high *g*-factor could be strategically relocated such that they are not within the ROI. For studies such as fMRI and fcMRI, where constraints are placed on spatial and temporal resolutions, the accelerations in data acquisition that can be achieved through pMRI techniques can be combined with purpose build hardware that minimizes the amplification of noise and artifacts in a particular ROI of the reconstructed images. With the incredible amount of both funding and effort being devoted towards fMRI and fcMRI studies for specific degenerative brain disorders (commonly associated with specific brain regions), the notion of RF coil arrays purpose built for imaging specific brain regions makes sense. Depending on the location of the ROI, asymmetric coil geometries that have elements with variable sizes and shapes, and

are designed to work in conjunction with a custom MRI pulse sequence, could achieve a more optimal *g*-factor within a ROI. As the B-fields of a coil geometry designed for a scanner with one magnetic field strength will behave differently when placed in a scanner with a different field strength (Wang, 2012), ROI specific coil geometries would have to be determined to achieve the same statistical properties and *g*-factor for each field.

In many studies (Muftuler et al., 2006; Muftuler et al., 2009; Chen et al., 2007), the optimization of RF coil design using the *g*-factor as a metric has proved to be a beneficial means of achieving higher SNR values in a ROI of the reconstructed image. However, while the *g*-factor represents the amplification of noise (standard deviation) in each voxel, it does not provide a measure of the correlations induced between the voxels in the ROI and the voxels previously aliased with the ROI prior to a SENSE reconstruction. In a coil design study, it is therefore not sufficient to only align the elements of the array in such a way that the *g*-factor in the ROI is minimal. While this would provide a uniform distribution of the noise in the ROI, if a region of the object being scanned that was previously aliased with the ROI has a *g*-factor that is significantly greater than that of the ROI, the amplified noise that results from the overlap of coil B-fields in that region will be correlated with the ROI through the SENSE reconstruction process. As such, the optimization criteria used in designing an RF coil array for SENSE imaging would be more appropriately defined to incorporate both the traditional *g*-factor metric, as well as a measure of the correlations induced between the ROI and other voxels in a SENSE reconstructed image.

Chapter 2: A Statistical Investigation of the SENSE pMRI Model

2.1 The SENSE Model

The SENSE model is characterized as an image space model because it performs the unfolding of aliased coil images in the image domain after the accelerated arrays of *k*-space from each of N_C receiver coils are inverse Fourier reconstructed. Consider a collection of full FOV B-field sensitivities for N_C=4 receiver coils in Fig. 2.1a, with corresponding aliased coil images acquired with an acceleration factor of A=3 by each coil in Fig. 2.1b. The underlying assumption of the SENSE model is that every complex-valued aliased voxel, j, in each of the N_C aliased coil images in Fig. 2.1b, $a_{jC} = a_{jR} + ia_{jI}$, is a sensitivity weighted linear combination of the A true un-aliased voxel values in Fig. 2.1c, $v_{jC} = v_{jR} + iv_{jI}$, with added measurement error, $\varepsilon_{jC} = \varepsilon_{jR} + i\varepsilon_{jI}$,

$$a_{jc} = S_{jC}\, v_{jC} + \varepsilon_{jC}. \qquad [2.1]$$

Illustrated for an arbitrary voxel, j, the sub-scripts of the sensitivities in Fig. 2.1a represent the coil and aliased fold indices in the matrix S_{jC}, the sub-scripts for the aliased voxel values in Fig. 2.1b indicate the coil index in the vector a_{jC}, and the sub-scripts in Fig. 2.1c represent the fold of the un-aliased image vector, v_{jC}. The spatial localization matrix, $S_{jC} = S_{jR}+iS_{jI}$, in Eq. [2.1] is an $N_C \times A$ array in which each of the N_C rows are comprised of the A fully sampled complex-valued coil sensitivities from each of the N_C=4 coils in Fig. 2.1a. It is generally assumed that the complex-valued measurement noise, ε_{jC}, is derived from the complex-valued normal distribution (Wooding, 1956), given by

$$f(\varepsilon_{jC}) = (2\pi)^{-N_C} \left|\Psi_C\right|^{-1/2} \exp\left(-\frac{1}{2} \varepsilon_{jC}^H \Psi_C^{-1} \varepsilon_{jC} \right),$$

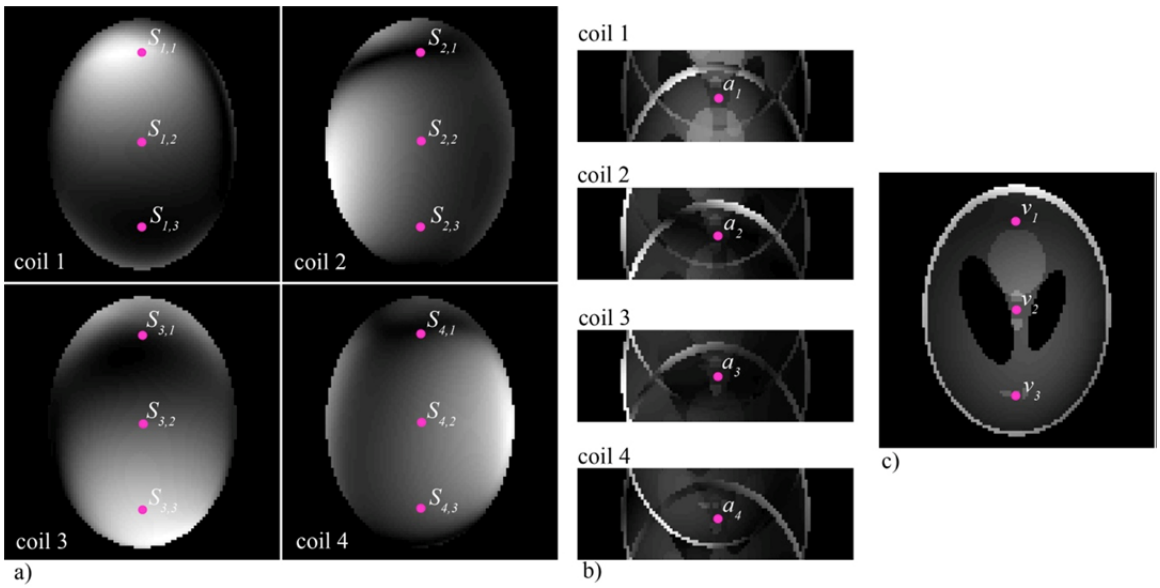

Figure 2.1: As performed in the SENSE model, a) full FOV coil sensitivities are used to un-alias the b) aliased coil images from N_C=4 coils, sub-sampled by A=3, to reconstruct c) a single un-aliased image.

where $\Psi_C = \Psi_R + i\Psi_I$ is the complex-valued coil covariance matrix and H denotes the Hermetian, or conjugate transpose. Derived through a change of variables from the distribution of ε_{jC}, the distribution of the complex-valued vector of sub-sampled spatial frequencies, a_{jC}, in Eq. [2.1] also has a complex-valued normal distribution

$$f(a_{jC}) = (2\pi)^{-N_C} \left|\Psi_C\right|^{-1/2} \exp\left[-\frac{1}{2}(a_{jC} - S_{jC}v_{jC})^H \Psi_C^{-1}(a_{jC} - S_{jC}v_{jC})\right].$$

Under the assumption of normality, the maximum likelihood estimates of the complex-valued un-aliased voxel values can therefore be derived using a complex-valued weighted least-squares estimation by

$$v_{jC} = (S_{jC}{}^H \Psi_C{}^{-1} S_{jC})^{-1} S_{jC}{}^H \Psi_C{}^{-1} a_{jC}. \qquad [2.2]$$

Through the complex-valued weighted least squares estimation in Eq. [2.2], the A un-aliased voxel values are derived from aliased voxel values acquired from the N_C coils.

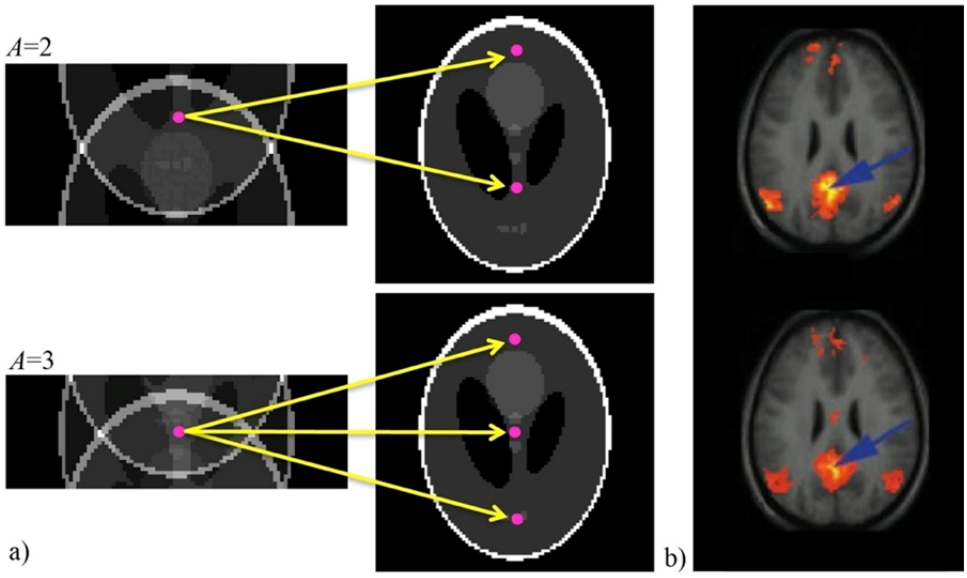

Figure 2.2: a) The non-biological correlations artificially induced by the SENSE un-aliasing process with A=2 and A=3 share the same spatial locations with b) biological correlations denoting the Default Mode Network derived through an fcMRI study (Greicius et al., 2003), (Copyright (2003) National Academy of Sciences, U.S.A).

As shown for acceleration factors of A=2 and A=3 in Fig. 2.2a, the complex-valued weighted least squares estimation of the un-aliased voxel values in Eq. [2.2] effectively converts a single value in each of the N_C aliased coil images into A un-aliased values. By definition, such an un-aliasing process would therefore be expected to artificially induce a correlation between the A un-aliased voxels. The figure presented in Fig. 2.2b was drawn from a study by Greicius et al. (2003) that observed functional connectivity in both the resting and active brain. The correlations in Fig. 2.2b are of a true biological origin and represent a very commonly investigated network of functional connections within the brain known as the "Default Mode" (Raichle et al, 2001; Raichle et al., 2007). Upon observation, the artificially correlated voxels un-aliased by the SENSE model in Fig. 2.2a share the same spatial locations as the truly correlated voxels of the Default Mode Network in Fig. 2.2b. If a statistical analysis were to be conducted

on SENSE reconstructed images, without accounting for such correlations, it would be impossible for one to know whether or not the correlations observed in the fcMRI data were of a true biological origin or artificially amplified or diminished by the SENSE induced correlations. For this reason, the remainder of this chapter presents a means of precisely quantifying the non-biological correlations artificially induced by SENSE through a real-valued isomorphism, with the implications of the artificial correlations validated by both theoretical and experimental illustrations.

2.2 The SENSE Isomorphism

In this section, an isomorphic representation of the complex-valued SENSE model is presented to un-alias all voxels from the N_C aliased coil images at once using real-valued matrix operators. Representing the complex-valued SENSE un-aliasing process with a single real-valued matrix operator enables one to observe the precise linear combination of the sub-sampled spatial frequencies acquired by the N_C receiver coils that formed each voxel in the un-aliased image. Furthermore, with a real-valued matrix operator, the way in which the covariance and correlation structure of the acquired data is altered by the SENSE model can be precisely quantified using the formalism in Eqs. [1.8] and [1.9], without the need for time consuming Monte Carlo simulations that are only able to approximate the structure of the induced correlation.

2.2.1 Real-Valued SENSE Model

For a single aliased voxel j, the complex-valued SENSE model in Eq. [2.1] can be equivalently expressed as a real-valued isomorphism by

$$\begin{bmatrix} a_{jR} \\ a_{jI} \end{bmatrix} = \begin{bmatrix} S_{jR} & -S_{jI} \\ S_{jI} & S_{jR} \end{bmatrix} \begin{bmatrix} v_{jR} \\ v_{jI} \end{bmatrix} + \begin{bmatrix} \varepsilon_{jR} \\ \varepsilon_{jI} \end{bmatrix}, \text{ or } a_j = S_j v_j + \varepsilon_j. \quad [2.3]$$

In Eq. [2.3], the vector a_j is comprised of the vector of N_C real aliased voxel measurements stacked upon the vector of N_C imaginary aliased voxel measurements, the vector v_j is comprised of the A real true un-aliased voxel values stacked upon the A imaginary true un-aliased voxel values, and the vector ε_j is comprised of the N_C real parts of the complex-valued additive noise stacked upon a vector of the N_C imaginary parts of the complex-valued additive noise. When the product $S_{jC}\, v_{jC} = (S_{jR}+iS_{jI})(v_{jR}+iv_{jI})$ in Eq. [2.1] is expanded and expressed in terms of a real-valued isomorphism, the spatial localization matrix, S_j, in Eq. [2.3] takes on the skew symmetric form,

$$S_j = \begin{bmatrix} S_{jR} & -S_{jI} \\ S_{jI} & S_{jR} \end{bmatrix}. \quad [2.4]$$

Using the real-valued isomorphism in Eq. [2.3], the complex-valued multivariate normal distribution of the vector of aliased voxel values, a_j, can be expressed as the $2N_C \times 1$ real-valued multivariate normal distribution of coil measurements by

$$f(a_j) = (2\pi)^{-N_C} \left|\Psi\right|^{-1/2} \exp\left[-\frac{1}{2}(a_j - S_j v_j)^T \Psi^{-1} (a_j - S_j v_j) \right].$$

As the additive measurement noise, derived from the complex-valued normal distribution (Wooding, 1956),

$\varepsilon_{jC} \sim CN(0, \Psi_C)$,

provides the covariance between the coils in the SENSE model, when represented as a real-valued isomorphism,

$$\varepsilon_j \sim N\left(0, \begin{bmatrix} \Psi_{RR} & -\Psi_{II} \\ \Psi_{II} & \Psi_{RR} \end{bmatrix} \right),$$

the real-valued representation of the complex coil covariance matrix, as used in the SENSE model, takes on the skew-symmetric form

$$\Psi = \begin{bmatrix} \Psi_{RR} & -\Psi_{II} \\ \Psi_{II} & \Psi_{RR} \end{bmatrix}. \qquad [2.5]$$

It is of note that when a covariance between coils is estimated from experimentally acquired complex-valued aliased voxel values organized with the real component stacked upon the imaginary component, such as a_j in Eq. [2.3], there is an estimated covariance between the real components, Ψ_{RR}, between the imaginary components, Ψ_{II}, and between the real and imaginary components of the coil measurements, Ψ_{RI}, that are ordered by

$$\hat{\Psi} = \begin{bmatrix} \Psi_{RR} & \Psi_{RI} \\ \Psi_{IR} & \Psi_{II} \end{bmatrix}.$$

What Eq. [2.5] therefore implies is that the complex-valued application of the SENSE model imposes a skew-symmetric covariance structure between coils, where the real/imaginary covariance between coils is equated to be the negative of the imaginary covariance, and that the imaginary coil covariance is equated to that of the real coil covariance. The validity of this assumption is explored further in Appendix A. In many studies, Ψ_C (and hence Ψ) is treated as a real-valued identity matrix, however, it will be shown in both the illustrations in this chapter and in Appendix A that when the covariance between coils is estimated from experimentally acquired data, the structure is far from an identity matrix (Bruce et al., 2011; Bruce et al., 2012).

Provided with the real-valued isomorphism representation of the complex-valued coil sensitivities matrix in Eq. [2.4] and the real-valued isomorphism representation of the complex-valued coil covariance matrix in Eq. [2.5], the SENSE estimator for the un-

aliased voxel values in Eq. [2.2] can be equivalently expressed as a real-valued isomorphism by

$$\begin{bmatrix} v_{jR} \\ v_{jI} \end{bmatrix} = \left(\begin{bmatrix} S_{jR} & -S_{jI} \\ S_{jI} & S_{jR} \end{bmatrix}^T \begin{bmatrix} \Psi_{RR} & -\Psi_{II} \\ \Psi_{II} & \Psi_{RR} \end{bmatrix}^{-1} \begin{bmatrix} S_{jR} & -S_{jI} \\ S_{jI} & S_{jR} \end{bmatrix} \right)^{-1} \cdot \begin{bmatrix} S_{jR} & -S_{jI} \\ S_{jI} & S_{jR} \end{bmatrix}^T \begin{bmatrix} \Psi_{RR} & -\Psi_{II} \\ \Psi_{II} & \Psi_{RR} \end{bmatrix}^{-1} \begin{bmatrix} a_{jR} \\ a_{jI} \end{bmatrix}$$

or

$$v_j = (S_j^T \Psi^{-1} S_j)^{-1} S_j^T \Psi^{-1} a_j, \qquad [2.6]$$

where S_j is of dimension $2N_C \times 2A$, Ψ is of dimension $2N_C \times 2N_C$, and the vector of voxel measurements, a_j, is of dimension $2N_C \times 1$. The isomorphism in Eq. [2.6] yields an image space vector, v_j, of dimension $2A \times 1$ that is comprised of the A real voxel values stacked upon the A imaginary voxel values. These A un-aliased voxel values correspond to the A folds that are formed via sub-sampling the data in k-space by a factor of A. It can be shown that the real and imaginary parts of the estimated complex-valued un-aliased voxel values in Eq. [2.4] are mathematically equivalent to the estimated real and imaginary isomorphism vector of un-aliased voxel values in Eq. [2.6].

2.2.2 A Linear Framework for Parallel Imaging

For the aliased images acquired from the N_C receiver coils to be combined and un-aliased with the SENSE unfolding matrix, the aliased images first need to be appropriately formatted. The formalism in Eqs. [1.3] and [1.4] is expressed to reconstruct data from a single receiver coil that acquires a full FOV array of k-space measurements, but can be generalized to reconstruct sub-sampled data from multiple receiver coils in an

array at once. With each of $\xi = [1,\ldots, N_C]$ receiver coils acquiring a $(p_y/A)\times p_x$ array of complex-valued sub-sampled spatial frequencies, $F_{\xi,C}$, a real-valued vector can be formed for each coil by stacking the rows of the real component of $F_{\xi,C}$ into a vector, $f_{\xi,R}$, stacking the rows of the imaginary component of $F_{\xi,C}$ into a vector, $f_{\xi,I}$, and then concatenating the vectors with the real and imaginary components for each coil into a single vector, $f_\xi = [f_{\xi,R}{}^T, f_{\xi,I}{}^T]^T$. Each coil vector, f_ξ, is now of the same form as f in Eq. [1.3], and when inverse Fourier reconstructed with the Ω operator, (that has been adjusted for the sub-sampled dimensions) results in a vector of aliased voxel values,

$a_\xi = \Omega f_\xi$.

Being of a single coil, the vector a_ξ is ordered in the same fashion as y in Eq. [1.3].

As illustrated in Fig.2.3, when the spatial frequency vectors from each of the N_C coils are concatenated into a single vector, f_{coil}, with alternating sub-vectors of the real and imaginary spatial frequency measurements from each coil, the inverse Fourier reconstruction of all N_C aliased coil images can be conducted at once using a Kronecker product of the inverse Fourier transform operator,

$$a_{coil} = (I_{N_C} \otimes \Omega) f_{coil}. \qquad [2.7]$$

The resulting vector, a_{coil}, in Eq. [2.7] is thus comprised of N_C sub-vectors, each with a vector of the real reconstructed aliased voxel values from coil ξ stacked upon a vector of imaginary reconstructed voxel values from coil ξ. As illustrated in Fig. 2.3, the N_C sub-vectors in a_{coil} can be reshaped into N_C aliased coil images by reversing the process used to generate the vector f_{coil}.

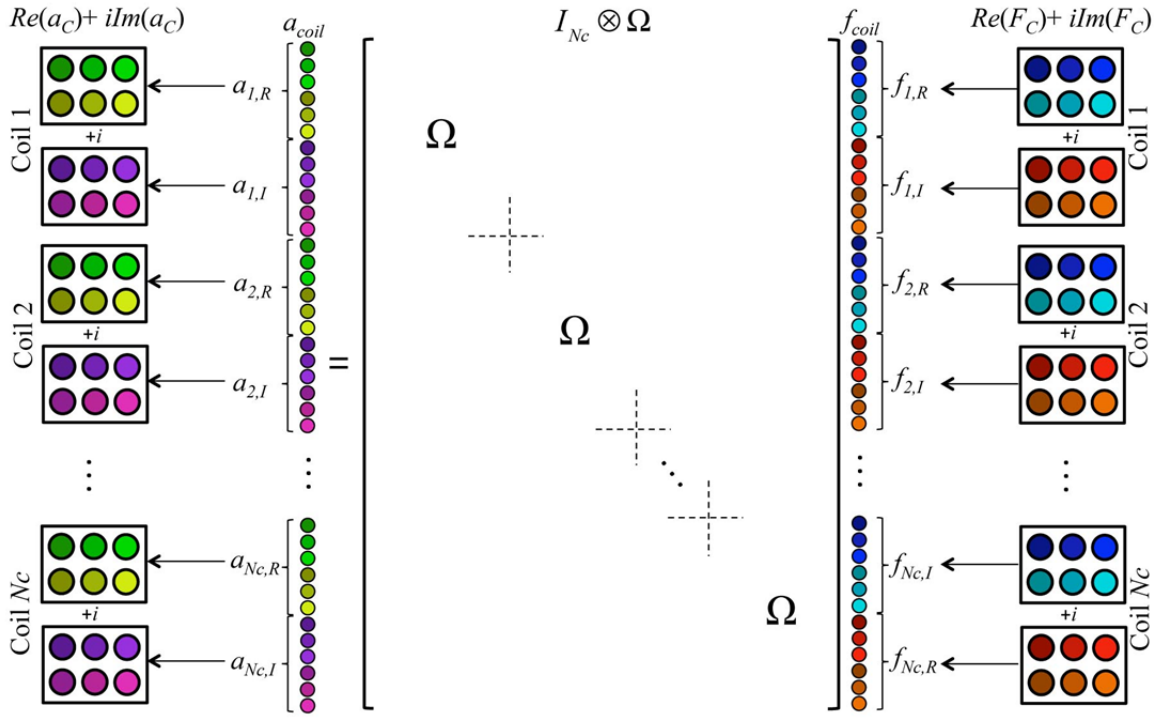

Figure 2.3: Vectorizing the sub-sampled spatial frequencies from each of N_C coils into a single real-valued vector, f_{coil}, such that all aliased coil images can be inverse Fourier reconstructed at once into another vector, a_{coil}, with N_C sub-vectors of alternating real and imaginary components.

2.2.3 SENSE Operator and Permutations

To apply the SENSE unfolding operation in Eq. [2.6] to all aliased voxels at once, the vector a_{coil} in Eq. [2.7] first needs to be permuted from being ordered by aliased coil image, to being ordered by aliased voxel. This reordering operation, illustrated in Fig. 2.4, can be undertaken by pre-multiplying the vector a_{coil} in Eq. [2.7] with a "complex" permutation matrix, P_C, by

$$a = P_C\,(I_{N_C} \otimes \Omega)\, f_{coil} = P_C\, a_{coil}. \qquad [2.8]$$

The result of such a permutation is another vector, a, containing the same elements as a_{coil}, but the elements are rearranged with the N_C real voxel values stacked upon the N_C imaginary voxel values for each of the rp aliased voxels in the N_C coil images.

In addition to the complex permutation applied in Eq. [2.8], it may be necessary to apply a second permutation that performs a Fourier transform shift when even acceleration factors are used. The underlying assumption for a continuous Fourier transform is that the limits of the domain being transformed are infinite. When an inverse Fourier transform is performed on a discrete array of *k*-space, with a finite domain, the continuity condition is accounted for by assuming a wraparound of spatial frequencies. This effectively places "copies" of the 2-dimensional *k*-space array at all four edges of the domain. When sub-sampling is performed in the PE dimension, the failure to meet the Shannon-Nyquist sampling criteria causes these "copies" of the inverse Fourier

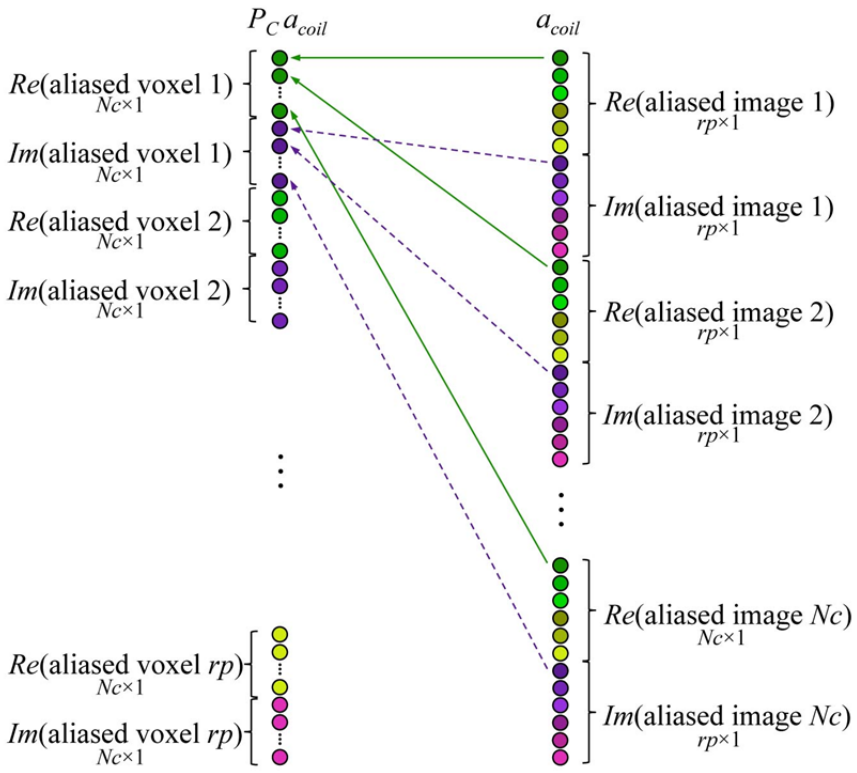

Figure 2.4: Complex permutation, P_C, used in the SENSE isomorphism to permute vector a_{coil} from being ordered by aliased coil image to being ordered by aliased voxel with the respective vector of the real components stacked on top of the vector of the imaginary components.

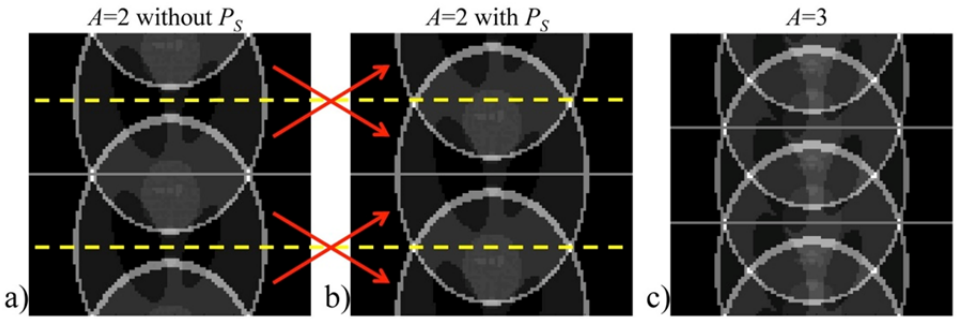

Figure 2.5: The unfolding of aliased images with a reduction factor of A=2 a) without a Fourier transform shift results in an off center image, and b) with a Fourier transform shift results in a centered image. c) No Fourier transform shift is needed for odd reduction factors such as A=3, as the image is centered after unfolding.

reconstructed image to overlap, placing the center of the image domain in the center of the aliased image. For an acceleration factor of A=2, the center of the image domain will therefore be in the center of the aliased image, and thus an unfolding of the aliased image will lead to an image that is shifted in the PE direction by $p_y/(2A)$, as illustrated in Fig. 2.5a, where the image appears to be off center. However, if a Fourier transform shift is applied to the aliased images after inverse Fourier reconstruction, then the top and bottom halves of the aliased images are effectively reversed, as illustrated in Fig. 2.5b, shifting the center of the un-aliased image back to the center of the image domain. As shown for an acceleration factor of A=3 in Fig. 2.5c, this is not an issue for odd acceleration factors because the center of the aliased image will always be aligned with the center of the image domain. As such, a Fourier transform shift permutation, P_S, pre-multiplies the complex permutation in Eq. [2.8] whenever an even acceleration factor, A, is selected,

$$a = P_S P_C (I_{N_C} \otimes \Omega) f_{coil}. \qquad [2.9]$$

In order to apply the SENSE isomorphism in Eq. [2.6] to un-alias all voxels in the aliased coil images at once using the linear framework in Eqs. [2.8] and [2.9], Eq. [2.6] is rewritten as

$v = Ua$,

where the SENSE unfolding matrix, U, is a block diagonal matrix, with the j^{th} block for un-aliasing voxel j defined by

$U_j = (S_j^T \Psi^{-1} S_j)^{-1} S_j^T \Psi^{-1}$.

Provided with the fully sampled coil sensitivities, a coil sensitivity matrix, S, can be constructed by placing the $2N_C \times 2A$ coil sensitivities in Eq. [2.4] corresponding to each aliased voxel $j = [1,\ldots, rp]$, S_j, along the diagonal of a block diagonal matrix, where rp denotes the total number of aliased voxels. Assuming a true covariance structure between spatial frequencies of Λ, and a covariance between receiver coils of Ψ, the covariance structure of the acquired k-space data in f, ordered by coil, is defined to be

$\Gamma = \Psi \otimes \Lambda$. [2.10]

When the acquired k-space data in all coils is inverse Fourier reconstructed into coil images through Eq. [2.7], the covariance structure between spatial frequencies that are ordered by coil in Eq. [2.10] is converted to a covariance between voxel values, also ordered by coil, through

$$\begin{aligned}\Sigma &= (I_{N_C} \otimes \Omega)\Gamma(I_{N_C} \otimes \Omega)^T \\ &= \Psi \otimes (\Omega \Lambda \Omega^T),\end{aligned}$$

where the covariance between voxels is

$\Upsilon = \Omega \Lambda \Omega^T$.

In order to reconstruct all voxels at once with a known covariance between voxels, Υ, the SENSE unfolding operator is expressed as

$$U = \left(S^T \left(\Upsilon \otimes \Psi \right)^{-1} S \right) S^T \left(\Upsilon \otimes \Psi \right)^{-1}, \quad [2.11]$$

where the order of Ψ and Υ are reversed in the Kronecker product in Eq. [2.11] because the data un-aliased by U has been permuted by P_C to being ordered by voxel rather than by coil. Although it can be shown when estimated from experimental data that Υ is not an identity matrix (Bruce et al., 2012), the general practice in almost all applications of the SENSE model is to use an identity covariance between voxels. If Υ is assumed to be an identity matrix of size rp, the SENSE unfolding operator assumes that all voxels in the aliased coil images exhibit the same covariance between coils, Ψ, and thus Eq. [2.11] becomes a block diagonal matrix of the form

$$U = \left(S^T \left(I_{rp} \otimes \Psi \right)^{-1} S \right) S^T \left(I_{rp} \otimes \Psi \right)^{-1}.$$

A discussion on the choice between $\Upsilon \neq I_{rp}$ and $\Upsilon = I_{rp}$ in Eq. [2.11] is carried out in Appendix A. It has been shown in Bruce et al. (2012) that while the assumption of $\Upsilon \neq I_{rp}$ may be more mathematically appropriate, the incorporation of Υ into the SENSE model through Eq. [2.11] does not offer a sufficient improvement over the common assumption that $\Upsilon = I_{rp}$ to justify the significantly increased computational load. As such, $\Upsilon = I_{rp}$ will be assumed for the remainder of this dissertation unless stated otherwise. When U is applied as an operator, it will perform the real-valued un-aliasing of the N_C real and N_C imaginary aliased voxel values in Eq. [2.6] into A real and A imaginary voxel values for all rp aliased voxels at once,

$$v = U P_S P_C (I_{N_C} \otimes \Omega) f_{coil}.$$

After an application of the SENSE operator, U, it is then necessary to apply a third permutation, P_U, illustrated in Fig. 2.6, that reorders the real and imaginary un-aliased

voxel values in v from being ordered by voxel to being ordered by fold. Applying a permutation of this kind results in a vector of all real image values stacked upon all imaginary image values,

$$y = P_U\, U\, P_S\, P_C\, (I_{N_C} \otimes \Omega)\, f_{coil}, \qquad [2.12]$$

that is of the same order as the vector y in Eq. [1.3].

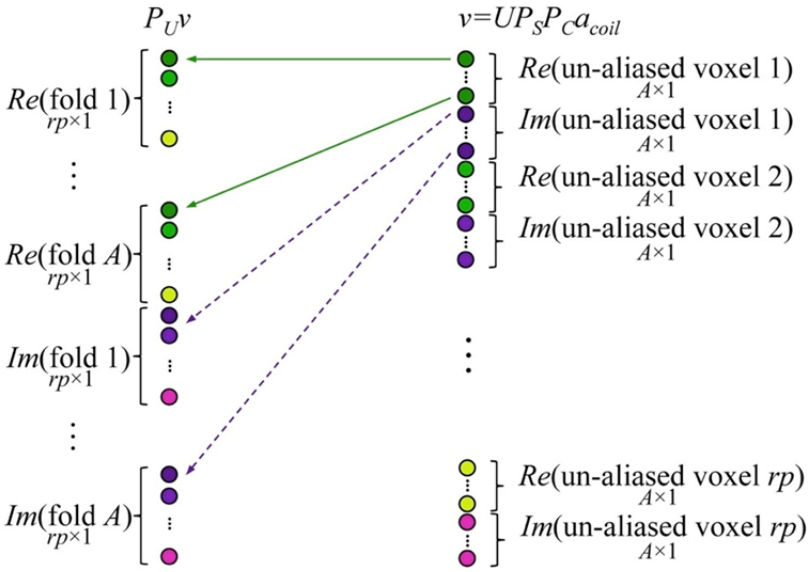

Figure 2.6: Unfolding permutation, P_U, used in the SENSE isomorphism to permute vector v from being ordered by un-aliased voxel to being ordered by fold.

The framework in Eq. [2.12] enables additional operators for pre-processing in k-space, O_K, and image space processing, O_I, to be incorporated into the reconstruction by

$$y = O_I\, P_U\, U\, P_S\, P_C\, (I_{N_C} \otimes \Omega O_k)\, f_{coil}. \qquad [2.13]$$

The operators used to reconstruct the acquired k-space data in Eq. [2.12] can finally be combined into a single operator that performs the entire SENSE reconstruction by

$$O_{SE} = O_I\, P_U\, U\, P_S\, P_C\, (I_{N_C} \otimes \Omega O_k). \qquad [2.14]$$

2.3 SENSE Operator Induced Correlations

Assuming a true covariance between coils, Ψ, and a true covariance between spatial frequencies, Λ, the data vector, f_{coil}, in Eq. [2.12] is described by the sum of a vector of mean spatial frequency measurements, $E[f_{coil}]=f_0$, with added measurement error that has the covariance structure, $\text{cov}(f_{coil})=\Gamma$, in Eq. [2.10]. When the operators in Eq. [2.14] are applied to f_{coil} in Eq. [2.12], the resulting image vector will have a mean of $E[y]=O_{SE} f_0$ and a modified covariance structure of

$$\text{cov}(y) = O_{SE}\, \Gamma O_{SE}^{T}. \qquad [2.15]$$

In order to determine the covariance structure induced solely by the reconstruction operators in Eq. [2.14], Γ is assumed to be an identity matrix, simplifying Eq. [2.15] to

$$\begin{aligned}\Sigma_{SE} &= O_{SE}\, O_{SE}^{T} \\ &= O_I\, P_U\, U\, P_S\, P_C\, (I_{N_C}\otimes\Omega O_K)\, (I_{N_C}\otimes\Omega O_K)^{T}\, P_C^{T}\, P_S^{T}\, U^{T}\, P_U^{T}\, O_I^{T}.\end{aligned}$$

Under the assumption that $\Gamma=I$, any non-zero terms in the off diagonal elements of Σ_{SE} denote an artificially induced covariance (and in turn correlation) between voxels in the reconstructed image vector, y. It is important to note that such an induced covariance is purely a result of the reconstruction process, and is of no biological origin whatsoever.

Assuming there are no pre-processing operations performed in k-space, $O_K=I$, the covariance induced by each operation in Eq. [2.14] can be investigated by simply multiplying each individual operator by its transpose. To quantify the covariance induced by each operator, operators were constructed to simulate the reconstruction of a 6×6 array of spatial frequencies acquired by N_C=4 receiver coils, sub-sampled by a factor of A=2. Starting with the first operator applied to the frequency vector, f_{coil}, the inverse Fourier transform operator, $(I_{N_C}\otimes \Omega)$, illustrated in Fig. 2.7a is shown to be orthogonal, resulting

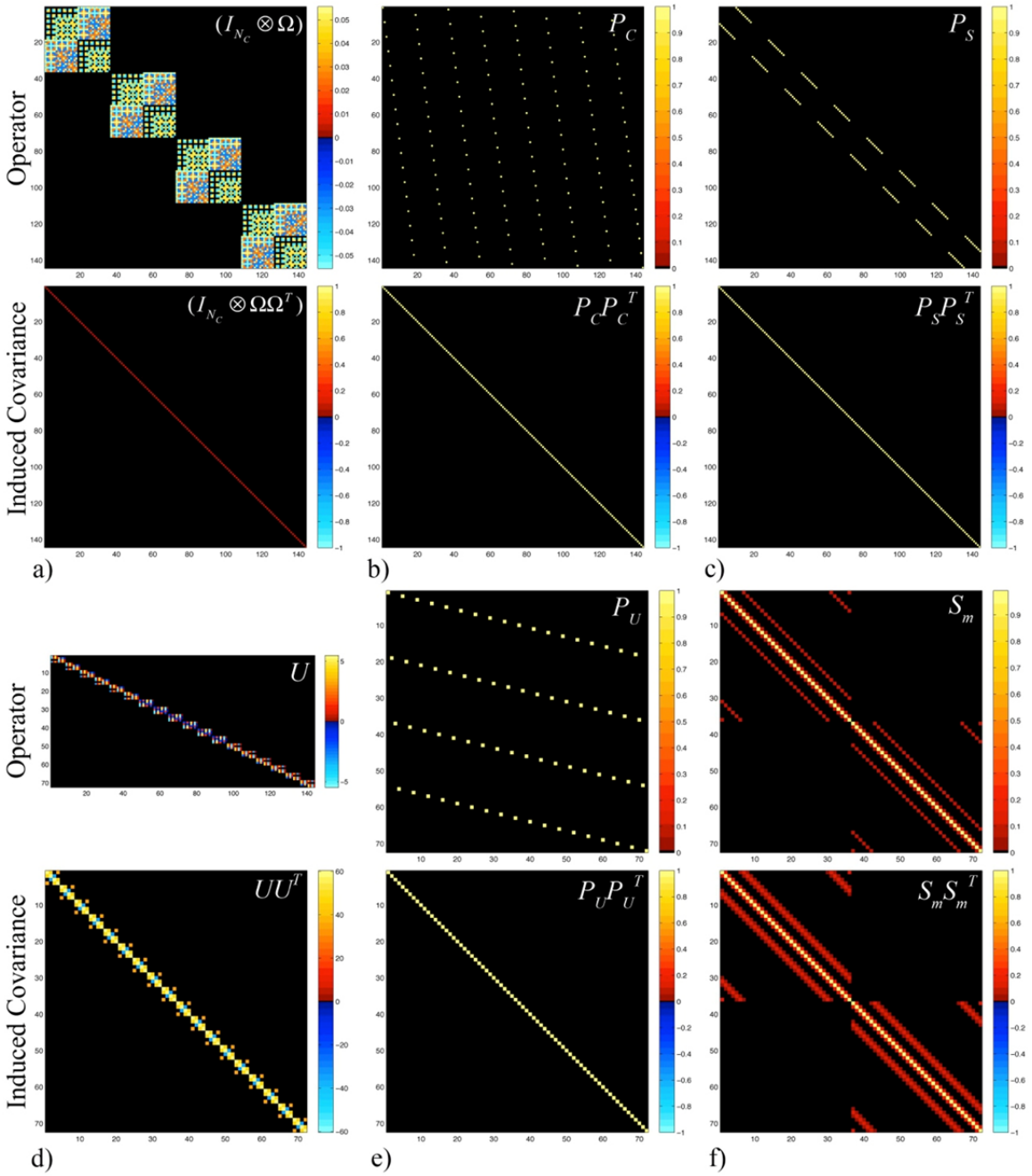

Figure 2.7: Illustrated for a toy example unfolding 6×6 images acquired with A=2 from N_C =4 coils, operators and covariance induced by a) inverse Fourier transform applied to N_C=4 coils, b) complex permutation, c) shift permutation, d) SENSE un-aliasing operator, e) unfolding permutation, and f) a Gaussian smoothing operator, S_m, with fwhm of one voxel.

in an identity covariance matrix scaled by $A/p_x p_y$ when multiplied by its transpose. As such, there is no covariance induced between voxels by the ($I_{N_C}\otimes \Omega$) operator. Similarly, the permutations P_C and P_S in Figs. 2.7b and 2.7c merely rearrange the data vector that they pre-multiply, and are therefore orthonormal, resulting in identity matrices when multiplied by their respective transposes. As predicted in Fig. 2.2, the SENSE un-aliasing matrix, U, is not an orthogonal operation, and thus the block diagonal operator in Fig. 2.7d is shown to result in a block diagonal induced covariance matrix when multiplied by its transpose. Since the data vector, $P_S P_C (I_{N_C}\otimes\Omega) f_{coil}$, that the SENSE un-aliasing operator pre-multiplies is permuted to being ordered from by coil to by aliased voxel, the blocks along the diagonal of the covariance matrix in Fig. 2.7d denote the covariance structure induced between the previously aliased voxels. Although the unfolding permutation, P_U, is orthonormal by itself, as shown in Fig. 2.7e, the fact that it pre-multiplies the SENSE un-aliasing matrix, which is not orthogonal, means that any covariance induced by the SENSE operator will be rearranged by the permutation. This is true even if the original data was assumed to have an identity covariance, $\Gamma=I$, and thus the resulting covariance induced by the SENSE model simplifies to

$$\Sigma_{SE} = \frac{A}{p_x p_y}\left(O_I P_U U U^T P_U{}^T O_I{}^T\right).$$

In almost all fMRI and fcMRI studies, it is common practice to perform spatial filtering (smoothing) after image reconstruction in an effort to increase the contrast to noise ratio (CNR) (Lowe & Sorenson, 1997). As such, a Gaussian smoothing kernel, $O_I=S_m$, with a full-width-at-half-maximum (fwhm) of one voxel was applied in image space after the unfolding permutation,

$$y = S_m P_U U P_S P_C (I_{N_C} \otimes \Omega) f_{coil},$$

and thus the SENSE operators for smoothing and reconstructing *k*-space data becomes

$$O_{SEsm} = S_m P_U U P_S P_C (I_{N_C} \otimes \Omega). \quad [2.16]$$

By definition, the operation of spatial smoothing induces a covariance between a voxel and its neighbors, and thus the covariance induced solely by the smoothing operator in Fig. 2.7f is not orthogonal. Furthermore, the fact that the operator *Sm* post-multiplies the unfolding permutation and SENSE unfolding operation, $P_U U$, means that any covariance induced by the SENSE operator will be further modified by the smoothing operation. The resulting covariance induced by the SENSE model together with smoothing thus becomes

$$\Sigma_{SEsm} = \frac{A}{p_x p_y}\left(S_m P_U U U^T P_U{}^T S_m{}^T\right).$$

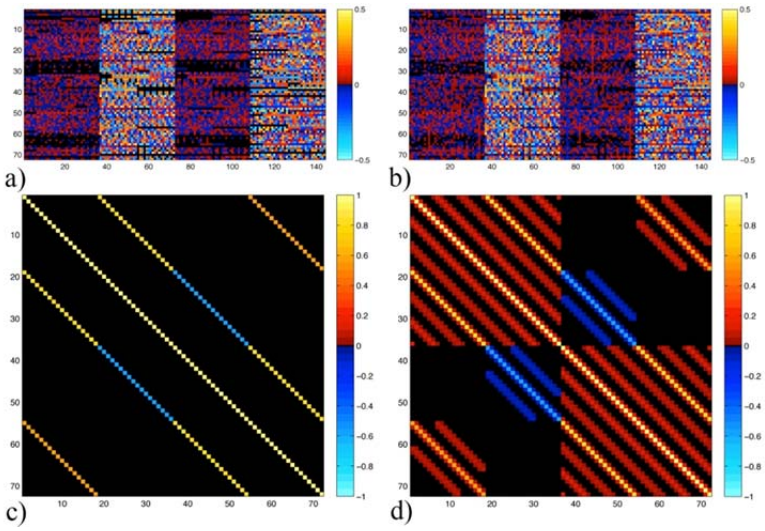

Figure 2.8: a) The complete SENSE reconstruction matrix, b) the SENSE reconstruction matrix with Gaussian smoothing, c) the correlation induced by the complete SENSE process and d) the correlation induced by the SENSE process with Gaussian smoothing.

The overall SENSE reconstruction operators without smoothing in Eq. [2.14] are presented in Fig. 2.8a, and together with smoothing in Eq. [2.16] are presented in Fig. 2.8b. Inserting the SENSE operations in both Eq. [2.14] and Eq. [2.16] into Eq. [1.9], the correlations induced by the entire SENSE model are precisely quantified and presented without smoothing in Fig. 2.5c and with smoothing in Fig. 2.8d. It is apparent that the SENSE operators together with Gaussian smoothing in Fig. 2.8d spread the structure of the correlation induced by the SENSE model in Fig. 2.8c to additional neighboring voxels. This indicates that while spatial filtering is commonly thought to improve the CNR of an image, it can have adverse effects on the covariance of the reconstructed image as well. If the correlation matrices in Figs. 2.8c and 2.8d are partitioned into quadrants, such as those in Eq. [1.10], there are apparent non-zero elements in the upper right and lower left quadrants that indicate correlations are induced between the real and imaginary components of the reconstructed data.

2.4 Theoretical Illustration of SENSE Induced Correlations

2.4.1 Data Generation

To replicate the process of acquiring data from an MRI scanner with a standard EPI pulse sequence, a time series of complex valued spatial frequencies was generated using the MR signal equation,

$$f(k_x,k_y)=\int_{-\infty}^{\infty}\int_{-\infty}^{\infty}\rho(x,y)e^{-t/T_2^*(x,y)}e^{-i\gamma B(x,y)t}e^{-i2\pi(k_x x+k_y y)}\,dx\,dy. \qquad [2.17]$$

In Eq. [2.17], every spatial frequency value, $f(k_x,k_y)$, is derived from a linear combination of the proton spin density, ρ, the intra-acquisition decay, T_2^*, and the magnetic field, B, in

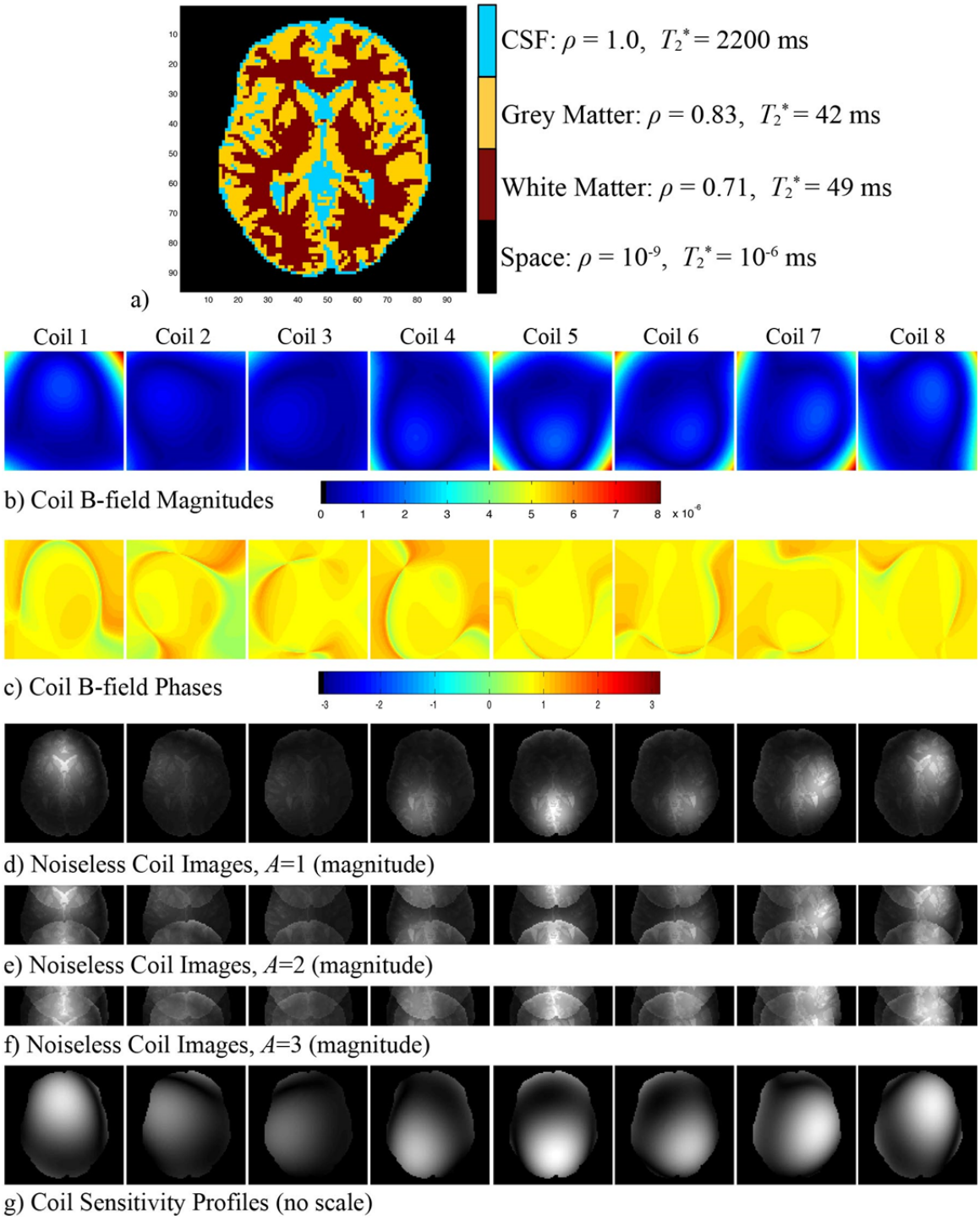

Figure 2.9: Data generated through Eq. [2.17] using a) a 96×96 Brain phantom with proton spin density, ρ, and transverse relaxation, T_2^*, parameters defined for CSF, grey matter, white matter and space. Data was generated for each of N_C=8 coils using B-field b) magnitudes and c) phases estimated from experimentally acquired data, resulting in noiseless coil images (magnitude shown) for acceleration factors of d) A=1, e) A=2, f) A=3. As used in the SENSE reconstruction g) full FOV B-field sensitivity profiles (magnitude shown) were estimated for each of the N_C=8 receiver coils.

every voxel location, (x,y), within the slice of the object being scanned. As the magnetic field gradients in an MRI scanner Fourier encode the spatial frequency spectrum of the object being scanned, the term $e^{-i2\pi(k_x x+k_y y)}$ in Eq. [2.17] corresponds to the forward Fourier transform. In this simulation, the 96×96 brain phantom in Fig. 2.9a was used to simulate an axial slice of a human subject's brain. Voxels that correspond to white matter, grey mater, cerebral spinal fluid (CSF) and points in space were given tissue specific values of both ρ and T_2^*, as listed in Fig. 2.9a. To simulate the acquisition of k-space using a phased array, a collection of N_C=8 B-fields, B, were estimated from an experimentally acquired human subject resting-state data set (that will be presented in the Experimental Illustration to follow) by fitting a third order polynomial to estimated sensitivity profiles. The magnitude and phase of the B-field for each of the N_C=8 receiver coils are presented in Fig. 2.9b and Fig. 2.9c respectively. The B-fields in Fig. 2.9b and Fig. 2.9c were estimated from data acquired in a 3.0 T MRI scanner, and the gyromagnetic ratio, γ, in Eq. [2.17] is γ=42.58 MHz/T.

To simulate the acquisition of spatial frequencies, the generation of each spatial frequency value, $f(k_x,k_y)$, in Eq. [2.17] is performed by shifting through k-space in increments of Δt=0.004 ms, thereby defining a time, t, at which each location in k-space is acquired. As with a standard EPI pulse sequence in Fig. 1a, k-space is sampled on a frequency-by-frequency and row-by-row basis, starting in the lower left corner. The magnetic field gradients shift through k-space in the frequency encoding direction from the lower left corner to the lower right corner, measuring spatial frequencies spaced Δk_x apart. Once an entire row of frequencies has been acquired, the gradient in the frequency encoding direction is reversed while the gradient in the phase encoding direction is

applied simultaneously to shift vertically by an increment of Δk_y. This turn around process occurs over a series of "turn around" points, during which the time, t, is incremented by Δt=0.004 ms at each point. For this simulation, a total of 80 turn around points were simulated for each turn. When shifting in the PE dimension by an increment of Δky, a fully sampled array of spatial frequencies is acquired, resulting in the noiseless coil images in Fig. 2.9d after applying an inverse Fourier transform. To simulate sub-sampling by an acceleration factor of A, the increment in the PE dimension was increased to $A\Delta ky$. The resulting noiseless inverse Fourier reconstructed sub-sampled coil images for accelerations of A=2 and A=3 are illustrated in Fig. 2.9e and Fig. 2.9f respectively.

To generate the time series of images, the noiseless spatial frequency arrays generated by Eq. [2.17] for each coil with acceleration factors A=1 (fully sampled), A=2 and A=3 were first inverse Fourier reconstructed into the image domain to generate noiseless coil images for each acceleration factor. These noiseless coil images were then scaled to have a maximum magnitude of 50 in the coil image with the greatest magnitude, and subsequently Fourier transformed back into spatial frequency arrays for each coil. A time series of 500 time repetitions (TRs) was generated for all N_C=8 coils by adding Gaussian noise with a mean of zero and a standard deviation of $\sqrt{p_x p_y} = \sqrt{96 \cdot 96}$ to both the real and imaginary components of the 500 k-space arrays for each coil and for each of the three different acceleration factors. If a $p_y \times p_x$ array of k-space, with a standard deviation of $\sqrt{p_x p_y}$, is sub-sampled by a factor of A, the standard deviation of the corresponding $(p_y/A) \times p_x$ inverse Fourier reconstructed image will be increased by $\sqrt{A}$. When A=1 in the fully sampled data set, this results in images with a standard deviation of 1, and thus a maximum SNR (magnitude/standard deviation) of 50 in the coil images.

When A>1, the standard deviation is therefore expected to increase, and thus the SNR of the reconstructed images is expected to decrease in turn.

When the complex-valued Gaussian noise was added to each TR of the time series, a complex-valued coil covariance structure, Ψ, was also induced between the coil arrays. The covariance matrix, Ψ, used in this illustration was derived from the same

Table 2.1: Coil correlation structure estimated from a human subject data set.

a) Correlation between real components of each coil (Ψ_{RR})

1	0.6496	0.1819	-0.3027	0.4453	0.4415	-0.2778	-0.5478
0.6496	1	0.6483	-0.1925	0.5118	0.4825	-0.0915	-0.1967
0.1819	0.6483	1	0.2368	0.5997	0.5342	0.0868	0.0375
-0.3027	-0.1925	0.2368	1	0.2471	0.3889	0.4605	0.3363
0.4453	0.5118	0.5997	0.2471	1	0.7886	-0.4482	-0.4809
0.4415	0.4825	0.5342	0.3889	0.7886	1	-0.2639	-0.4627
-0.2778	-0.0915	0.0868	0.4605	-0.4482	-0.2639	1	0.7266
-0.5478	-0.1967	0.0375	0.3363	-0.4809	-0.4627	0.7266	1

b) Correlation between imaginary components of each coil (Ψ_{II})

1	0.6448	0.0705	-0.4013	0.4243	0.4314	-0.4087	-0.6343
0.6448	1	0.5261	-0.3035	0.4472	0.4278	-0.2055	-0.2564
0.0705	0.5261	1	0.2677	0.5352	0.4847	0.1056	0.0966
-0.4013	-0.3035	0.2677	1	0.224	0.3418	0.502	0.3966
0.4243	0.4472	0.5352	0.224	1	0.7672	-0.4848	-0.479
0.4314	0.4278	0.4847	0.3418	0.7672	1	-0.299	-0.4764
-0.4087	-0.2055	0.1056	0.502	-0.4848	-0.299	1	0.7586
-0.6343	-0.2564	0.0966	0.3966	-0.479	-0.4764	0.7586	1

c) Correlation between real and imaginary components of each coil (Ψ_{RI})

-0.078	0.4349	0.6323	0.4003	0.148	0.1643	0.514	0.5416
-0.56	-0.0859	0.5932	0.6195	0.0736	0.0809	0.5715	0.5988
-0.6769	-0.625	0.0573	0.8011	-0.1161	-0.0461	0.584	0.5626
-0.3838	-0.558	-0.7516	0.0023	-0.7741	-0.5255	0.3833	0.3465
-0.2494	-0.1737	0.1329	0.7752	-0.0281	0.3376	0.5983	0.3519
-0.2629	-0.1743	0.0524	0.5261	-0.3949	-0.0192	0.8141	0.4769
-0.4865	-0.484	-0.4965	-0.3295	-0.5473	-0.8054	0.0304	0.4048
-0.473	-0.4974	-0.4931	-0.3255	-0.2916	-0.4477	-0.3657	0.0095

experimentally acquired human subject resting-state data set that was used for estimating the coil B-field profiles. To observe the structure of the coil covariance, the matrix Ψ was converted to a correlation structure and presented in Table. 2.1. Upon observation, the structure in Table 2.1 is not an identity matrix, as assumed in most applications of the SENSE model. Based on the skew symmetric structure assumed by the SENSE model in Eq. [2.5], the imaginary covariance between coils is changed from the structure in Table 2.1b to $\Psi_I = \Psi_R$ in Table 2.1a, and the covariance between the real and imaginary components of the coil images is converted from the structure in Table 2.1c to the negative of the estimated imaginary structure in Table. 2.1b.

2.4.2 Data Reconstruction and Processing

As performed when reconstructing experimentally acquired data with the SENSE model, the coil B-field sensitivity profiles, S_C, and the estimated covariance between coils, $\hat{\Psi}$, used in Eq. [2.2] are estimated from the fully sampled calibration data. The fully sampled data set generated with A=1 was therefore used for calibration in this study. To estimate the coil B-field sensitivity profiles, a mean image for each of the N_C=8 coils was derived by taken the mean over the individual coil time series. To normalize these mean coil images and remove any anatomical structure, a single "body coil" image was derived by averaging the mean coil images into a single image. Each of the N_C=8 mean coil images was then divided by the simulated body coil image. The result of this process is the estimated coil B-field sensitivity profiles illustrated in Fig. 2.9g that have no anatomical structure and describe the decrease in B-field strength with distance from each coil. The procedure used for estimating the covariance between coils, $\hat{\Psi}$, is outlined in

Appendix A. With estimates of both S_C and $\hat{\Psi}$, the aliased coil images in each TR of the time series with A=1, A=2, and A=3 were reconstructed into full FOV combined images with the SENSE model in Eq. [2.2]. As most fcMRI studies use spatial filtering to increase CNR (Lowe & Sorenson, 1997), smoothing was performed by convolving each of the reconstructed image with a Gaussian smoothing kernel that had a fwhm of 3 voxels. The weights of the smoothing kernel were normalized such that the smoothed images would be of the same signal strength as the unsmoothed images.

2.4.3 Results

The mean magnitude and phase images from the reconstructed time series with A=1, A=2, and A=3 are presented in Fig. 2.10a, Fig. 2.10b, and Fig. 2.10c respectively. Due to the fact that the number of coils is more than double that of the highest acceleration factor, the system of equations in Eq. [2.1] is very over-determined. As such, there is no apparent difference in either the mean magnitude or mean phase images of the three different data sets. When the N_C=8 aliased coil images are combined into a single un-aliased image with SENSE, the standard deviation of the combined image will be lower than that of the individual coil images. This is apparent in Fig. 2.10a for A=1, where each reconstructed coil image had a standard deviation of 1, while the SENSE reconstructed image has a standard deviation (on average) that is close to 0.2. Consequently, the SNR of the combined fully sampled data set in Fig. 2.10a is increased from 50 in the uncombined coil images to 200 in the SENSE combined image. Upon observation of the standard deviation and SNR for the SENSE reconstructed time series with A=1, A=2, and A=3, presented in Fig. 2.10a, Fig. 2.10b, and Fig. 2.10c respectively, there is an apparent increase in the standard deviation with an increase in the acceleration

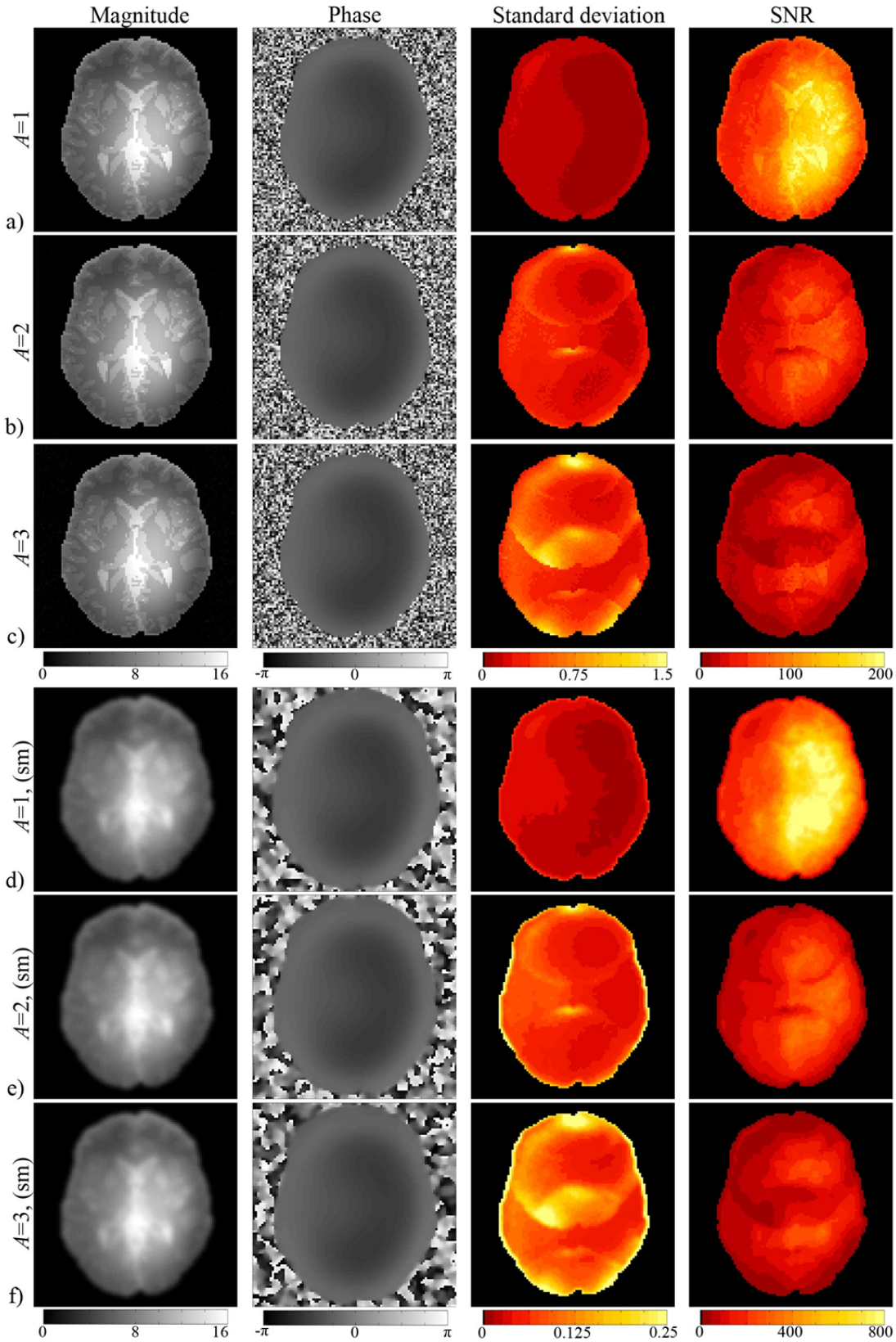

Figure 2.10: Mean magnitude and phase, standard deviation and SNR for SENSE reconstructed images with a) A=1, b) A=2, c) A=3, as well as d) A=1, e) A=2, and f) A=3 with smoothing.

factor. This is due to the fact that the noise added to the *k*-space array for each coil image in the time series had a standard deviation of $\sqrt{p_x p_y} = \sqrt{96 \cdot 96}$, and thus when *k*-space was sub-sampled by *A*=2 and *A*=3, the standard deviation of the inverse Fourier reconstructed coil images was increased within the regions of aliasing by a factor of $\sqrt{2}$ and $\sqrt{3}$ respectively. In areas of the reconstructed images with *A*=2 and *A*=3 in which there was no aliasing (such as the sides of the phantom), the standard deviation is more on the order of that in Fig. 2.10a where *A*=1. A consequence of this increase in the standard deviation in the previously aliased regions of the phantom is the notable decrease in the SNR of SENSE reconstructed images in Fig. 2.10b and 2.10c for *A*=2 and *A*=3, by comparison to that of a reconstruction with *A*=1 in Fig. 2.10a.

As almost all current fMRI and fcMRI studies use spatial filtering to increase CNR, each of the 500 images in the SENSE reconstructed time series with *A*=1, *A*=2 and *A*=3 were smoothed using a Gaussian smoothing kernel with a fwhm of 3 voxels. As with the unsmoothed images, the mean magnitude and phase images from the reconstructed time series with *A*=1, *A*=2, and *A*=3, presented in Fig. 2.10d, Fig. 2.10e, and Fig. 2.10f respectively, show no noticeable differences between them. As the desired effect of spatial smoothing is to reduce the standard deviation, and in turn the noise, the standard deviations for all acceleration factors are significantly reduced (note the scale difference between the standard deviations in Figs. 2.10a-2.10c and those in Figs. 2.10d-2.10f). All standard deviation and SNR images in Fig. 2.10 have been masked to focus on the behavior within the phantom. The “ring” of high standard deviation around the phantom in the reconstructed images with *A*=2 in Fig. 2.10e and *A*=3 in Fig. 2.10f results from a decreased standard deviation within the phantom by comparison to that in space. As with

the unsmoothed reconstructed images, the SNR of the smoothed SENSE reconstructed images decreases with an increase in the acceleration factor. As the standard deviation in all images in Fig. 2.10 increases in the regions of the phantom that were aliased for A=2 and A=3, the SNR is notably lower in these aliased regions in turn.

By constructing the SENSE unfolding operator, U, in Eq. [2.14] for acceleration factors of A=1, A=2 and A=3, the theoretical correlations induced by the entire SENSE reconstruction process were determined by inserting the operator O_{SE} for each acceleration factor into Eq. [1.9]. Through Eq. [1.9] the theoretical correlations induced between the real un-aliased voxel values, between the imaginary un-aliased voxel values, and between the real and imaginary un-aliased voxel values are determined. To observe these correlations about a single voxel of interest (VOI), j, one merely reshapes the j^{th} rows in the respective quadrants of the matrix generated in Eq. [1.9] into $p_y \times p_x$ matrices. As an identity covariance structure was assumed between spatial frequencies in generating the time series of images in each coil for each acceleration factor, there is no inherent structure in the original data. Any correlation structure noted in either the theoretical induced correlations determined by Eq. [1.9] or those estimated from the SENSE reconstructed Monte Carlo (MC) time series will therefore be a direct result of the SENSE reconstruction process.

The theoretical correlations induced about a VOI in the anterior of the brain phantom, highlighted by a pink circle, by the SENSE unfolding process for a data set with no sub-sampling (A=1) are presented on top of a magnitude reconstructed image underlay in Fig. 2.11a with a threshold of ±0.125. As this data set was generated with no sub-sampling, there was no un-aliasing performed in the reconstruction process. As such,

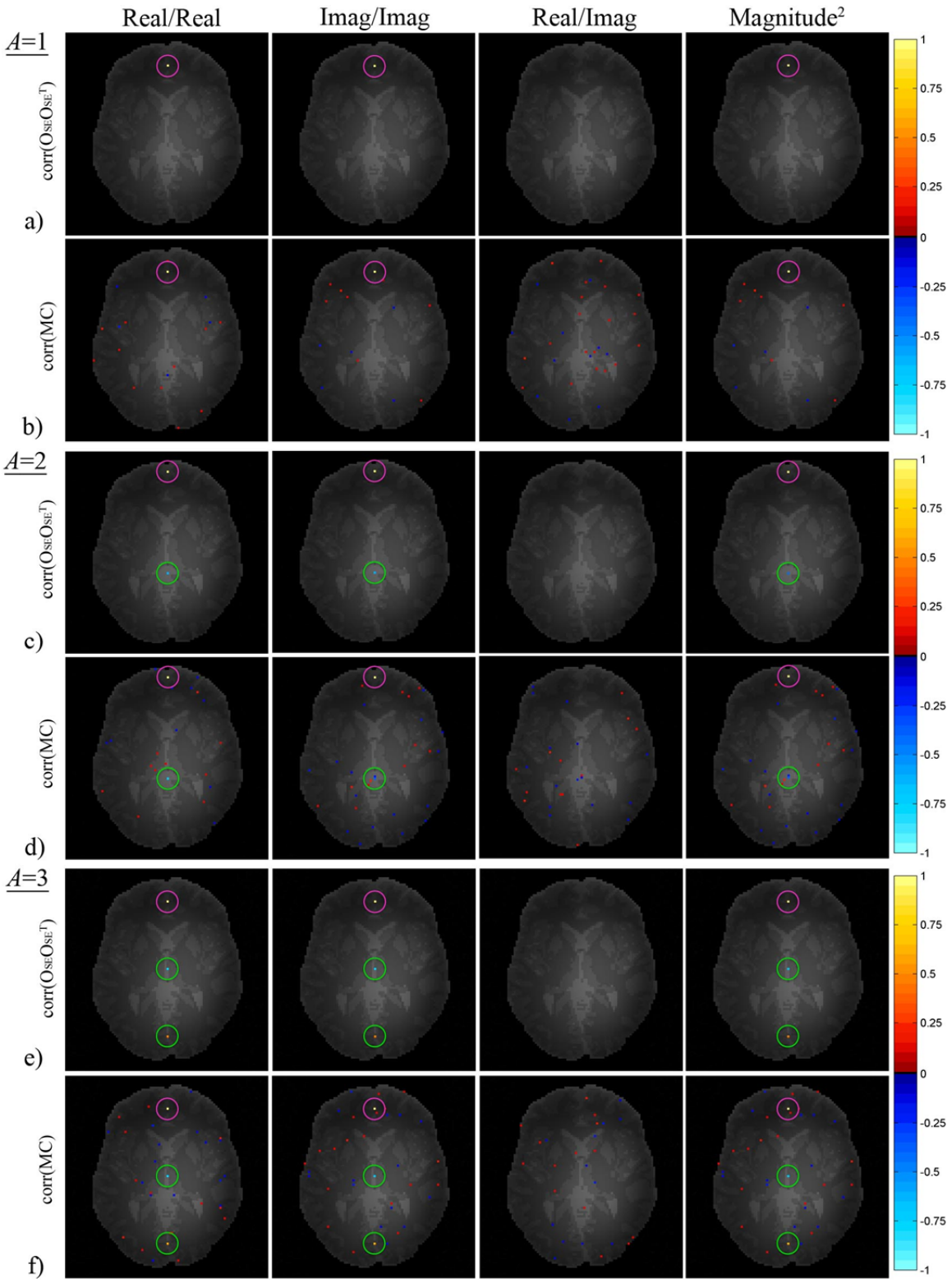

Figure 2.11: Presented on a magnitude brain phantom underlay and threshold to ±0.125 are real, imaginary, real/imaginary and magnitude-squared correlations a) theoretically induced by SENSE with A=1, b) estimated from MC data with A=1, c) theoretically induced by SENSE with A=2, d) estimated from MC data with A=2, e) theoretically induced by SENSE with A=3, and f) estimated from MC data with A=3.

there is no correlation induced by the SENSE model between the real component of the VOI and the real component of any other voxel, between the imaginary component of the VOI and the imaginary component of any other voxel, or between the real component of the VOI and the imaginary component of any other voxel. While magnitude-only data has become the gold standard in many fMRI and fcMRI studies, the reconstruction of magnitude data is not a linear operation, and thus the correlations induced by such a process are not presented here. However, the square of magnitude-only data is a linear process, and the correlation structures of magnitude-only and magnitude-squared data are asymptotically equivalent (and visually indistinguishable) (Nencka et al., 2009; Rowe and Nencka, 2009). As such, the correlations induced by the SENSE reconstruction with A=1 about the VOI in magnitude-squared data is presented in Fig. 2.11a. As with the real and imaginary induced correlation structures, there is no correlation induced between the VOI and any other voxel since no un-aliasing was performed. To validate the theoretical correlations induced by the SENSE model with A=1, the real, imaginary, real/imaginary and magnitude-squared correlations about the VOI were also estimated from the MC timeseries reconstructed with A=1, and are presented in Fig. 2.11b. As predicted by the theoretical correlations in Fig. 2.11a, there is no apparent correlation structure induced between the VOI and any other voxel that is more than a byproduct of the random noise added to the data set.

The theoretical correlations induced by the SENSE unfolding process with A=2 and A=3 are presented about a VOI in the center of the pink circles in Fig. 2.11c and Fig. 2.11e respectively. Prior to the SENSE reconstruction, the VOI selected in Fig. 2.11c was aliased with a single aliased VOI (aVOI) due to the two-fold aliasing with A=2, and the

VOI selected in Fig. 2.11e was previously aliased with two aVOIs due to the three-fold aliasing with A=3. The green circles in Fig. 2.11 highlight the locations of each aVOI. Upon observation, there are negative real, imaginary and magnitude squared correlations induced between the VOI and aVOI by a SENSE reconstruction with A=2 in Fig. 2.11c, while the SENSE reconstruction with A=3 induces a negative real, imaginary and magnitude squared correlations between the VOI and the aVOI in the center of the phantom and a positive correlation between the VOI and the aVOI in the anterior of the phantom. As with the fully sampled data set, there is no apparent correlation between the real component of the VOI and the imaginary component of any other voxel for SENSE reconstructions with A=2 or A=3. To validate the theoretical correlations induced by the SENSE model with A=2 and A=3, the real, imaginary, real/imaginary and magnitude squared correlations estimated from the MC reconstructed time series are presented in Fig. 2.11d for A=2, and in Fig. 2.11f for A=3. As predicted by the theoretical correlations induced by SENSE with A=2 and A=3 in Fig. 2.11c and Fig. 2.11e, there are correlations of the same sign noted between the VOI and aVOIs in Fig. 2.11d and Fig. 2.11f. As with the correlations estimated from the time series reconstructed with A=1, there are additional random low correlations between the VOI and other voxels spread throughout the phantom for reconstructions with both A=2 and A=3 that are merely a result of the noise added when generating the data.

When a Gaussian smoothing operator, Sm, with a fwhm of 3 voxels is applied after the SENSE unfolding process, as in Eq. [2.16], the correlations induced by SENSE for acceleration factors of A=1, A=2, and A=3 together with smoothing are determined by inserting the operator $S_m O_{SE}$ for each acceleration factor into Eq. [1.9]. The theoretical

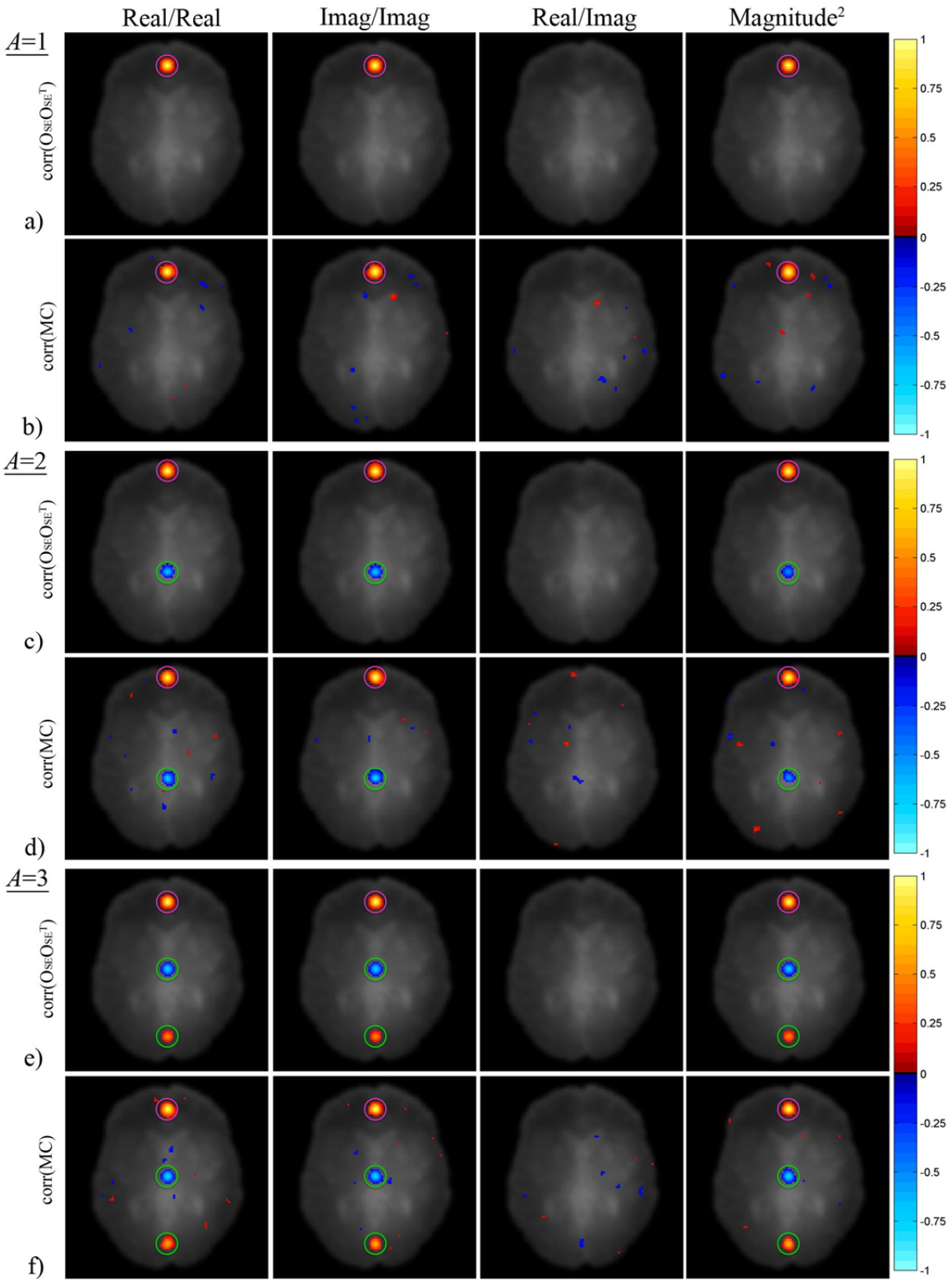

Figure 2.12: Presented on a magnitude underlay and threshold to ±0.125 are smoothed real, imaginary, real/imaginary and magnitude-squared correlations a) theoretically induced by SENSE with A=1, b) estimated from MC data with A=1, c) theoretically induced by SENSE with A=2, d) estimated from MC data with A=2, e) theoretically induced by SENSE with A=3, and f) estimated from MC data with A=3.

correlations induced by SENSE with A=1, A=2, and A=3 together with smoothing are presented in Fig. 2.12a, Fig. 2.12c, and Fig. 2.12e respectively. Upon comparison to the unsmoothed counterparts in Fig. 2.11, all SENSE induced correlations between the VOI and aVOIs are of the same sign and appear to be spread to the neighboring voxels of both the VOI and the neighboring voxels of the aVOIs. This implies that while the VOI may be artificially aliased with an aVOI by the SENSE model, the addition of smoothing induces a correlation between the VOI and neighboring voxels of the aVOIs. The theoretical correlations induced by SENSE reconstructions with A=1, A=2 and A=3 together with smoothing are validated by observing the MC correlations estimated from the smoothed reconstructed time series for A=1 in Fig. 2.12b, for A=2 in Fig. 2.12d, and for A=3 in Fig. 2.12f. As with the estimated unsmoothed MC correlations, the structure of the estimated MC correlations between each VOI and aVOI after smoothing match the corresponding theoretical SENSE induced correlations for each acceleration factor. There are once again additional random low correlations between the VOI and other voxels spread throughout the phantom for all acceleration factors that are merely a result of the noise that was added when generating the data.

2.4.4 Theoretical Functional Connectivity Simulation

To replicate an fcMRI study, a Hamming band pass filter was applied to the time series of every voxel in the smoothed SENSE reconstructed images with A=1, A=2, and A=3 to maintain temporal frequencies between 0.01 and 0.08 Hz. In many fcMRI studies, a cluster of voxels in a particular region defines the seed VOI. For this study, the VOIs selected in Fig. 2.12 were expanded to 2×2 clusters of voxels in the same locations within the anterior of the phantom. To determine functional connectivity about the 2×2 seed

region, the voxel time series were averaged over space to form a single mean time series for the VOI, v. The correlation coefficient, *cc*, between the seed region time series, v, and the time series for each other voxel, s, in the Hamming band pass filtered images reconstructed with each acceleration factor were evaluated using the standard Pearson's coefficient of linear correlation,

$$cc = \frac{\sum_{t=1}^{500} (\mathrm{v}(t) - \bar{\mathrm{V}}) \cdot (\mathrm{s}(t) - \bar{\mathrm{S}})}{\sqrt{\sum_{t=1}^{500} \left(\mathrm{v}(t) - \bar{\mathrm{V}}\right)^2 \cdot \sum_{t=1}^{500} \left(\mathrm{s}(t) - \bar{\mathrm{S}}\right)^2}}, \qquad [2.18]$$

where $\bar{\mathrm{V}}$ and $\bar{\mathrm{S}}$ are the temporal means of voxels v and s respectively. Using Eq. [2.18], the correlation coefficients between the real components of v and s, between the imaginary components of v and s, between the real component of v and the imaginary component of s, and between the magnitude-squared components of v and s were determined for the SENSE reconstructed images with A=1, A=2, and A=3.

An identity covariance structure was used between spatial frequencies in generating the time series of images in each coil for each acceleration factor because the null hypothesis in an fcMRI study assumes no correlation exists between voxels. Should a statistically significant correlation be determined between two brain regions, the null hypothesis is rejected and functional connectivity is assumed between those regions. The fcMRI correlation coefficients determined by Eq. [2.18] for the SENSE reconstructed time series with A=1 are presented in Fig. 2.13a with a threshold of ±0.35 (p≈0.05) (Greicius et al., 2003). As there was no un-aliasing performed on this data set, the "connectivity" noted about the seed VOI is random, and purely a result of the noise added to the data. For the SENSE reconstructed time series that were sub-sampled with A=2 in Fig. 2.13b and with A=3 in Fig. 2.13c, the same induced correlation structure noted in

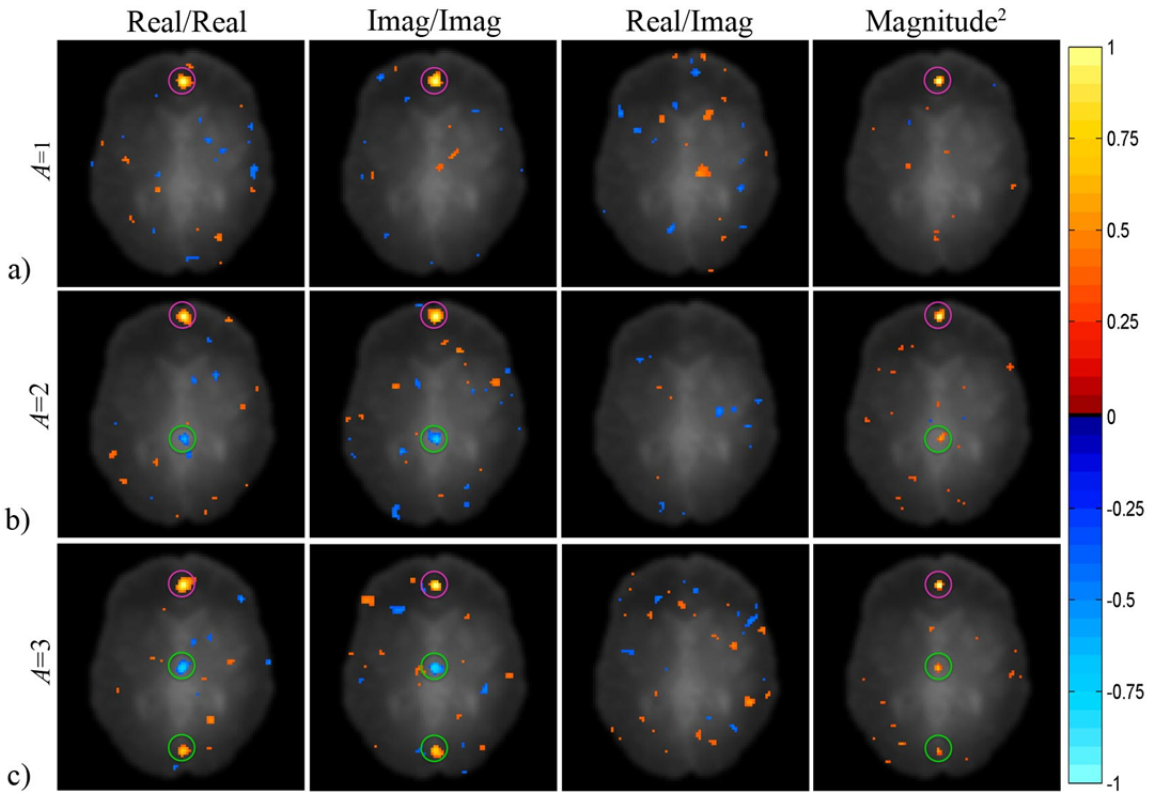

Figure 2.13: Estimated real, imaginary, real/imaginary and magnitude-squared correlations denoting functional connectivity in time series reconstructed by SENSE with a) A=1, b) A=2, and c) A=3 after a temporal Hamming band pass filter was applied to each voxel to maintain frequencies between 0.01 and 0.08 Hz. Correlations are all presented on a smoothed magnitude underlay and threshold to ±0.35.

Fig. 2.11 and Fig. 2.12 are noted between the VOI and aVOIs. As the correlations in Fig. 2.13 are estimated from SENSE reconstructed data sets that have been subjected to a Hamming band pass filter to maintain temporal frequencies between 0.01 and 0.08 Hz, these correlations would reject the null hypothesis in a fcMRI study, implying that the previously aliased voxels are functionally connected. As the data in this illustration was generated with an identity covariance between voxels, all correlations between the seed VOIs in Fig. 2.13 and any other voxels therefore indicate false positives. This implies that the SENSE induced correlations are statistically significant and reside in the frequency spectrum commonly associated with functional connectivity. Moreover, the

position of the selected seed VOI and the aVOIs align themselves very closely to the commonly investigated Default Mode Network in the brain (Raichle et al., 2001; Raichle et al., 2007) in Fig. 2.2, and could therefore corrupt fcMRI conclusions with the potential for incurring Type I & II errors, depending on the sign of the induced correlations and the sign of the correlations inherent in the acquired data.

2.5 Experimental Illustration of SENSE Induced Correlations

2.5.1 Data Acquisition and Reconstruction

To validate the statistical implications of the SENSE model explored in the previous section, a non-task human subject fcMRI data set of 510 TRs was acquired with each of N_C=8 receiver coils through an echo planar imaging (EPI) pulse sequence in a 3.0T General Electric Signa LX magnetic resonance imager. The data set was comprised of four axial slices with 96×96 voxels that were 2.0×2.0×2.5mm in dimension. Each TR in the time series was 1 s in length with an echo time of 45.4 ms, an effective echo spacing of 816 μs, excited by a flip angle of 45°, and an acquisition bandwidth of 125 kHz. Of the 510 TRs, the first 20 were discarded to account for T_1 effects and varying echo times, resulting in 490 TRs acquired under the same conditions. To correct the Nyquist "ghosting" that can result from sampling the odd and even lines of *k*-space in different directions in an EPI acquisition scheme, the center row of *k*-space for each TR in each receiver coil was acquired with three navigator echoes. These extra rows of *k*-space were used to estimate and adjust the error in the center frequency and group delay offsets between the odd and even lines of *k*-space (Nencka et al., 2008). As factors such as respiration and out of field motion can create dynamic fluctuations in the main B-field

of the scanner when using EPI acquisition techniques, the global temporal phase structure was corrected in each coil to account for field shifts associated with gradient heating and RF phase variations (Hahn et al., 2009; Hahn et al., 2012). Additionally, to account for the phase drift in B-field gradients, a plane was fit to and subtracted from the phase in each image in a time series in each coil using the technique outlined in (Jesmanowicz et al., 2011).

To observe the difference between the same data set being fully sampled with A=1 and reconstructed by the SENSE model with A=3, sub-sampling was performed retrospectively by deleting rows of k-space with the PE direction oriented as anterior-posterior. The fully sampled data set was used for estimating coil B-field sensitivity profiles, S, together with the covariance between coils, Ψ, that are used for reconstructing the data set sub-sampled by A=3 with Eq. [2.2]. For a baseline comparison, the data set with A=1 acquired by the N_C=8 coils was combined into a single time series using Eq. [2.2]. After reconstruction, each image in the data sets with A=1 and A=3 were spatially filtered using a Gaussian smoothing kernel with a fwhm of 3 voxels. To observe functional connectivity, a Hamming band pass filter was then applied to the time series of every voxel in the smoothed images reconstructed by SENSE with A=1 and A=3 to maintain temporal frequencies between 0.01 and 0.08 Hz.

2.5.2 Experimental Results

The mean magnitude, mean phase, standard deviation and SNR for the data sets reconstructed by SENSE with A=1 and A=3 and subsequently smoothed with a Gaussian kernel are presented in Fig. 2.14a and Fig. 2.14b respectively. As with the theoretical illustration, the mean magnitude reconstructed images for A=1 and A=3 are visually

similar, which is to be expected since the number of coils is more than double A=3, and thus the spatial localization matrix, S, in Eq. [2.2] is very over determined. Unlike the magnitude, however, there are notable differences in the mean phase within the brain of the images reconstructed with A=1 and A=3. As the SENSE un-aliasing process makes use of coil B-field sensitivity estimates, this difference in the phase is most likely the result of inhomogeneities in the acquired coil B-fields. It is of note that the large FOV of the acquired data set makes the size of the brain small relative to the size of the image. This means that although the full FOV image is folded over on itself A=3 times through the aliasing process, the brain itself only experiences two-fold aliasing, with one of the A=3 aliased voxels falling in space. As noted in the theoretical illustration, the reduced FOV of k-space in the data set sub-sampled by A=3, results in a standard deviation in Fig.

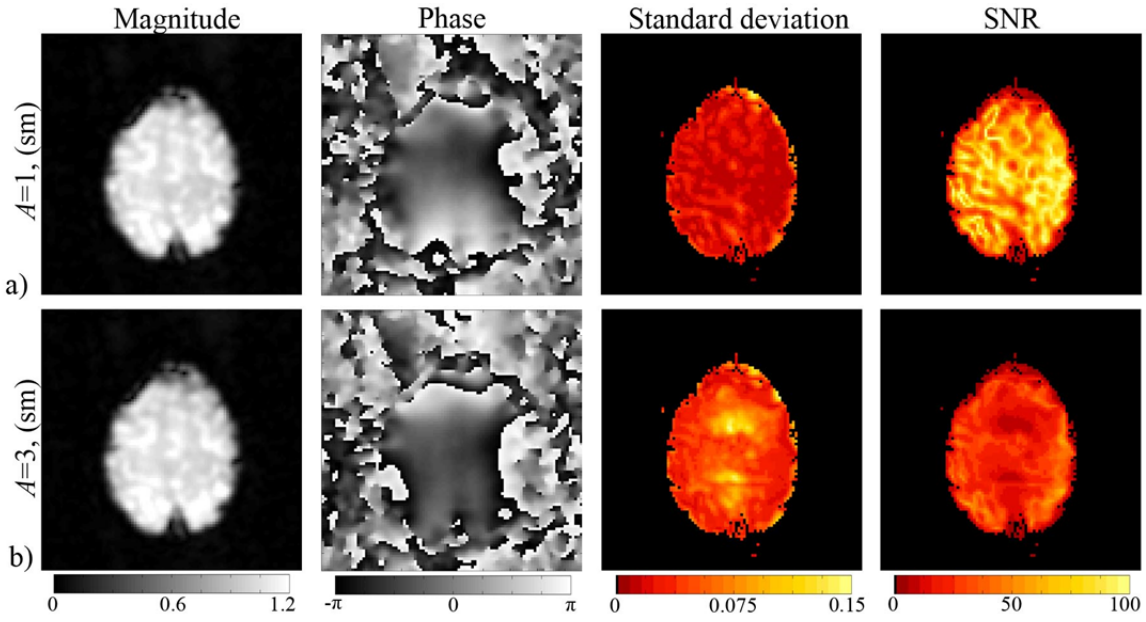

Figure 2.14: Mean magnitude and phase, standard deviation and SNR for images of a human subject reconstructed by SENSE with a) A=1 and b) A=3 together with smoothing.

2.14b that is greater in the areas of two-fold aliasing than that of the fully sampled data set in Fig. 2.14a. Given that SNR is derived by the ratio of the mean magnitude and standard deviation in each voxel, the increase in standard deviation with an increase in A results in a decreased SNR for A=3 in Fig. 2.14b compared to that for A=1 in Fig. 2.14a.

The comparison between the real, imaginary, real/imaginary and magnitude-squared correlations induced by a SENSE reconstruction with A=1 versus A=3 is performed in three ways. First, the theoretical correlations induced by the SENSE reconstruction operators, O_{SE}, together with a smoothing operator, Sm, in Eq. [2.16] were determined through Eq. [1.9] and are presented in Fig. 2.15a for A=1 and Fig. 2.15d for A=3. Second, the correlations estimated directly from the experimentally acquired human subject data sets (EXP) reconstructed with the SENSE model together with smoothing are presented in Fig. 2.15b for A=1 and in Fig. 2.15e for A=3. Finally, the correlations estimated about a 2×2 seed region, determined with Eq. [2.18], in the reconstructed time series after a Hamming band pass filter was applied to each voxel's time series are presented in Fig. 2.15c for A=1 and in Fig. 2.15f for A=3. All correlations in Fig. 2.15 are presented on top of a magnitude underlay with a pink circle highlighting each VOI and green circles highlighting the aVOI's. To illustrate the complete theoretical structure, the images in Fig. 2.15a and Fig. 2.15d show all correlations induced about the VOI by the SENSE model, even if there is a correlation induced between the VOI and voxels in space. All correlation in Figs. 2.15b-c and Figs. 2.15e-f, however, are masked to observe correlations between the VOI and voxels within the brain only. The theoretical correlations induced by SENSE are presented with a threshold of ±0.125 to illustrate the general induced correlation structure, while the correlations estimated from the

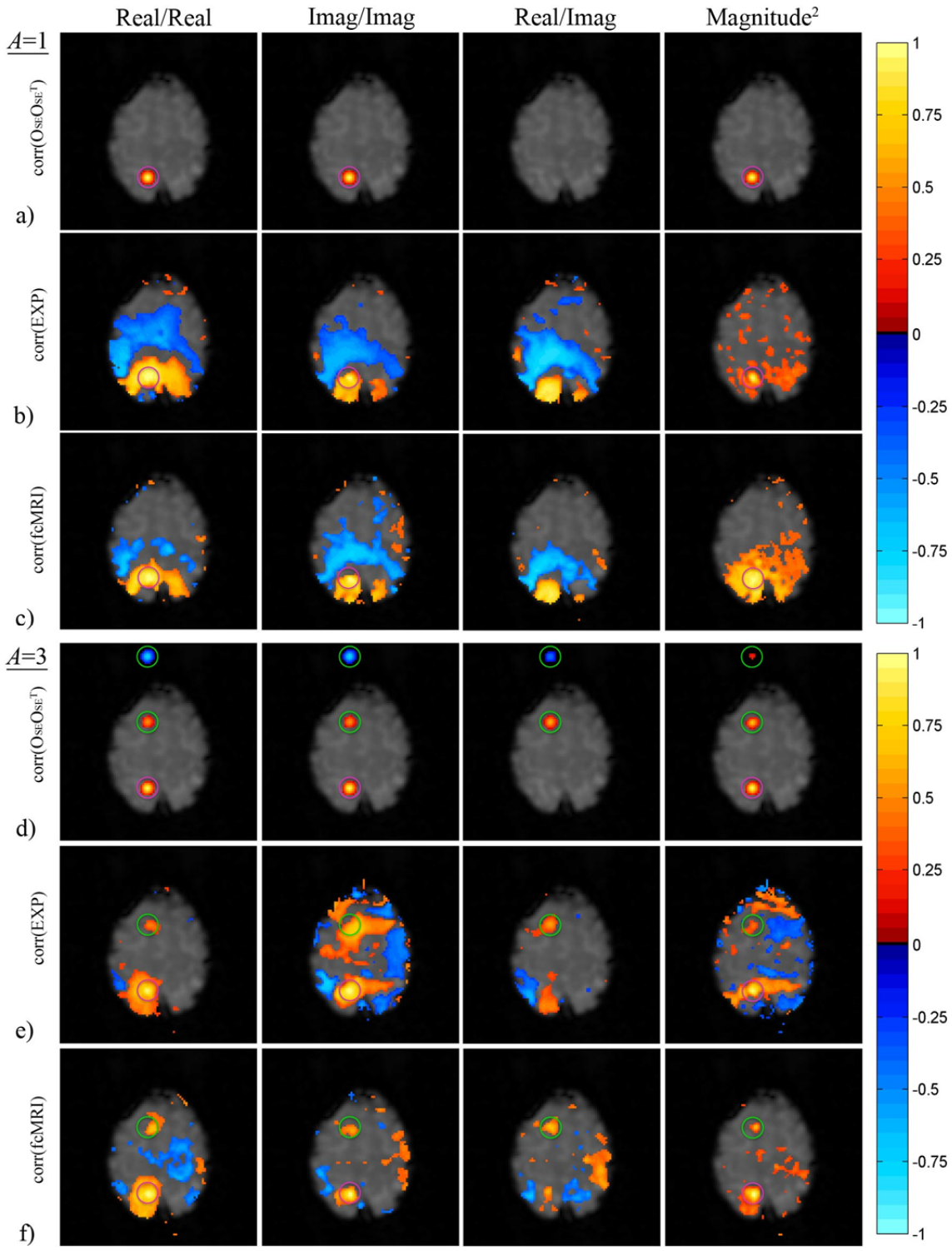

Figure 2.15: Correlations about a VOI for a human subject data set a) theoretically induced by SENSE with A=1, b) estimated from EXP data with A=1, c) fcMRI correlations estimated from Hamming band pass filtered images reconstructed by SENSE with A=1, d) theoretically induced by SENSE with A=3, e) estimated from EXP data with A=3 and f) fcMRI correlations estimated from Hamming band pass filtered images reconstructed by SENSE with A=3. Correlations in a) and d) are threshold to ±0.125 and correlations in b-c) and e-f) are threshold to ±0.35.

reconstructed images with and without band pass filtering are presented with a threshold of ±0.35 (p≈0.05) (Greicius et al., 2003).

As the theoretical correlations presented in Fig. 2.15a are for a SENSE reconstruction with A=1 together with smoothing, the only correlation structure of note is that induced between the VOI and its immediate neighbors by the Gaussian smoothing kernel. The estimated EXP correlations for data reconstructed with A=1 together with smoothing in Fig. 2.15b show positive real, imaginary and real/imaginary correlations in the vicinity of the VOI with negative real, imaginary and real/imaginary correlations across the midbrain region. As the correlations estimated from magnitude-squared data all appear to be positive and strongest in the vicinity of the VOI, the negative real, imaginary and real/imaginary correlations are most likely a byproduct of the phase in the reconstructed images. This could result from inhomogeneities in either the B-fields of the coils that acquired the data or the estimates of the B-field sensitivities that are used to reconstruct the data. When the time series of each voxel in the smoothed images reconstructed by SENSE with A=1 are band pass filtered to the frequency spectrum commonly associated with fcMRI, the correlations representing connectivity in Fig. 2.15c are slightly diminished but still resemble the structure of their un-filtered counterparts in Fig. 2.15b.

With the VOI located in the anterior region of the brain, the aVOIs prior to a SENSE reconstruction with A=3 fall both within the anterior of the brain and in space above the brain. The correlations induced by a SENSE reconstruction with A=3 between the VOI and the real, imaginary, real/imaginary and magnitude-squared components of all other voxels are presented in Fig. 2.15d. As with the theoretical illustration, the real

and imaginary induced correlations are both positive and negative while the correlations induced between the VOI and aVOIs in magnitude-squared data are all positive. Unlike the data set used in the theoretical illustration, there are notable positive and negative correlations induced between the real component of the VOI and the imaginary components of the aVOIs. It is apparent that the estimated EXP correlations for data reconstructed with A=3 together with smoothing in Fig. 2.15e appear to be slightly different to the corresponding EXP correlations estimated from data with A=1 in Fig. 2.15b. These differences are partly a result of the difference in phase between the images reconstructed with A=1 in Fig. 2.14a and the images reconstructed with A=3 in Fig. 2.14b, but most importantly are a result of the real, imaginary, real/imaginary and magnitude squared correlations induced by the SENSE reconstruction between the VOI and the aVOI within the brain. The correlations noted within the green circles of Fig. 2.15e match the sign of and shape their theoretically induced counterparts in Fig. 2.15d. When the time series of each voxel in the smoothed images reconstructed by SENSE with A=3 are band pass filtered to the frequency spectrum commonly associated with fcMRI, the correlations representing functional connectivity in Fig. 2.15f still show positive correlations between the VOI and the aVOI in the green circle. This validates the fcMRI correlations in the theoretical illustration in Fig. 2.13c, suggesting that the artificial correlations induced by the SENSE model reside in the frequency spectrum commonly associated with functional connectivity. As the fcMRI correlations shown in Fig. 2.15c for a data set with no un-aliasing (A=1) exhibit no positive correlations between the VOI and the location of where an aVOI would be in the anterior of the brain, these regions would not be assumed to be functionally connected. However, should a neuroscientist not

account for the implications of the reconstruction and processing operations performed on their data, the notable correlations between the VOI and aVOI after a SENSE reconstruction with A=3 in Fig. 2.15f (which are of no biological origin) would reject the null hypothesis in a functional connectivity study, suggesting that these two regions are in fact functionally connected when they are not.

2.6 Discussion

The SENSE model is one of the most common pMRI models used in most clinical GE MRI scanners. With an array of receiver coils placed around an object in the scanner, the SENSE model offers an attractive means of un-aliasing aliased coil images into a single full FOV image by exploiting the overlap of coil B-fields for spatial localization. As such, many studies (including those funded by the $35m Human Connectome Project) utilize the SENSE model with little to no regard as to the degree to which the model changes the statistical properties of the data. The real-valued isomorphic framework outlined in this chapter provides a novel means of precisely quantifying the structure of the correlations artificially induced by the SENSE model without the need for time-consuming MCMC simulations that can only estimate the structure.

The correlations theoretically induced by the SENSE model have been validated through both theoretical MC and experimental illustrations. The results of both illustrations have shown that when images are sub-sampled with an array of receiver coils by an acceleration factor of A>1, and subsequently un-aliased by the SENSE model, there are unavoidable correlations of no biological origin induced between the A previously aliased voxels. As these correlations still exceed a threshold of ±0.35 after the conventional Hamming band pass filtering of each voxel's time series to frequencies

between 0.01 and 0.08 Hz, the non-biological correlations artificially induced by the SENSE model would be mistaken for regions of apparent functional connectivity with 95% confidence when they are not. When sub-sampling is performed from anterior/posterior, these correlations can fall within the commonly explored default mode network, while sub-sampling from left/right could result in these correlations falling near or within the motor cortices. As such, there is ultimately a need for new methods to accelerate data without inducing such misleading correlations. In the meantime, it is necessary for scientists conducting an fcMRI study that employs models such as SENSE to at least quantify and be aware of the presence of these correlations between regions they may be investigating.

Chapter 3: A Statistical Investigation of the GRAPPA pMRI Model

3.1 The GRAPPA Model

Unlike the SENSE model, where the un-aliasing of aliased coil images is performed in the image domain, the GRAPPA model is characterized as a *k*-space technique because the interpolation of missing coil measurements occurs in the spatial-frequency domain. The original GRAPPA model (Griswold, et al., 2002) represents a more generalized implementation of the VD-AUTO-SMASH approach (Heidemann, et al., 2001), utilizing a variable density (VD) acquisition scheme, only differing in the way in which the missing lines of *k*-space are repopulated. With AUTO-SMASH (Jakob, et al., 1998) and VD-AUTO-SMASH, a collection of fully sampled spatial frequencies are acquired either in the center of *k*-space or separately in full FOV calibration scans and used to generate a single composite array of spatial frequencies from the sub-sampled *k*-space arrays acquired with multiple receiver coils. Using the acquired spatial frequency measurements from all coils, the GRAPPA model generates a full FOV uncombined spatial frequency array for each receiver coil by performing an interpolation of missing lines of *k*-space within each coil array.

When a uniform sub-sampling of *k*-space is performed by an acceleration factor of A in the PE direction, such as that in Fig. 1.1, every A^{th} row of *k*-space is acquired. This spaces the acquired rows $A\Delta k_y$ apart and leaves (A-1) missing rows between measurements. With VD acquisition schemes, additional rows of auto-calibration signal (ACS) measurements are acquired within the center portion of *k*-space. These rows of ACS measurements are positioned where blocks of (A-1) rows of *k*-space would

generally be sub-sampled. This allows one to fit the *k*-space measurements from a collection of N_{row} rows in a single column of all N_C coils, F_l, to the (A-1) additionally acquired calibration measurements in a single coil, F_{calib}. From this fitting process, a set of interpolation weights, w, can be estimated and used to interpolate the missing spatial frequencies for each coil $\xi = [1,2,\ldots N_C]$ by

$$F_{calib,\xi}(k_x, k_y + m\Delta k_y) = \sum_{l=1}^{N_C} \sum_{r=-U}^{D} w(\xi, r, l, m) F_l(k_x, k_y + rA\Delta k_y). \quad [3.1]$$

In Eq. [3.1], m denotes the index of the row being interpolated, $m\Delta k_y$ denotes the frequency offset from the acquired frequency in column k_x and row k_y, the number of rows above (U) and below (D) the calibration measurements, F_{calib}, sum to a total of N_{row} rows in the interpolation kernel, and A is the acceleration factor by which the region of *k*-space is sub-sampled. Since its derivation in (Griswold, et al., 2002), the one-dimensional interpolation in Eq. [3.1] has been adapted (Griswold, 2004; Wang et al., 2005; Griswold, et al., 2006; Brau et al., 2008) to incorporate more than a single column in the interpolation by

$$F_{calib,\xi}(k_x, k_y + m\Delta k_y) = \sum_{l=1}^{N_C} \sum_{c=-L}^{R} \sum_{r=-U}^{D} w(\xi, c, r, l, m) F_l(k_x + c\Delta k_x, k_y + rA\Delta k_y). \quad [3.2]$$

In Eq. [3.2], the number of columns to the left (L) and right (R) of F_{calib} sum to a total of N_{col} columns in the interpolation kernel. If the column index, c, is set to zero (L=R=0), Eq. [3.2] becomes one-dimensional, as in Eq. [3.1]. Once the interpolation kernel weights, w, in Eq. [3.1] or Eq. [3.2] are determined from the fitting the acquired *k*-space measurements to the calibration measurements, they can be used to interpolate all missing frequencies in all coils results in a complete array of spatial frequencies for each

coil, which if combined in either the image or frequency domains produces a single full FOV image after inverse Fourier reconstruction.

To reduce artifacts in the reconstructed images, interpolation weights need to be derived from a dataset with a sufficient SNR by using training data either in the form of additional ACS lines in the center of *k*-space, or through full FOV pre-calibration scans (Larkman, 2007). In theory, if multiple ACS lines are acquired in the center of *k*-space, with the remainder of *k*-space sub-sampled uniformly, "auto-calibration" is achieved in the interpolation of missing spatial frequencies for a single data set within a time series. This has a potential advantage over the SENSE model, where calibration images are acquired before the sub-sampled data set and used to reconstruct the entire time series, as each image becomes independent, with no effects of motion and other temporally varying artifacts. Furthermore, the additionally acquired ACS lines can be incorporated into the final reconstructed image and allow higher acceleration factors to be used in the sub-sampled region of *k*-space. However, despite their advantages, VD acquisition schemes suffer from varying effective inner-echo spacing if acquired using an EPI pulse sequence. As such, a uniform sub-sampling scheme is often used (as in this dissertation), with interpolation weights in Eq. [3.2] estimated from full FOV pre-calibration scans.

For a given collection of N_{col} columns and N_{row} rows of acquired spatial frequencies, the contribution from each acquired measurement is determined by the relative distance between that measurement and the block of (A-1) missing measurements to be interpolated, as described in Eq. [3.2]. If the spacing between all acquired *k*-space measurements is constant, as can be assumed with an EPI pulse sequence, the weights used in repopulating the missing lines of *k*-space in the GRAPPA interpolation can be

considered to be shift invariant (Griswold et al., 2002). This effectively implies that the same kernel of interpolation weights can be used for all missing spatial frequency measurements that have the same spacing between the acquired measurements. Illustrated in Fig. 3.1, for an application of Eq. [3.2] with to an array of N_C coils using a kernel of size N_{row} rows by N_{col} columns, sub-sampled with A=2, Eq. [3.2] can be applied to interpolate all coils at once using a matrix representation of Eq. [3.2] by

$$f_{calib} = w\, f_l. \qquad [3.3]$$

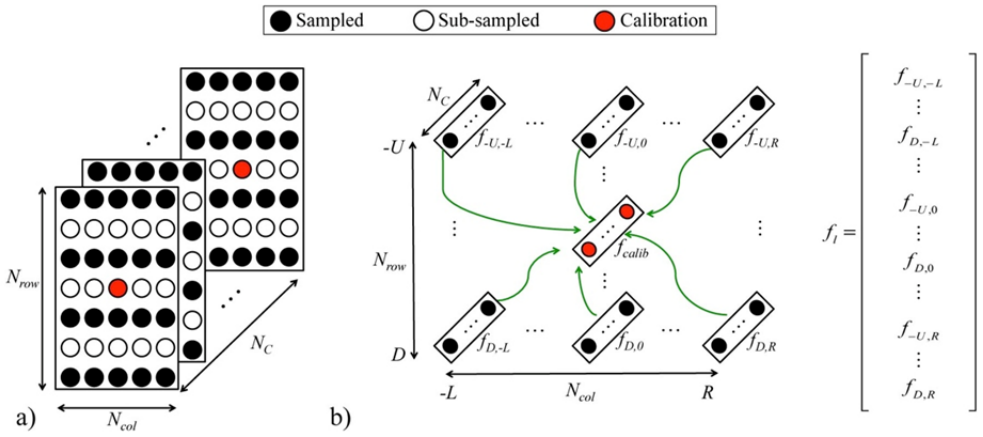

Figure 3.1: Fitting the sampled spatial frequencies in a) all N_C coils with an interpolation kernel of size N_{col} columns and N_{row} rows, b) to a vector of all N_C calibration measurements, f_{calib}, with the of sampled spatial frequencies, f_l, for a column-wise implementation of the 2D GRAPPA operator.

Illustrated in Fig. 3.1b, with red dots denoting ACS calibration measurements, f_{calib} in Eq. [3.3] is a $(A\text{-}1)N_C \times 1$ column vector with N_C sub-vectors of the $(A\text{-}1)$ complex-valued calibration k-space measurements from each coil. In this dissertation, a column-wise application of Eq. [3.2] is employed. As shown with black dots denoting the sampled measurements in Fig. 3.1b, the vector f_l in Eq. [3.3] is constructed by first stacking the complex-valued acquired spatial frequencies from the N_C coils into vectors.

Moving through the kernel from top to bottom and left to right, the N_{row} vectors of length N_C in each column are stacked into N_{col} vectors, which are in turn stacked into the single vector in Fig. 3.1b, f_l, of length $N_{row}N_{col}N_C$. Using a least squares estimation, one can solve for the $(A\text{-}1)N_C \times N_{row}N_{col}N_C$ matrix of complex-valued weights in Eq. [3.3] by

$$w = f_{calib} f_l^H (f_l f_l^H)^{-1}. \quad [3.4]$$

To interpolate (A-1) missing spatial frequencies in N_C coils with a kernel of size N_{row} by N_{col}, the estimation of interpolation weights requires at least $N_{fits} \geq N_{row}N_{col}N_C(A\text{-}1)$ fits between acquired and calibration measurements in Eq. [3.2]. Shifting through the available calibration data using the techniques outlined in (Griswold et al., 2002; Breuer et al., 2009; Park et al., 2005; Park et al., 2012), the vector f_{calib} and f_l in Eq. [3.3] for each of the N_{fit} fits are stacked into the columns of matrices $F_{calib}=[f_{calib,1},\ldots f_{calib,Nfits}]$ and $F_l=[f_{l,1},\ldots f_{l,Nfits}]$ respectively, allowing for the interpolation weights to be determined by

$$w = F_{calib} F_l^H (F_l F_l^H)^{-1}. \quad [3.5]$$

The interpolation weights in Eq. [3.5] are of a higher rank than those in Eq. [3.4], and can therefore more appropriately account for (among other things) measurement error and noise, the oscillations between positive and negative spatial frequencies, and the variation in amplitude between high frequencies at the edge of k-space low frequencies in the center of k-space.

3.2 Real-Valued GRAPPA Isomorphism

As the interpolation process performed by the GRAPPA model in Eq. [3.1] and Eq. [3.2], by definition, induces a local covariance between the acquired and interpolated spatial frequency measurements, this covariance will become a global covariance between the voxels in the inverse Fourier reconstructed image. The interpolation kernel

weights, w, in Eq. [3.1] and Eq. [3.2] are generated from fully sampled spatial frequency measurements, either in the form of pre-calibration scans or additional ACS lines in the center of k-space. As these measurements are derived from the Fourier transform of coil B-field sensitivities, the GRAPPA interpolation essentially performs a sensitivity encoding (Pruesmann et al., 1999) in k-space by convolving the sub-sampled k-space measurements with the Fourier transform of the B-field sensitivities of each of the N_C receiver coils. As such, the covariance induced between voxels in the image reconstructed by the GRAPPA interpolation process is expected to be greatest between previously aliased voxels, similar to those induced by the SENSE model in the previous chapter, with an additional covariance structure that is lower in value and induced throughout the reconstructed image.

To quantify the true structure of the induced covariance (and in turn correlation), an isomorphic representation of the complex-valued GRAPPA model is presented to interpolate all missing complex-valued spatial frequencies in all coils at once using real-valued matrix operators. Similarly to the isomorphic representation of the SENSE model in Chapter 2, representing the interpolation process undertaken in the GRAPPA model as a series of real-valued matrices enables one to observe the statistical implications of each step in the process as well as the implications of the process as a whole. Furthermore, the GRAPPA interpolation process depends on a variety of parameters that include the acceleration factor, the number of coils and the size of the interpolation kernel. A framework of this kind can therefore provide a means of investigating the degree to which each parameter influences the correlation structure induced by the GRAPPA model.

When voxels are assumed to have an identity covariance structure in the SENSE model, the un-aliasing process is performed on each aliased voxel separately. This means that no two aliased voxels implement the same acquired measurements or sensitivities values during the un-aliasing process. When an interpolation kernel used in the GRAPPA model is shifted from interpolating a block of (A-1) missing spatial frequencies in one row and column to interpolating a block of (A-1) missing spatial frequencies in a neighboring row or column, the same acquired spatial frequency measurements might be used in both interpolations. This complicates the linearization of the GRAPPA model compared to that of SENSE, as there are many ways in which the real-valued isomorphism of the GRAPPA model can be formatted. In this dissertation, the GRAPPA interpolation process is performed on a column-by-column basis (as opposed to interpolating on either a row-by-row or coil-by-coil basis) and thus the initial data vector, f_{coil}, as used in the SENSE model in Fig. 2.3 and Eq. [2.6], is permuted accordingly.

Re-illustrated on the right side of Fig. 3.2, the complex-valued array of sub-sampled spatial frequencies, $F_{\xi,C}$, from each of $\xi=[1,\ldots,N_C]$ receiver coils in an array is vectorized by stacking the rows of the real component of $F_{\xi,C}$ into a vector, $f_{\xi,R}$, stacking the rows of the imaginary component of $F_{\xi,C}$ into a vector, $f_{\xi,I}$, and then concatenating the real and imaginary component vectors for coil ξ into vectors, $f_{\xi} = [f_{\xi,R}^{T}, f_{\xi,I}^{T}]^{T}$. The real-valued vectors of spatial frequencies for each of the N_C receiver coils are finally concatenated into a single real-valued vector, f_{coil}, with alternating sub-vectors of the real and imaginary spatial frequencies from all N_C coils. To perform the GRAPPA interpolation, a complex permutation, P_{C_I}, which is different from P_C in the SENSE model in Eq. [2.8], is applied to reorder f_{coil} to having all real spatial frequencies from all

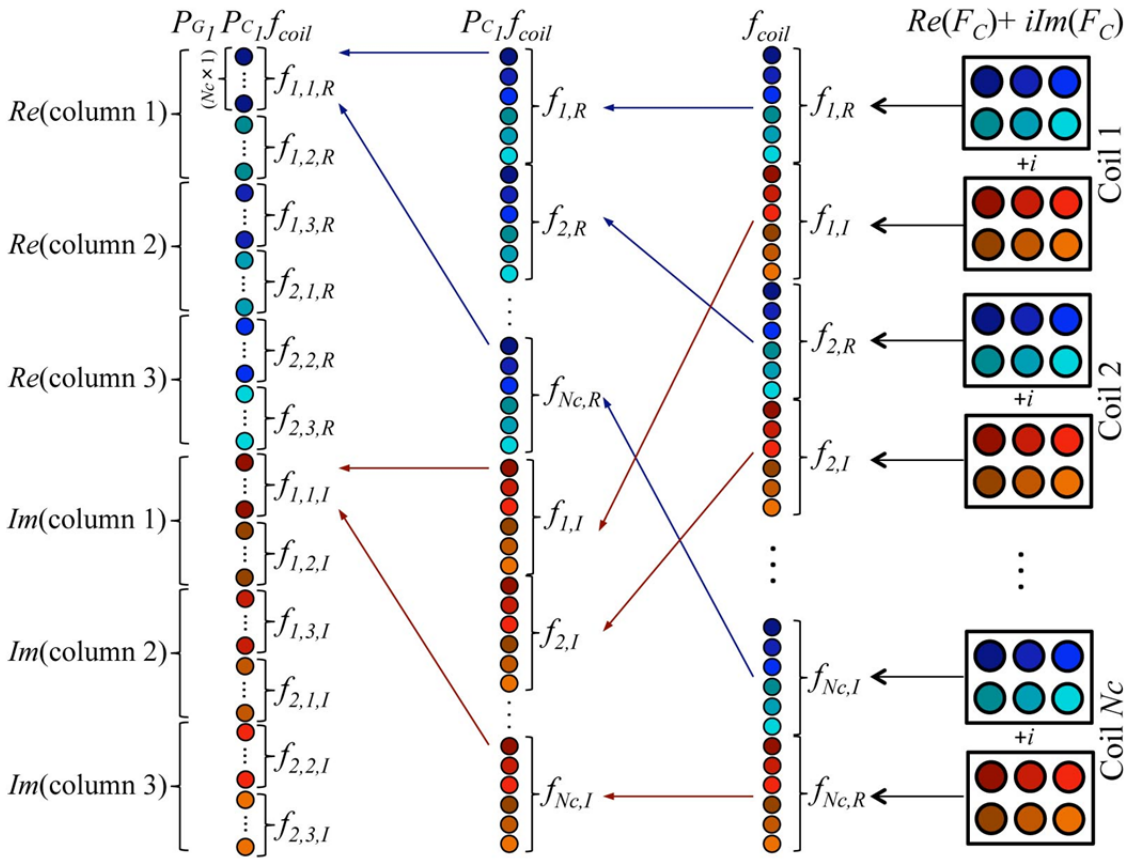

Figure 3.2: The real-valued vector, f_{coil}, formed by vectorizing and concatenating the real and imaginary components of the sub-sampled *k*-space arrays from each of N_C coils is permuted by P_{C_1} to having all real values from all N_C coils stacked upon all imaginary values from all N_C coils, and then permuted by the GRAPPA sorting permutation, P_{G_1}, to being ordered first by column, then by row, and finally by coil.

N_C coils stacked upon all imaginary spatial frequencies from all N_C coils, as illustrated by $P_{C_1} f_{coil}$ in Fig. 3.2. In order to interpolate the missing rows of *k*-space on a column-by-column basis, the vector, $P_{C_1} f_{coil}$, is permuted once more by a GRAPPA sorting permutation, P_{G_1}, such that the resulting vector,

$$f_G = P_{G_1} P_{C_1} f_{coil}, \qquad [3.6]$$

has spatial frequencies ordered first by column, then by row, and finally by coil, as illustrated on the left side of Fig. 3.2.

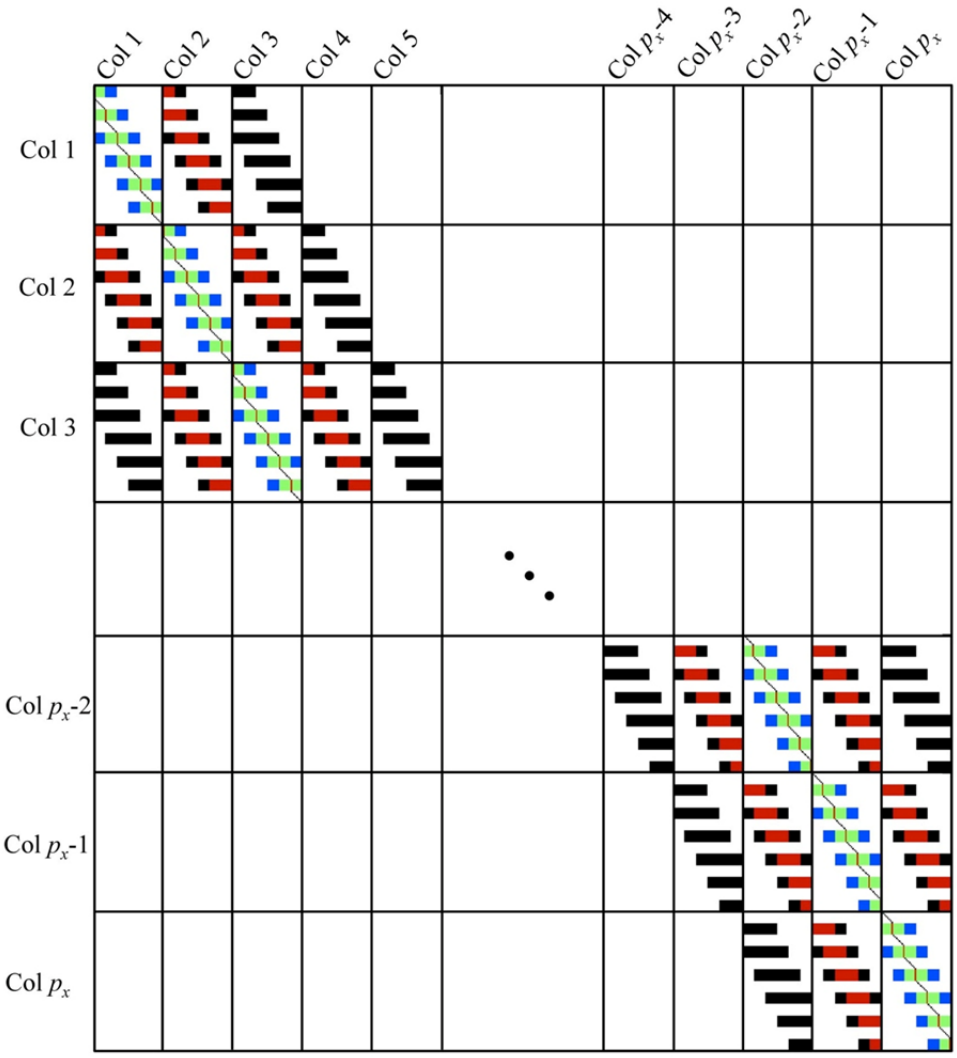

Figure 3.3: The complex-valued GRAPPA interpolation operator, G_C, with kernels of size (N_{cols}×N_{rows}): 2×1 (green), 4×1 (green and blue), 2×3 (green and red), and 4×5 (green, blue, red, and black).

With the permuted spatial frequency vector, f_G, ordered by column, the interpolation weights, w, can be appropriately segmented and placed along various diagonals of the matrix G_C in Fig. 3.3 to perform the interpolation. In Fig. 3.3, the toy example from Fig. 3.2 is expanded to having p_x columns, with p_y=12 rows that are sub-sampled by A=2 in N_C coils. For each block of (A-1)N_C missing spatial frequencies, the complex-valued weights, signified by the blocks of varying color in Fig. 3.3, are

positioned such that the appropriate rows and columns of acquired measurements are employed in the interpolation in Eq. [3.2]. In Fig. 3.3, the 1-dimensional complex-valued GRAPPA interpolation performed in Eq. [3.1], with a kernel of size 2×1 (N_{cols}×N_{rows}), is represented by the green blocks, while an interpolation with a kernel of size 4×1 is represented by a combination of the green and blue blocks. The vertical red line in the center of these kernels denotes the "middle" of the kernel, and thus weights to the left of this line will be applied to rows of acquired spatial frequencies above the (A-1)N_C missing spatial frequencies, and weights to the right of this line will be applied to rows of acquired spatial frequencies below the missing frequencies. For the 2-dimensional GRAPPA model in Eq. [3.2] to be applied using a matrix operator, the matrices of weights, w, need to be partitioned and placed in such a way that the partitions perform a linear combination of the appropriate measurements in f_G, corresponding to the neighboring columns of the (A-1)N_C missing spatial frequencies being interpolated. The 2-dimensional complex-valued GRAPPA interpolation with a kernel of size 2×3 is represented in Fig. 3.3 by a combination of the green and red blocks, while an interpolation with a kernel of size 4×5 is represented by a combination of the green, blue, red and black blocks. With p_y/A=6 acquired rows, there are six total rows to be interpolated, and thus each column listed down the left side of Fig. 3.3 has six blocks, one for each missing row. To maintain all acquired rows in the refilled array, N_C×N_C real-valued identity matrices are positioned between the blocks of weights. The result of combining the six blocks of weights for the missing rows and the six identity matrices for the acquired rows is a total of p_y=12 rows in the interpolated frequency vector. While one could utilize a variety of techniques to refill the measurements near the edge of k-space

(zero-filling, symmetry, wraparound etc.), partial kernels were used in this dissertation for simplicity, with weights estimated specifically for each edge condition.

To apply the complex-valued GRAPPA matrix operator, $G_C=(G_R+iG_I)$, in Fig. 3.3 to the real-valued permuted vector, f_G, in Eq. [3.6], a real-valued representation of G_C is formed by

$$G=\begin{bmatrix} G_R & -G_I \\ G_I & G_R \end{bmatrix},$$

where G_R and G_I are the real and imaginary components of G_C. The product Gf_G results in a vector of length $2N_Cp_xp_y$ with a combination of both sampled and interpolated spatial frequencies, ordered in the same fashion as f_G. The refilled vector of spatial frequencies therefore needs to be re-permuted to the original format of f_{coil} using the reverse of the operations in P_{C_1} and P_{G_1} with permutations P_{C_2} and P_{G_2} respectively. The permutations P_{C_2} and P_{G_2} are of a larger dimension than P_{C_1} and P_{G_1} given the combination of both acquired and interpolated values in Gf_G. The resulting vector,

$$f_{full} = P_{C_2} P_{G_2} G f_G,$$

therefore contains full FOV spatial frequencies for each of the N_C coils, with vectors of the real frequency values for each coil, stored by row, stacked upon vectors of the imaginary values for the corresponding coil, in an order similar to that of f_{coil} in Fig. 3.2.

To reconstruct the vector of coil spatial frequencies, f_{full}, into a vector of coil voxel values, the real-valued matrix representation of the complex-valued inverse Fourier transform, Ω, in Eq. [1.3] is used. At this stage, one can either inverse Fourier reconstruct each coil image using a Kronecker product, $(I_{N_C}\otimes\Omega)$, and apply a combination matrix, C, to perform the combination of coil images in the image domain,

$$y = C(I_{N_C} \otimes \Omega) f_{full},$$

or, to reduce the demand on computational resources, combine the coil frequencies in *k*-space and inverse Fourier reconstruct the combined spatial frequencies to get a single combined image vector of voxel values,

$$y = \Omega C f_{full}. \quad [3.7]$$

In most studies, a root-sum-of-squares (RSS) combination of coil images is performed with the phase portion of the reconstructed data discarded (Griswold et al., 2002). However, the RSS combination is not a linear operation, and it has been shown that the phase portion of the reconstructed data can provide important biological information about the brains vasculature (Menon et al., 2002; Rowe and Logan, 2004; Rowe and Logan, 2005; Rowe et al., 2005; Nencka et al., 2007; Rowe, 2009). As such, the combination matrix used in this dissertation, C, performs a complex linear combination, generating a $2p_x p_y \times 1$ vector of real combined spatial frequencies stacked upon a $2p_x p_y \times 1$ vector of imaginary combined spatial frequencies in Eq. [3.7]. The combined full FOV vector of spatial frequencies, Cf_{full}, is the exact same size and in the same order as the vector f in Eq. [1.3].

3.3 GRAPPA Induced Correlations

The complete set of matrix operators used in the GRAPPA image reconstruction isomorphism is

$$O_G = \Omega C P_{C_2} P_{G_2} G P_{G_1} P_{C_1}, \quad [3.8]$$

and thus the final reconstructed image vector, y, can be obtained from the original vector of observed *k*-space measurements, f_{coil}, by

$$y = O_G f_{coil}. \quad [3.9]$$

Additional operators for pre-processing in *k*-space, O_K, and post-processing in image space, O_I, can be incorporated into Eq. [3.8] by

$$O_G = O_I \Omega C P_{C_2} P_{G_2} G P_{G_1} P_{C_1} O_K. \quad [3.10]$$

As no pre-processing operations are performed in this dissertation, the assumption that $O_K=I$ will be made unless stated otherwise. The data vector f_{coil} in Eq. [3.9] is described by the sum of a vector of mean spatial frequency measurements, $E[f_{coil}]=f_0$, with added measurement error that has the covariance structure, $\text{cov}(f_{coil})=\Gamma$. When the GRAPPA reconstruction operator in Eq. [3.8] is applied to the vector f_{coil}, the reconstructed image vector, y, in Eq. [3.9] will have a mean of $E[y]=O_G f_0$ and a modified covariance of

$$\Sigma_G = \text{cov}(y) = O_G \Gamma O_G^T. \quad [3.11]$$

In order to determine the covariance structure induced solely by the GRAPPA reconstruction operators in Eq. [3.8], the covariance matrix, Γ, is assumed to be identity, simplifying Eq. [3.11] to

$$\begin{aligned} \Sigma_G &= O_G O_G^T \\ &= O_I \Omega C P_{C_2} P_{G_2} G P_{G_1} P_{C_1} P_{C_1}^T P_{G_1}^T G^T P_{G_2}^T P_{C_2}^T C^T \Omega^T O_I^T. \end{aligned} \quad [3.12]$$

Under the assumption that $\Gamma=I$, any non-zero terms in the off diagonal elements of Σ_G denote an artificial covariance (and in turn correlation) induced by the GRAPPA model between voxels in the reconstructed image vector, y. It is important to note that such an induced covariance is purely a result of the GRAPPA interpolation and reconstruction process, and is of no biological origin whatsoever.

Since all of the permutations in Eq. [3.8] simply rearrange the data that they pre-multiply, they are orthonormal and do not induce any covariance,

$$P_{G_1} P_{G_1}^T = P_{C_1} P_{C_1}^T = I.$$

The covariance of the images reconstructed using the GRAPPA image reconstruction operators in Eq. [3.12] therefore simplifies to

$$\Sigma_G = \Omega C P_{C_2} P_{G_2} G \, G^T P_{G_2}{}^T P_{C_2}{}^T C^T \Omega^T. \quad [3.13]$$

As the GRAPPA operator, G, interpolates missing spatial frequency measurements from acquired measurements, it is not orthogonal, and thus the product GG^T results in an induced covariance structure that is not strictly diagonal. While the subsequent permutations, P_{G_2} and P_{C_2}, are orthonormal, inducing an identity covariance when multiplied by their respective transposes, the fact that they pre-multiply the non-orthogonal GRAPPA operator, G, means that the each permutation will rearrange the GRAPPA induced covariance structure, GG^T. By themselves, both the inverse Fourier transform operator, Ω, and the complex averaging operator, C, are orthogonal, resulting in diagonal covariance structures when multiplied by their respective transposes. As with the permutations, P_{G_2} and P_{C_2}, however, the data vectors that the operators Ω and C pre-multiply each have a covariance structure that is not identity. This means that the applications of both Ω and C will further alter the covariance induced by the GRAPPA operator, G, that was re-ordered by the permutations P_{G_2} and P_{C_2}.

3.3.1 The Effects of Kernel Size on GRAPPA Induced Correlations

While the covariance (and correlation) induced by both the SENSE and GRAPPA models is dependent on the acceleration factor, A, and the number of receiver coils, N_C, the GRAPPA interpolation is also dependent on the dimensions of the interpolation kernel, $N_{cols} \times N_{rows}$. As such, an investigation is performed on the degree to which variations in both the acceleration factor and the dimensions of the interpolation kernel

affect the correlations induced by the GRAPPA model about a seed voxel in the reconstructed images. The correlation induced between all voxels in y, solely by the GRAPPA image reconstruction process, is derived by

$$\text{corr}(O_G O_G^T) = D_G^{-1/2} O_G O_G^T D_G^{-1/2}, \quad [3.14]$$

where the operator O_G from Eq. [3.8] is used with no additional pre- or post-processing, and $D_G = diag(O_G O_G^T)$ is a diagonal matrix with elements that are the reciprocal square root of the variances drawn from the diagonal of the covariance matrix $O_G O_G^T$. When the theoretical correlation matrix determined by Eq. [3.14] is partitioned into the four quadrants in Eq. [1.10], the correlations induced between all real measurements in y, between all imaginary measurements, and between all real and imaginary measurements can be obtained. Additionally, provided with the correlations in Eq. [3.14] and a mean reconstructed image vector, the correlations induced between magnitude-squared measurements can be obtained using the method outlined in (Nencka et al., 2009; Rowe and Nencka, 2009).

Presented in Fig. 3.4 are the real, imaginary, real/imaginary and magnitude squared correlations theoretically induced by the GRAPPA model about a VOI in the center of the pink circles for widely used acceleration factors of A=2 and A=3, and interpolation kernels of size 4×1, 2×3 and 4×5. Using a Shepp-Logan phantom for an underlay, the structure of the correlations in Fig. 3.4 were accentuated by applying a threshold of $\pm 10^{-7}$, selected to be very close to zero, and any additional correlations outside of the induced structure (resulting from machine size error for values near zero) were set to zero. As the GRAPPA model effectively performs a spatial localization in k-space by using a truncated convolution kernel that is derived from the Fourier transform

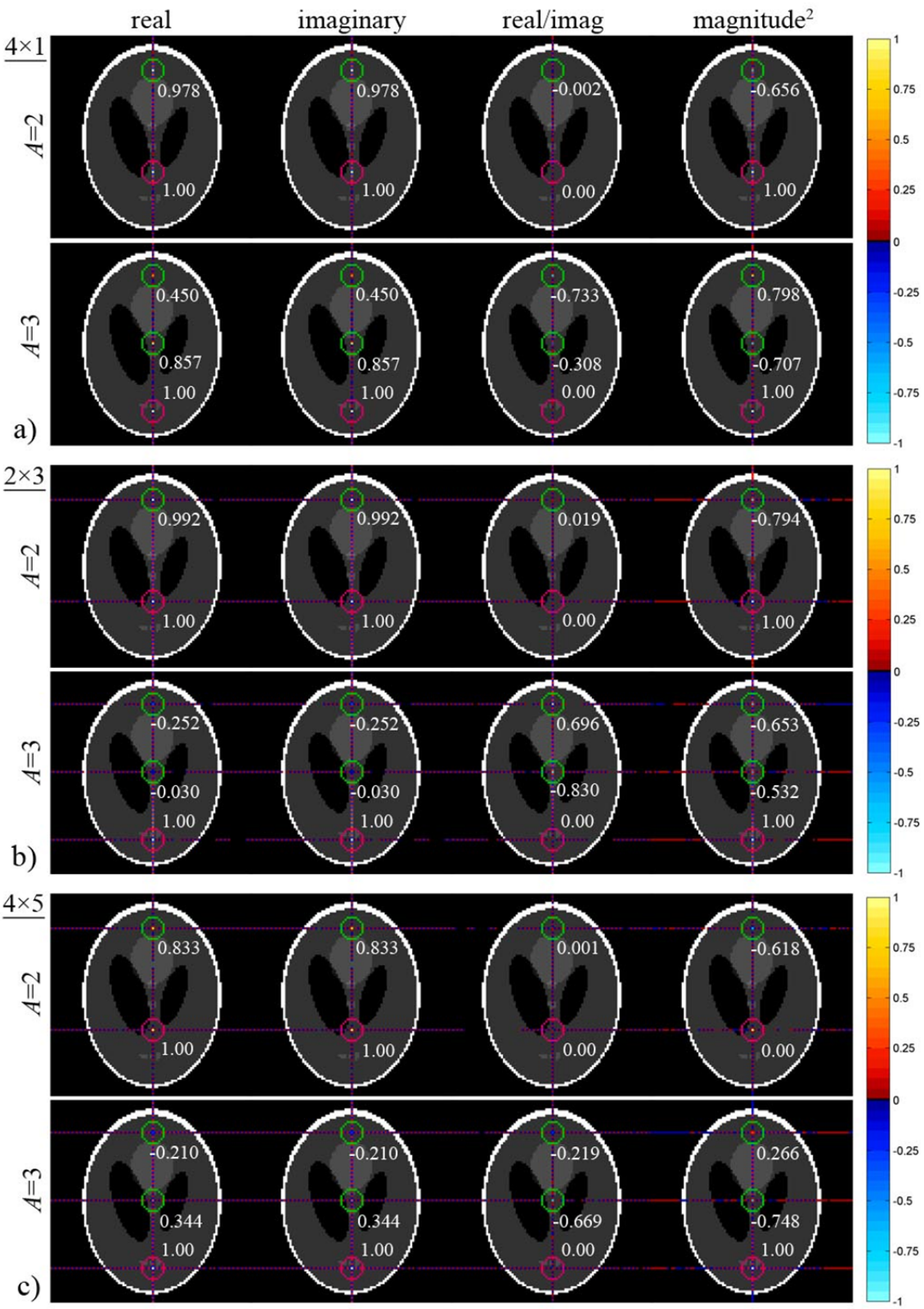

Figure 3.4: Correlations induced between real voxel values, imaginary voxel values, between the real and imaginary voxel values and between magnitude-squared voxel values for a GRAPPA reconstruction with acceleration factors of A=2 and A=3 using interpolation kernels of size a) 4×1, b) 2×3, and c) 4×5.

of the N_C coil B-field sensitivity profiles, the real, imaginary and magnitude-squared correlations in Fig. 3.4 are strongest between the VOI and the aVOIs, in the centers of the green circles, as expected. The theoretical correlations induced between the VOI and aVOIs are stated adjacent to the respective voxel in each image of Fig. 3.4, and appear, on average, to be inversely proportional to the acceleration factor and size of the kernel. The correlations induced between the VOI and the two aVOIs with A=3 are lower in strength than those induced between the VOI and the aVOI with A=2, which is most likely the result of the correlation being distributed between the aVOIs. When a kernel incorporates more rows and columns of k-space measurements into the interpolation, the relative weighting of each measurement is decreased, which is likely the reason why the induced correlations for kernels of size 4×5 appear lower than those of size 2×3. In all images in Fig. 3.4, there is a notable vertical band of correlations induced about the VOI and the column of voxels in which the VOI resides. This correlation results from interpolations performed across rows in the PE direction in which data was sub-sampled. For the 2×3 and 4×5 two-dimensional kernels, there are additional correlations induced between the VOI and voxels in the rows in which both the VOI and the aVOIs reside. These correlations are a result of the interpolation performed across columns in the fully sampled FE direction. Upon close observation, these vertical and horizontal bands exhibit an approximately sinc correlation structure with amplitudes and periods relative to the dimensions of the truncated rectangular kernels. With the local correlation between neighboring spatial frequencies in k-space induced by a rectangular convolution kernel, it is understandable to observe a sinc correlation structure in the image domain after the spatial frequencies are inverse Fourier reconstructed. The negative magnitude-squared

correlation induced between the VOI and aVOIs in Fig. 3.4 with both A=2 and A=3 results from a combination of the expected values and the covariance between the two previously aliased voxels. The sign of the magnitude-squared correlation between the VOI and aVOI can therefore change from one voxel to the next.

3.4 Theoretical Illustration of GRAPPA Induced Correlations

3.4.1 Data Generation

To explore the statistical implications of the GRAPPA reconstruction process, the same three time series generated in section 2.4.1 for a statistical investigation of the SENSE model were reconstructed with the GRAPPA model. The time series of 500 TRs with no sub-sampling performed, A=1, is once again used for both determining the interpolation weights used in the GRAPPA model and serves as a baseline for comparisons with higher acceleration factors. In section 2.4.1, the data was generated to have a maximal SNR of 50 in the 96×96 fully sampled inverse Fourier reconstructed images for the N_C=8 coils. This was done by scaling the magnitude of the coil images to having a maximum of 50 and adding normally distributed random noise to the k-space array for each coil with a mean of zero and a standard deviation of $\sqrt{p_x p_y} = \sqrt{96 \cdot 96}$. The noise added to each of the three data sets generated in section 2.4.1 also assumed the covariance structure listed in Table 2.1 between the coils. This covariance structure was estimated from experimentally acquired data and used in the SENSE un-aliasing process in Eq. [2.2]. The GRAPPA model, however, does not employ any such covariance

structure in the interpolation process in Eq. [3.2], even if the data itself is acquired or generated with a non-identity covariance between coils.

3.4.2 Data Reconstruction and Processing

To interpolate the missing spatial frequencies in the data sets sub-sampled by A=2 and A=3, a 4×5 GRAPPA interpolation kernel was used. The weights used in the GRAPPA interpolation in Eq. [3.2] were determined for the interpolations with both A=2 and A=3 by inserting the fully sampled data set with A=1 into Eq. [3.5]. Once the interpolation weights for each acceleration factor were determined, the missing lines of k-space in the sub-sampled data sets were interpolated from the acquired lines using Eq. [3.2]. With N_C fully sampled arrays of k-space for the data set generated with A=1, and N_C refilled arrays of k-space for the data sets sub-sampled by A=2 and A=3, a combined k-space array for each data set was formed with a complex-valued average performed over the coil dimension. The combined array of spatial frequencies in each of the 500 TRs for all three acceleration factors were then inverse Fourier reconstructed into time series of full FOV combined images. As most fcMRI studies use spatial filtering to increase CNR (Lowe & Sorenson, 1997), smoothing was performed by convolving each reconstructed image in the three time series with a Gaussian smoothing kernel that had a fwhm of 3 voxels.

3.4.3 Results

The mean magnitude and phase images from the reconstructed time series with A=1, A=2, and A=3 are presented in Fig. 3.5a, Fig. 3.5b, and Fig. 3.5c respectively. Unlike the magnitude and phase of the SENSE reconstructed images in Fig. 2.10, the

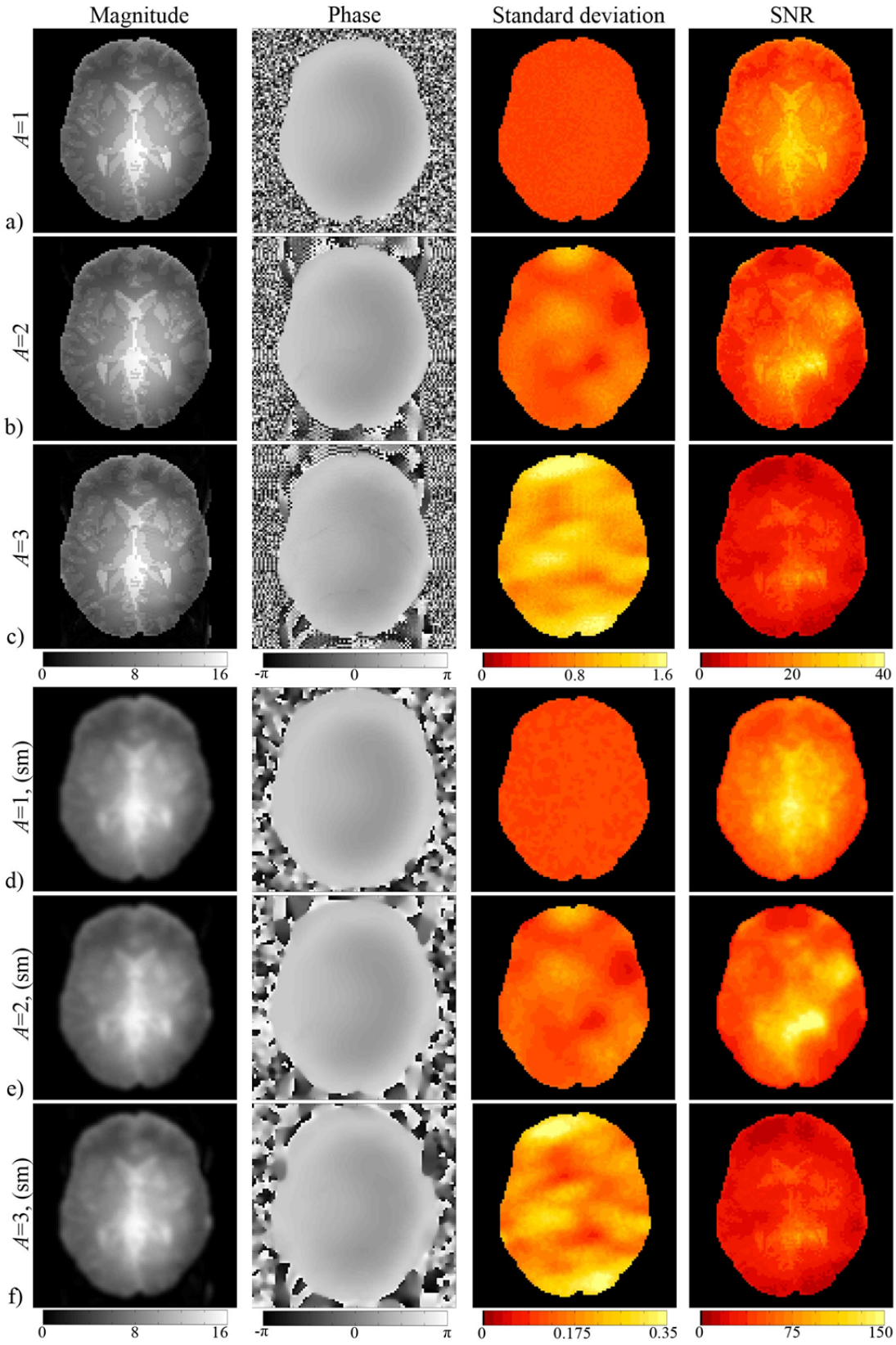

Figure 3.5: Mean magnitude and phase, standard deviation and SNR for GRAPPA reconstructed images with a) A=1, b) A=2, c) A=3, as well as d) A=1, e) A=2, and f) A=3 with smoothing.

mean magnitude and phase reconstructed images with A=2 in Fig. 3.5b and A=3 in Fig. 3.5c show apparent signs of residual aliasing as a result of the GRAPPA reconstruction process. Upon close observation, the aliasing is noticeable within the phantom in both the magnitude and phase, but is most apparent in the space surrounding the phantom in the phase for both acceleration factors. To reconstruct data with A=1 in the GRAPPA model, the operator G in Eq. [3.8] is treated as an identity matrix, as no interpolation is performed, and a complex-valued averaging of interpolated k-space arrays is performed with the operator C before an inverse Fourier reconstruction. With such a combination, the standard deviation for data reconstructed with A=1 in the GRAPPA model in Fig. 3.5a is relatively uniform throughout the phantom. In the SENSE reconstruction with A=1 in Fig. 2.10a, the standard deviation appears to have a "smooth" texture throughout the phantom due to the coil sensitivity weighting in the combination of the coil images. As with the un-aliasing process performed by the SENSE model, the interpolation of missing spatial frequencies in sub-sampled arrays results in full FOV reconstructed images that have an increased standard deviation. As illustrated in Fig. 3.5b for A=2 and in Fig. 3.5c for A=3, there is an apparent increase in the standard deviation with acceleration factor. While the regions of increased standard deviation in images reconstructed with the SENSE model in Fig. 2.10 are clearly defined by the areas of aliasing, the regions of increased standard deviation after a GRAPPA reconstruction are not as clearly defined. Although these regions of increased standard deviation in the GRAPPA reconstructed images are still predominantly within regions that were previously aliased, there is also a notable increase in the standard deviation in the regions without aliasing. The result of this increase in standard deviation with acceleration factor

is marked by a decrease in the SNR of GRAPPA reconstructed images. As the acceleration factor increases from A=1 in Fig. 3.5a to A=2 in Fig. 3.5b to A=3 in Fig. 3.5c, the SNR decreases within all regions of the phantom in which the standard deviation is increased.

After spatial filtering is performed using a Gaussian smoothing kernel with a fwhm of 3 voxels, the effects of aliasing in the mean magnitude images for A=2 in Fig. 3.5e and for A=3 in Fig. 3.5f appear to be diminished by the smoothing process. Upon very close observation, aliasing can still be noted within the phantom after a GRAPPA reconstruction with A=3 in Fig. 3.5f, but the effects of aliasing are still apparent above and below the phantom in space in the mean phase reconstructed images for both A=2 and A=3. As the incentive for performing spatial filtering is to decrease the noise in reconstructed images, the standard deviation within the phantom with A=1 after smoothing in Fig. 3.5d is noticeably lower than that without smoothing in Fig. 3.5a (note the change in scale). As the acceleration factor increases from A=2 in Fig. 3.5e to A=3 in Fig. 3.5f, the increase in standard deviation, is notable within the same regions as that without smoothing in Fig. 3.5b and Fig. 3.5c. With a decrease in standard deviation that results from smoothing, the SNR of the smoothed GRAPPA reconstructed images is increased. However, the same decrease in SNR with an increase in acceleration factor is notable when comparing the SNR for A=1 in Fig. 3.5d to the SNR of A=2 in Fig. 3.5e and A=3 in Fig. 3.5f.

When data is acquired with A=1, there is no interpolation performed and the operator G in Eq. [3.8] is replaced with an identity matrix. Since all four permutation matrices in Eq. [3.8] are orthonormal and both the inverse Fourier reconstruction

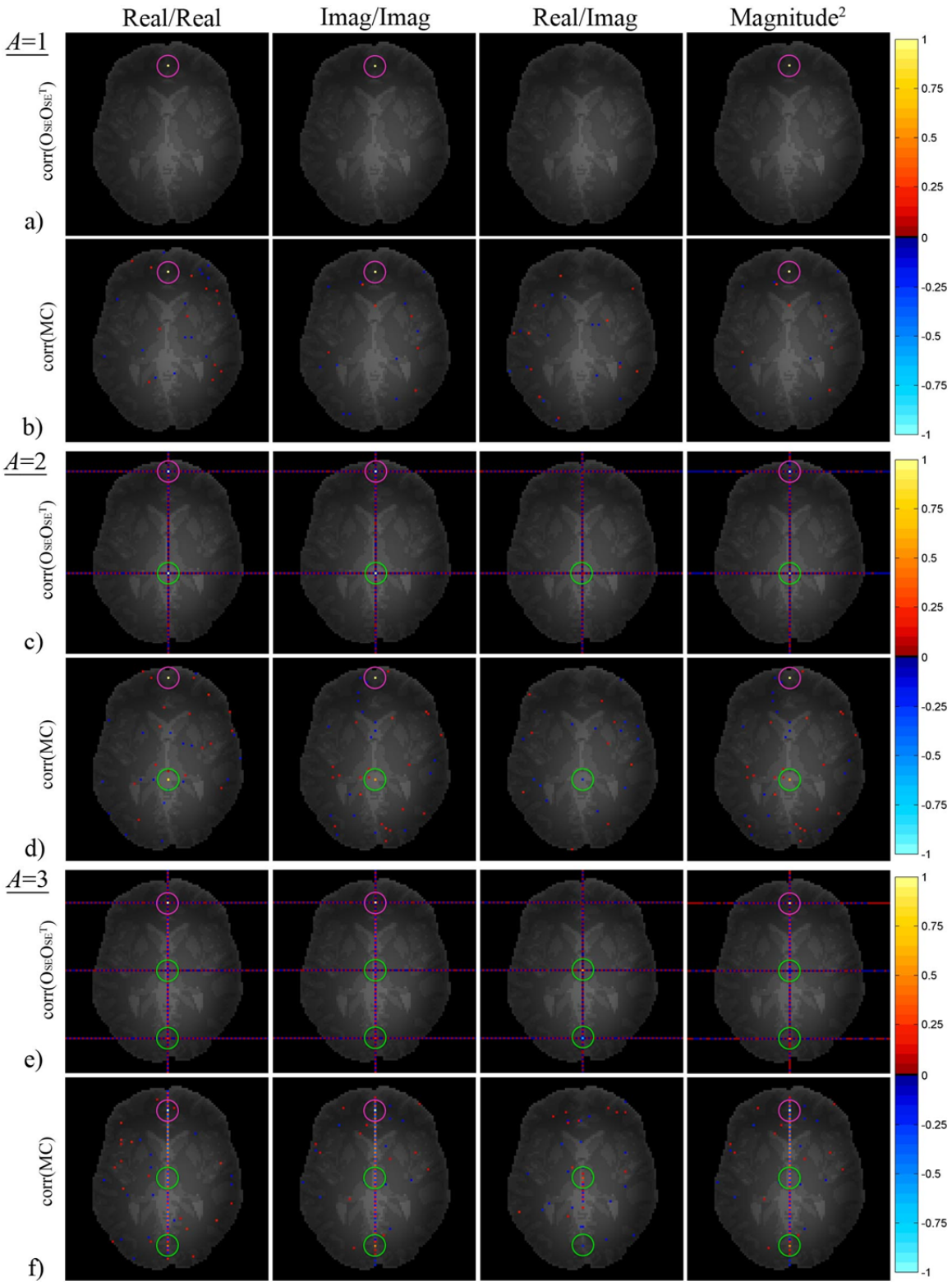

Figure 3.6: Presented on a magnitude brain phantom underlay and threshold to ±0.125 are real, imaginary, real/imaginary and magnitude-squared correlations a) theoretically induced by GRAPPA with A=1, b) estimated from MC data with A=1, c) theoretically induced by GRAPPA with A=2, d) estimated from MC data with A=2, e) theoretically induced by GRAPPA with A=3, and f) estimated from MC data with A=3.

operator, Ω, and the combination matrix, *C*, are orthogonal, the resulting correlation induced by the GRAPPA model with *A*=1 is an identity matrix. This is presented in Fig. 3.6a, with a mean magnitude reconstructed image for an underlay and a threshold of ±0.125, where there is no correlation induced by the GRAPPA model noted between the VOI in the center of the pink circle and any other voxel. To validate the lack of correlations induced by GRAPPA with *A*=1, correlations estimated from the MC time series reconstructed by GRAPPA with *A*=1 in Fig. 3.6b show no statistically significant correlation between the VOI and any other voxel that is more than a consequence of the random noise added to the generated time series of images. The theoretical correlations induced by the GRAPPA model using a 4×5 interpolation kernel with *A*=2 and *A*=3 are presented in Fig. 3.6c and Fig. 3.6e respectively. As observed in Fig. 3.4, these theoretically induced correlations show low correlations within both the rows and column of the VOI and aVOIs. These correlations exhibit a sinc pattern that is a result of the rectangular truncated interpolation kernels used in the GRAPPA interpolation process. The real, imaginary and magnitude-squared correlations for *A*=2 in Fig. 3.6c and for *A*=3 in Fig. 3.6e are greatest in value in the locations of the aVOIs and unity within the VOIs. This is due to the spatial localization performed through an interpolation process that derives interpolation weights from fully sampled data. It is of note that the correlation induced between the VOI and aVOI with *A*=2 in Fig. 3.6c are positive, while the similar correlations induced by the SENSE model in Fig. 2.11 are negative. To validate these theoretical correlations induced by GRAPPA with *A*>1, the correlations estimated from the MC time series reconstructed by GRAPPA with *A*=2 are presented in Fig. 3.6d and the MC time series reconstructed by GRAPPA with *A*=3 are presented in Fig. 3.6e. When

comparing the theoretical correlations with A=2 in Fig. 3.6c to the estimated MC correlations in Fig. 3.6d, the estimated correlations with the greatest value are found in the aVOIs in the center of the green circles, but the sinc correlation structure is no longer present. When comparing the theoretical correlations with A=3 in Fig. 3.6e to the estimated MC correlations in Fig. 3.6f, however, the estimated correlations with the greatest value are still found in the aVOIs in the center of the green circles, but the sinc correlation structure is still apparent in the column containing both the VOI and aVOIs.

When the operator O_I in Eq. [3.10] is replaced with a Gaussian smoothing operator, *Sm*, that has a fwhm of 3 voxels, and the operator O_K is replaced with an identity matrix, the correlations induced by the resulting collection of operators are presented in Fig. 3.7. The theoretical correlations induced by GRAPPA using A=1 together with smoothing are presented in Fig. 3.7a with a mean magnitude reconstructed image for an underlay and a threshold of ±0.125. Similar to a SENSE reconstruction with A=1 together with smoothing in Fig. 2.11a, the operator *Sm* is the only operator that is not orthogonal when reconstructing data with A=1, and thus there are a real, imaginary and magnitude-squared correlations induced between the VOI and its immediate neighbors. The spread of these correlations about the VOI is relative to the size of the smoothing kernel. This correlation structure is validated in Fig. 3.7b, where the only significant correlation structure between the VOI and any other voxel, estimated from the smoothed MC time series, is between the VOI and its immediate neighbors. The theoretical correlations induced by the GRAPPA model using a 4×5 interpolation kernel with A=2 and A=3 together with a smoothing operator are presented in Fig. 3.7c and Fig. 3.7e respectively. The bands of low induced correlation with a sinc structure, as noted in Fig.

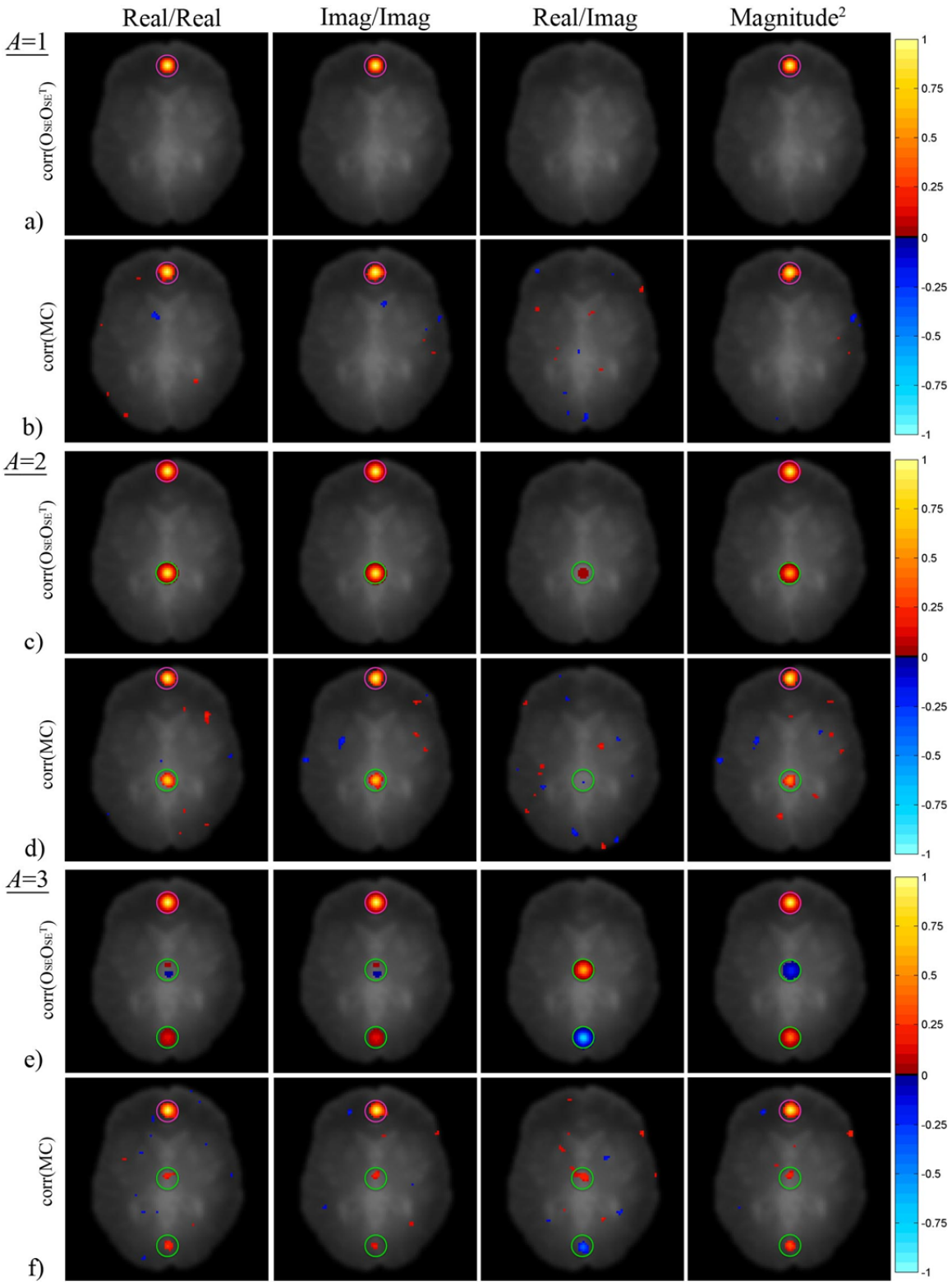

Figure 3.7: Presented on a magnitude underlay and threshold to ±0.125 are smoothed real, imaginary, real/imaginary and magnitude-squared correlations a) theoretically induced by GRAPPA with A=1, b) estimated from MC data with A=1, c) theoretically induced by GRAPPA with A=2, d) estimated from MC data with A=2, e) theoretically induced by GRAPPA with A=3, and f) estimated from MC data with A=3.

3.6c and Fig. 3.6e, are no longer apparent after smoothing is incorporated, but the correlations induced between the VOI and aVOIs are still greatest in value. Upon comparison to the unsmoothed counterparts in Fig. 3.6, all GRAPPA induced correlations with $A>1$ between the VOI and aVOIs are of the same sign and appear to be spread to the neighboring voxels of both the VOI and the neighboring voxels of the aVOIs. This implies that while the VOI may be artificially correlated with an aVOI by the GRAPPA model, the addition of smoothing induces a correlation between the VOI and neighboring voxels of the aVOIs. Unlike the combination of smoothing with a SENSE reconstruction of $A=2$ in Fig. 2.12c, the correlations induced by a GRAPPA reconstruction with $A=2$ together with smoothing are all positive. The correlations induced by GRAPPA with $A=3$ between the VOI and the aVOI in the central region of the phantom are both positive and negative while the correlations induced between the VOI and the aVOI in the posterior region of the phantom are positive. This structure is similar to that induced by the SENSE model with $A=3$. The correlations induced by the GRAPPA model with A>1 are validated by correlations estimated from the GRAPPA reconstructed MC time series with $A=2$ in Fig. 3.7d, and with $A=3$ in Fig. 3.7f. Upon comparing Figs. 3.7c and 3.7d for $A=2$ with Figs. 3.7e and 3.7f for $A=3$, the correlations induced about the VOI appear to be most apparent with the aVOIs. It is interesting to note that all correlations between the VOI and aVOIs for $A=3$ are positive, while the theoretical induced correlation between the VOI and aVOI are both positive and negative.

3.4.4 Theoretical Functional Connectivity Simulation

To replicate an fcMRI study, a Hamming band pass filter was applied to the time series of every voxel in the smoothed data sets reconstructed by GRAPPA with $A=1$, $A=2$

and A=3 to maintain temporal frequencies between 0.01 and 0.08 Hz. For this dissertation, the same 2×2 clusters of voxels as used in the SENSE illustration were selected for VOIs in the anterior of the phantom. To determine functional connectivity about the 2×2 seed region, the voxel time series were averaged over space to form a single mean time series for the VOI, v. The correlation coefficient, *cc*, between the seed region time series, v, and the time series of each other voxel, s, in the Hamming band pass filtered images for each acceleration factor were evaluated using the standard Pearson's coefficient of linear correlation in Eq. [2.18]. Through Eq. [2.18], the correlation coefficients between the real components of v and s, between the imaginary components of v and s, between the real component of v and the imaginary component of s, and between the magnitude-squared components of v and s were determined for the GRAPPA reconstructed images with A=1, A=2 and A=3.

The fcMRI correlation coefficients determined by Eq. [2.18] for the GRAPPA reconstructed time series with A=1 are presented in Fig. 3.8a with a threshold of ±0.35 (p≈0.05) (Greicius et al., 2003). As all data in this theoretical illustration was generated with an identity correlation structure, there is no apparent structure in the band pass filtered time series reconstructed by GRAPPA with A=1. The real, imaginary and magnitude-squared functional connectivity correlations about the VOI in fig 3.8a are predominantly in the local neighborhood of the VOI, with random sporadic correlations spread throughout the phantom that are a result of the added noise. For the GRAPPA reconstructed time series with A=2 in Fig. 3.8b and A=3 in Fig. 3.8c, the same structure noted in the theoretical induced correlations in Fig. 3.6 and Fig. 3.7 are noted between the

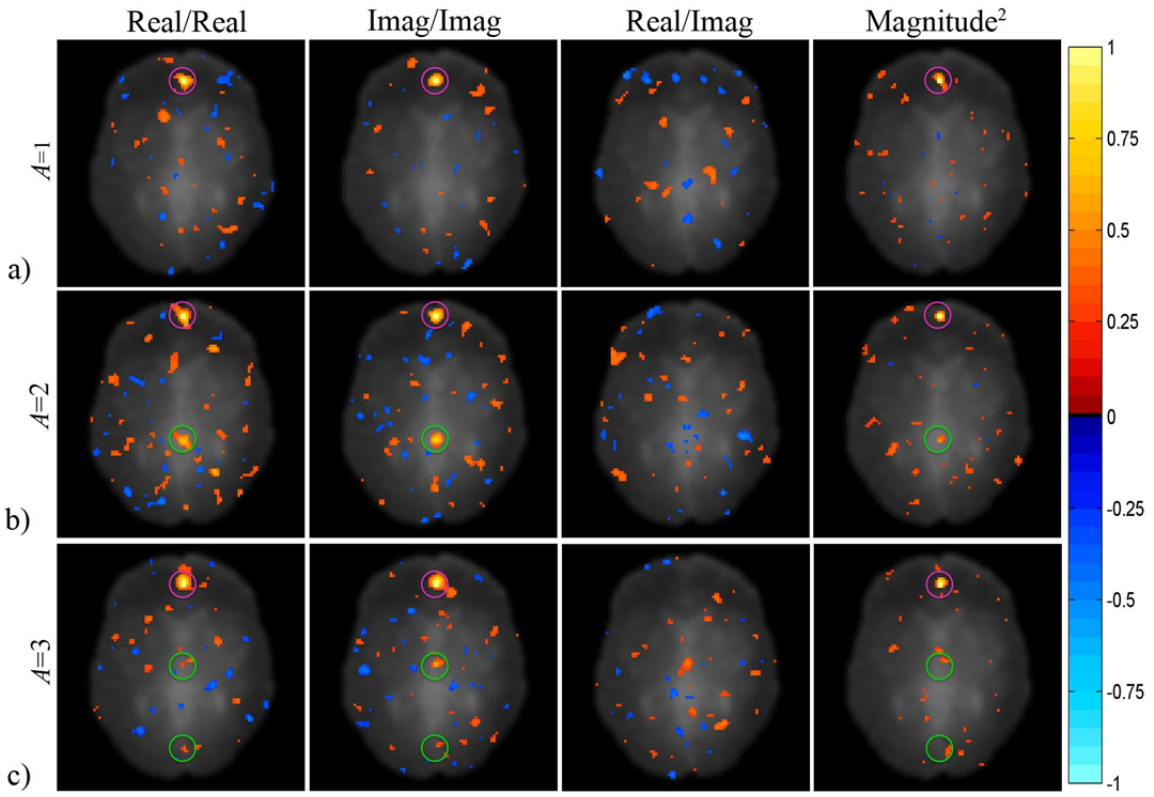

Figure 3.8: Estimated real, imaginary, real/imaginary and magnitude-squared correlations denoting functional connectivity in time series reconstructed by GRAPPA with a) A=1, b) A=2, and c) A=3 after a temporal Hamming band pass filter was applied to each voxel to maintain frequencies between 0.01 and 0.08 Hz. Correlations are all presented on a smoothed magnitude underlay and threshold to ±0.35.

VOI and aVOIs. Since the data generated in this simulation assumed an identity covariance between voxels, the correlations observed with A=2 in Fig. 3.8b and A=3 in Fig. 3.8c indicate artificial "connectivity" induced by the GRAPPA reconstruction process between brain regions.

As the correlations in Fig. 3.8 are derived from time series that have been subjected to a Hamming band pass filter to maintain temporal frequencies between 0.01 and 0.08 Hz, these correlations would reject the null hypothesis in a fcMRI study, implying that the previously aliased voxels are functionally connected. As with the SENSE illustration, the original data in this illustration was generated with an identity

covariance between voxels, and thus all correlations between the seed VOIs and any other voxel in Fig. 3.8 indicate false positives. This implies that the GRAPPA induced correlations are statistically significant and reside in the frequency spectrum commonly associated with functional connectivity. The position of the seed VOI and the aVOIs in the GRAPPA reconstructed images align themselves very closely in the commonly investigated Default Mode Network in the brain (Raichle et al., 2001; Raichle et al., 2007) in Fig. 2.2, and could therefore corrupt fcMRI conclusions. Depending on the sign of the induced correlations and the sign of the correlations inherent in the acquired data, these non-biological artificially induced correlations could lead to potential Type I & II errors.

3.5 Experimental Illustration of GRAPPA Induced Correlations

3.5.1 Data Acquisition and Reconstruction

To validate the statistical implications of the GRAPPA model that were explored in the previous section, the same non-task human subject fcMRI data set that was used for the experimental illustration of the SENSE model in the previous chapter was reconstructed with the GRAPPA model. This data set included 510 TRs that were acquired with each of N_C=8 receiver coils through an EPI pulse sequence in a 3.0T General Electric Signa LX magnetic resonance imager. The imaged region of the brain was acquired in four axial slices with 96×96 voxels that were 2.0×2.0×2.5mm in dimension. Each TR in the time series was 1 s in length with an echo time of 45.4 ms, an effective echo spacing of 816 μs, excited by a flip angle of 45°, and an acquisition bandwidth of 125 kHz. The first 20 of the 510 TRs were discarded to account for T_1

effects and varying echo times, resulting in 490 TRs acquired under the same conditions. A Nyquist ghost correction was performed by acquiring the center row of *k*-space for each TR in each receiver coil with three navigator echoes from which the error in the center frequency and group delay offsets between the odd and even lines of *k*-space were estimated and adjusted accordingly (Nencka et al., 2008). To account for dynamic fluctuations in the homogeneities of the main B-field that arise from factors such as respiration and out of field motion, the global temporal phase structure was corrected in each coil to account for field shifts associated with gradient heating and RF phase variations that EPI acquisition techniques are susceptible to (Hahn et al., 2009; Hahn et al., 2012). Additionally, to account for the drift in B-field gradients, a plane was fit to and subtracted from the phase in each image in a time series in each coil using the technique outlined in (Jesmanowicz et al., 2011).

To observe the difference between the same set of data being fully sampled with A=1 to being sub-sampled by A=3 and reconstructed by the GRAPPA model, sub-sampling was performed retrospectively by deleting rows of *k*-space with the PE direction oriented as anterior-posterior. The weights used in a two-dimensional 4×5 GRAPPA interpolation in Eq. [3.2] were determined for the interpolation with A=3 by inserting the fully sampled data set with A=1 into Eq. [3.5]. Once the interpolation weights were determined, the missing lines of *k*-space in the sub-sampled data set were interpolated from the acquired lines using Eq. [3.2]. With N_C=8 fully sampled arrays of *k*-space for the data set acquired with A=1, and N_C refilled arrays of *k*-space for the data sets sub-sampled by A=3, a combined *k*-space array for each data set was formed with a complex valued average performed over the coil dimension. The combined array of

spatial frequencies in each of the 490 TRs for both A=1 and A=3 were then inverse Fourier reconstructed into time series of full FOV combined images. After reconstruction, each image in both data sets were spatially filtered using a Gaussian smoothing kernel with a fwhm of 3 voxels. To observe functional connectivity, a Hamming band pass filter was then applied to the time series of every voxel in the smoothed GRAPPA reconstructed images with A=1 and A=3 to maintain temporal frequencies between 0.01 and 0.08 Hz.

3.5.2 Experimental Results

The mean magnitude, mean phase, standard deviation and SNR for the data sets reconstructed by GRAPPA with A=1 and A=3 and smoothed with a Gaussian kernel are presented in Fig. 3.9a and Fig. 3.9b respectively. With the size of the brain being small relative to the FOV, there are not noticeable signs of aliasing in the mean magnitude images as were observed in Fig. 3.5. When the same data set with A=3 was reconstructed with the SENSE model in Fig. 2.14, there were noticeable differences between the mean phase within the brain by comparison to the data set with A=1. This was likely due to the un-aliasing of voxels using coil sensitivities estimates of inhomogeneous B-fields. Such distinctions are not apparent when comparing the mean phase images for data sets with A=1 and A=3 reconstructed with the GRAPPA model in Fig. 3.9. Although the sub-sampled images are folded over on themselves A=3 times through the aliasing process, the relatively small size of the brain compared to the FOV means that the brain itself only experiences two-fold aliasing, with one of the A=3 aliased voxels falling in space. As noted in the theoretical illustration in Fig. 3.5, the reduced dimensions of k-space in the data set sub-sampled by A=3 results in a standard deviation in Fig. 3.9b that is greater in

the areas of two-fold aliasing than that of the data set with A=1 in Fig. 3.9a. Given that SNR is derived by the ratio of the mean magnitude and standard deviation in each voxel, the increase in standard deviation with an increase in A results in a decrease in the SNR for images reconstructed from data with A=3 in Fig. 3.9b by comparison to images reconstructed from data with A=1 in Fig. 3.9a.

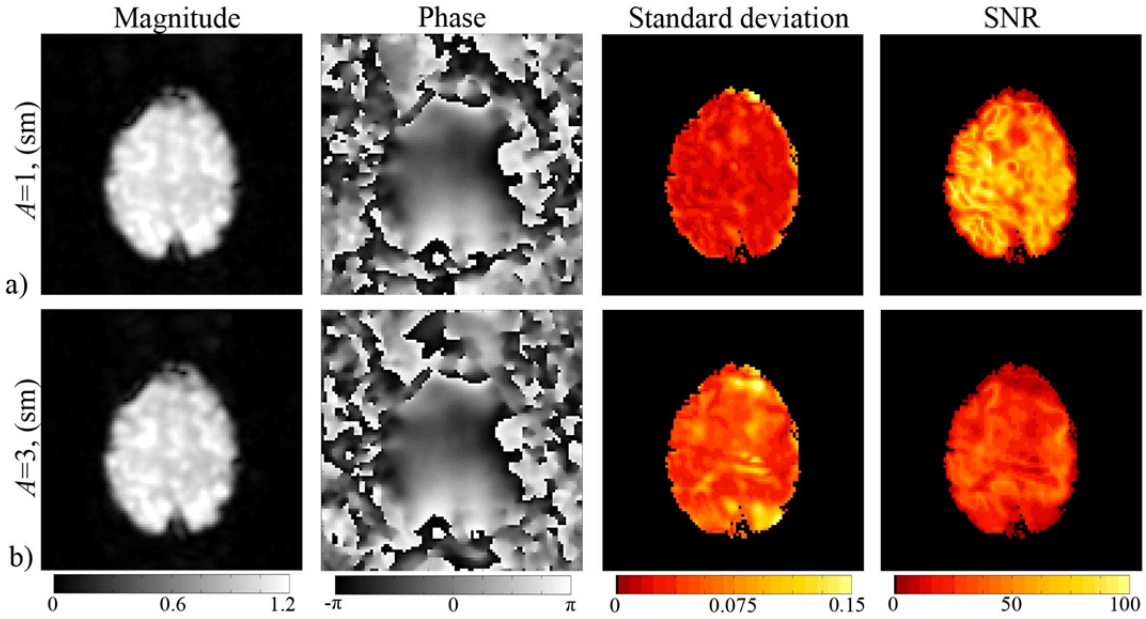

Figure 3.9: Mean magnitude and phase, standard deviation and SNR for images of a human subject reconstructed by the GRAPPA model with a) A=1 and b) A=3 together with smoothing.

As with the SENSE model, the comparison between the real, imaginary, real/imaginary and magnitude-squared correlations induced by an application of the GRAPPA model with A=1 versus A=3 is performed in three ways. First, the theoretical correlations induced by the GRAPPA reconstruction operators, O_G, together with a smoothing operator, Sm, in Eq. [3.10] were determined through Eq. [3.14] and are presented in Fig. 3.10a for A=1, and Fig. 3.10d for A=3. When data is acquired with A=1,

there is no interpolation performed and thus the operator G in Eq. [3.10] is replaced with an identity matrix. Second, the correlations estimated directly from the experimentally acquired data sets (EXP) reconstructed with the GRAPPA model together with smoothing are presented in Fig. 3.10b for A=1 and in Fig. 3.10e for A=3. Finally, the correlations estimated about a 2×2 seed region, determined with Eq. [2.18], in the reconstructed time series after a Hamming band pass filter was applied to each voxel's time series are presented in Fig. 3.10c for A=1 and in Fig. 3.10f for A=3. The images in Fig. 3.10a and Fig. 3.10d illustrate the theoretical structure of the correlations induced by the GRAPPA model, even if there is a correlation induced between the VOI and voxels in space, while all correlation in Figs. 3.10b-c and Figs. 3.10e-f are masked to observe correlations between the VOI and other voxels within the brain only. All correlations in Fig. 3.10 are presented on top of a magnitude underlay with a pink circle highlighting each VOI and green circles highlighting the aVOI's. The theoretical correlations induced by GRAPPA are presented with a threshold of ±0.125 to display the general structure of the correlations induced by the GRAPPA model, while the EXP correlations estimated from the reconstructed images with and without band pass filtering are presented with a threshold of ±0.35 (p≈0.05) (Greicius et al., 2003).

As the theoretical correlations presented in Fig. 3.10a are for a GRAPPA reconstruction with A=1 together with smoothing, the only correlation structure of note is that induced between the VOI and its immediate neighbors by the Gaussian smoothing kernel. As noted with the SENSE model in Fig. 2.15, the estimated EXP correlations for data reconstructed with A=1 together with smoothing in Fig. 3.10b show positive real, imaginary and real/imaginary correlations in the vicinity of the VOI with negative real,

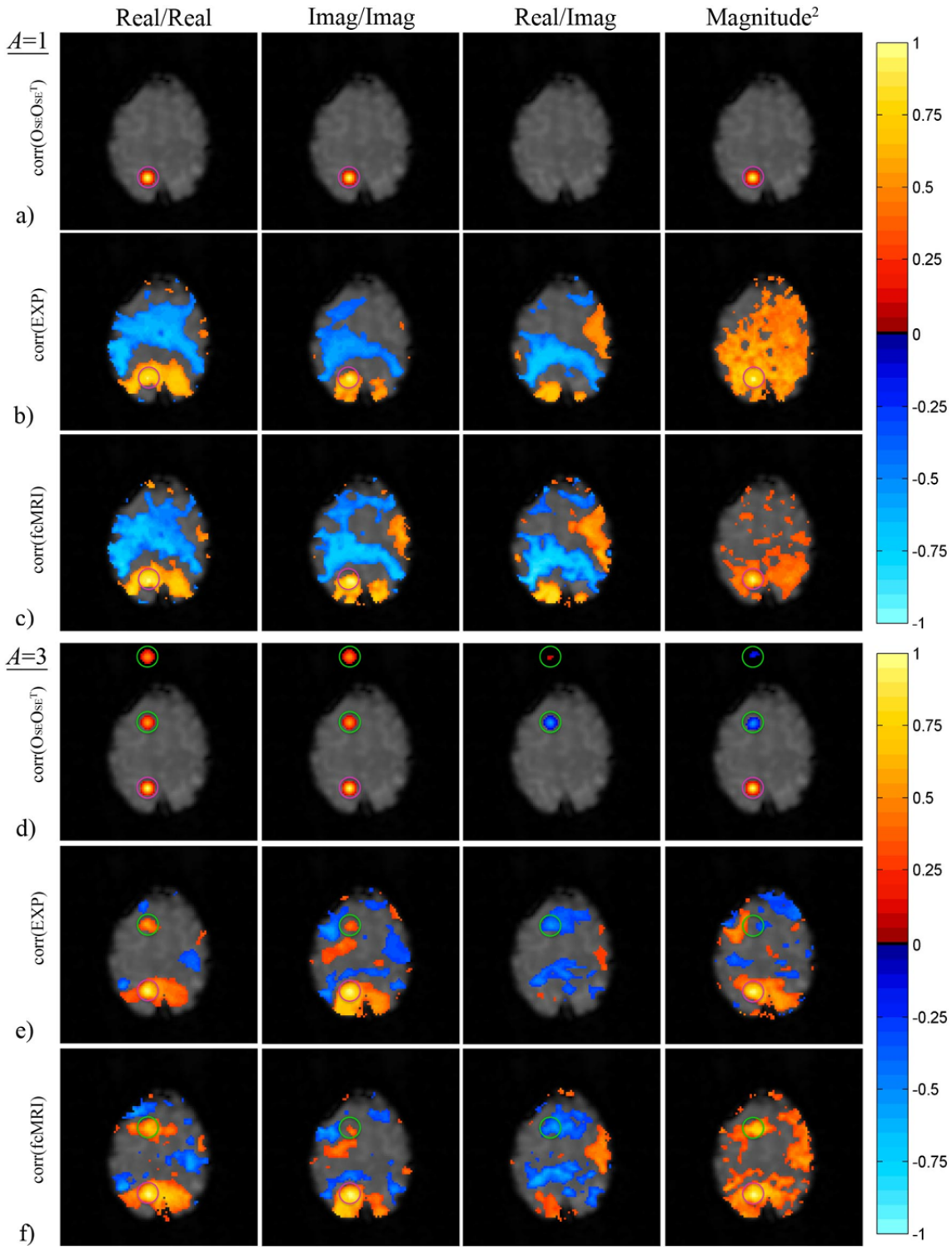

Figure 3.10: Correlations about a VOI for a human subject data set a) theoretically induced by GRAPPA with A=1, b) estimated EXP correlations with A=1, c) fcMRI correlations estimated from Hamming band pass filtered images reconstructed by GRAPPA with A=1, d) theoretically induced by GRAPPA with A=3, e) estimated EXP correlations with A=3 and f) fcMRI correlations estimated from Hamming band pass filtered images reconstructed by GRAPPA with A=3. Correlations in a) and d) are threshold to ±0.125 and correlations in b-c) and e-f) are threshold to ±0.35.

imaginary and real/imaginary correlations across the midbrain region. As the correlations estimated from magnitude-squared data all appear to be positive and are strongest in the vicinity of the VOI, the negative real, imaginary and real/imaginary correlations are most estimated from magnitude-squared data all appear to be positive and are strongest in the vicinity of the VOI, the negative real, imaginary and real/imaginary correlations are most likely a byproduct of B-field inhomogeneities that are manifested in the phase of the reconstructed images. When the time series of each voxel in the smoothed images reconstructed by GRAPPA with A=1 are band pass filtered to the frequency spectrum commonly associated with fcMRI, the correlations representing functional connectivity in Fig. 3.10c still resemble the structure of their un-filtered counterparts in Fig. 3.10b. It is of note that the negative structures in the real, imaginary and real/imaginary fcMRI correlations in Fig. 3.10b appear to be amplified after band pass filtering the GRAPPA reconstructed time series with A=1 in Fig. 3.10c, while the magnitude-squared fcMRI correlations are diminished to the anterior region of the brain. When band pass filtering was performed for the SENSE model, all fcMRI correlation structures appeared to be diminished by comparison to the corresponding estimated EXP correlations. This suggests that the B-field inhomogeneities that manifest themselves in the phase of the images combined in k-space through the GRAPPA model with A=1 reside within the low frequency spectrum associated with functional connectivity.

With the VOI located in the anterior region of the brain, the aVOIs prior to an application of the GRAPPA model with A=3 fall both within the anterior of the brain and in space above the brain. The correlations induced by an application of the GRAPPA model with A=3 between the VOI and the real, imaginary, real/imaginary and magnitude-

squared components of all other voxels are presented in Fig. 3.10d. As with the theoretical illustration, the real and imaginary induced correlations are all positive while the correlations induced between real and imaginary components of the VOI and aVOIs are both positive and negative. Unlike the theoretical illustration, the theoretical correlations induced between the VOI and aVOIs in magnitude-squared data in Fig. 3.10d are all negative. There are notable differences when comparing the estimated EXP correlations for data reconstructed with A=3 together with smoothing in Fig. 3.10e to the corresponding EXP correlations estimated from data with reconstructed with A=1 in Fig. 3.10b. The strong negative correlations noted with A=1 in Fig. 3.10b are not as apparent with a GRAPPA reconstruction with A=3 in Fig. 3.10e, but there is rather a cluster of voxels within the region of the aVOI that exhibit positive real and imaginary correlation structures and negative real/imaginary and magnitude-squared correlation structures. As the shape and sign of the voxels within the aVOI correlated to the VOI match their respective theoretical induced structure in Fig. 3.10d, and more importantly are not present with A=1 in Fig. 3.10b, they are most likely a result of the GRAPPA reconstruction process. When the time series of each voxel in the smoothed time series reconstructed by GRAPPA with A=3 is band pass filtered to the frequency spectrum commonly associated with fcMRI, the correlations representing connectivity in Fig. 3.10f still show positive real and imaginary correlations between the VOI and the aVOI and negative correlations between the real and imaginary components of the VOI and aVOI. Interestingly, the VOI and aVOI in the band pass filtered magnitude-squared data set reconstructed with A=3 exhibit a strong positive correlation structure when the correlations without band pass filtering in Fig. 3.10e do not exhibit this positive structure.

As the fcMRI correlations in Fig. 3.10c for a data set with no sub-sampling (A=1) show no positive correlations between the VOI and the location of where aVOI would be in the anterior of the brain, these regions would not be assumed to be functionally connected in the data set reconstructed with A=1. Should a neuroscientist not account for the implications of the reconstruction and processing operations performed on their data, the notable correlations between the VOI and aVOI after a GRAPPA reconstruction with A=3 in Fig. 3.10f (which are of no biological origin) would reject the null hypothesis in a functional connectivity study, suggesting that these two regions are in fact functionally connected when they are not.

3.6 Discussion

The GRAPPA model is one of the most common pMRI models used in most clinical SIEMENS MRI scanners. By exploiting a uniform spacing between discrete spatial frequency measurements, the GRAPPA model offers an attractive means of estimating the sub-sampled spatial frequencies in each coil through an interpolation kernel that incorporates acquired measurements both within a coil and between coils. As with the SENSE model, many studies (including those funded by the $35m Human Connectome Project) utilize the GRAPPA model to reconstruct accelerated acquisitions of k-space with little to no regard as to the degree to which the model changes the statistical properties of the data.

The real-valued isomorphic framework outlined in this chapter provides a novel means of precisely quantifying the structure of the correlations artificially induced by the GRAPPA model without the need for time-consuming MCMC simulations that can only estimate the induced correlation structure. To validate the correlations theoretically

induced by the GRAPPA model, however, both theoretical MC and experimental illustrations were performed in this dissertation. As the GRAPPA interpolation induces a local correlation between spatial frequencies, this correlation becomes global after an inverse Fourier reconstruction. Since the GRAPPA model uses a truncated convolution kernel derived from the Fourier transform of fully sampled coil sensitivities, the correlations induced between voxels of the reconstructed images are greatest in strength between previously aliased voxels, as noted with the SENSE model. Unlike the SENSE model, the rectangular interpolation kernel used in the GRAPPA model has also been shown to induce low correlations within the rows and column of both the VOI and aVOIs that exhibit a sinc structure, making it more difficult to precisely isolate the voxels that are artificially correlated by the GRAPPA model than by the SENSE model.

As the correlations induced by the GRAPPA model still exceed a threshold of ±0.35 after the reconstructed voxel time series in both theoretical and experimentally acquired data are Hamming band pass filtered to frequencies of 0.01 and 0.08 Hz, failure to account for these correlations would result in regions of the brain mistakenly assumed to be functionally connected, with 95% confidence, when they are not. As with the SENSE model, when sub-sampling is performed from anterior/posterior, these correlations can fall within the commonly explored default mode network, while sub-sampling from left/right could result in these correlations falling within the motor cortices. As such, there is ultimately a need for new methods to accelerate data without inducing such misleading correlations. In the meantime, it is necessary for scientists conducting an fcMRI study that employs models such as GRAPPA to at least quantify

and be aware of the presence of these correlations between regions they may be investigating.

Chapter 4: Informed RF Coil Design for Region Specific fcMRI Studies

4.1 RF Coil Design Theory

While the artificial correlations induced by pMRI models such as SENSE and GRAPPA, as discussed in the previous two chapters, are a byproduct of reconstructing accelerated acquisitions of *k*-space, a far more commonly explored consequence of this process is the loss in SNR. As described in Eq. [1.6], the inverse Fourier transformation of a $p_y \times p_x$ array of independent spatial frequency measurements from *k*-space to image space scales the covariance of the *k*-space measurements by a factor of $1/p_y p_x$. Thus, when the array of independent spatial frequencies is reduced to a dimension of $(p_y/A) \times p_x$, the scaling factor of the covariance is increased from $1/p_y p_x$ to $A/p_y p_x$. With the SNR in a voxel evaluated as the ratio of the voxel's mean and its standard deviation, the resulting SNR of a SENSE (or GRAPPA) reconstructed image is therefore reduced by a factor of $\sqrt{A}$. Given that this increase in the standard deviation is unavoidable, many studies focus primarily on the additional reduction in SNR that results from the amplification of noise in SENSE reconstructed images caused by the overlap of coil B-fields.

If a phased array is comprised of adjacent rectangular coils, such as the conventional "birdcage" array illustrated in Fig. 4.1a with N_C=8 coils, the B-field of each coil has an effective depth of sensitivity that is roughly equivalent to the outer dimensions of the coil. As the red rectangular coil in Fig. 4.1a has a narrower width than height, the depth of sensitivity, illustrated in Fig. 4.1b, is approximately that of the width of the coil. When the B-field contribution for each of the N_C coils in Fig. 4.1a are combined, the SNR distribution in SENSE reconstructed images is typically lower in both the central

and peripheral regions of the reconstructed images, as these regions are far away from the center of each coil (Chen et al., 2007). By this notion, the physical geometry of a phased array affects the profiles of coil B-fields and in turn the SNR in SENSE reconstructed images, SNR_{SE}. The optimization of RF coil arrays designed for SENSE imaging has therefore been an area of study for several years.

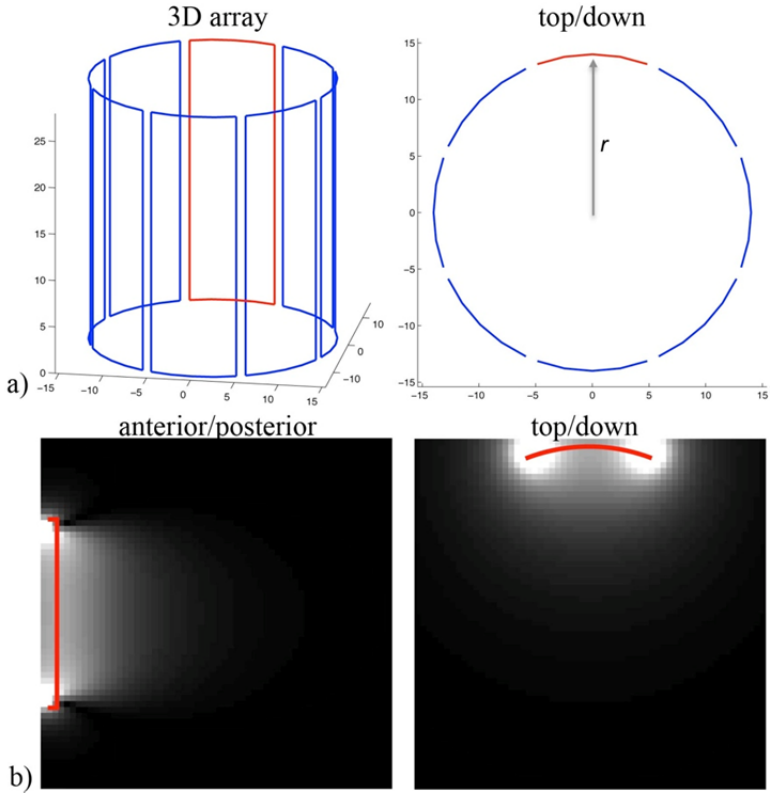

Figure 4.1: a) A "birdcage" array of N_C=8 rectangular coils with b) magnetic fields generated by the first coil (red) as viewed from anterior to posterior through the center (y,z) plane and top/down through the center (x,y) plane.

4.1.1 Estimation of RF Coil Magnetic Fields

Consider the closed wire loop resembling an RF coil in Fig. 4.2a. If a current, I, flows around the loop, a magnetic field, B, is generated by the current. Due to the counter

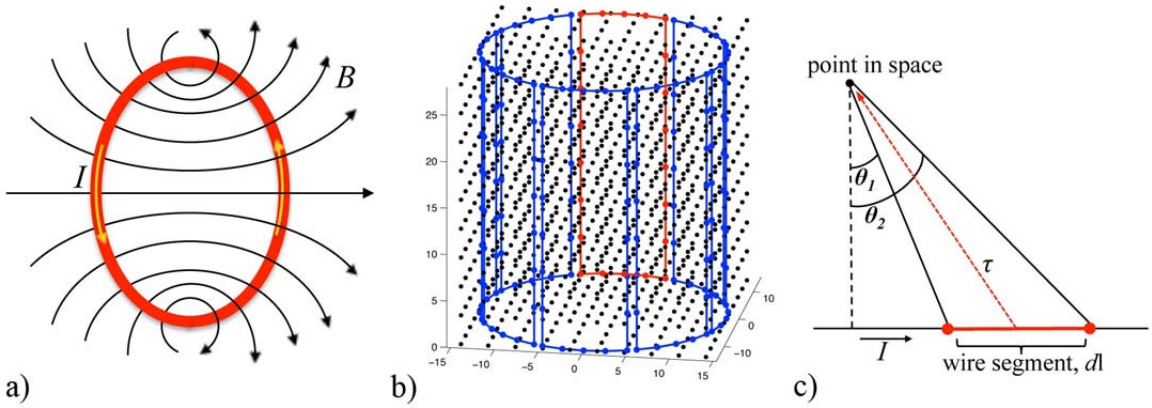

Figure 4.2: Using a) a current flowing through a loop of wire in a counter clockwise direction, b) the B-field generated by each coil can be is estimated by representing the coil as a collection of N_V connected vertices, and c) using Biot-Savart to sum to contribution of each segment at every point in space.

clockwise direction of flow, the B-field generated by the current is projected "out of the page". Based on this principle, if each coil in Fig. 4.2b is treated as a closed loop of wire with a current flowing in the counter clockwise direction, then the B-field of each coil will project into the center of the array. To estimate the B-field generated by the array, each coil element in Fig. 4.2b is represented as a collection of N_V connected vertices, with the space surrounding the array represented as a 3-dimensional lattice. With the array represented in this fashion, the B-field generated by a single coil at each point in space can be approximated by the Biot-Savart law (Griffiths, 1999) through a sum of the B-field generated by each wire segment, dl, that make up the coil,

$$
\begin{aligned}
B &= \frac{\mu_0}{4\pi}\int \frac{Id\mathbf{l}\times\hat{\tau}}{|\tau|^2} \\
&= I\frac{\mu_0}{4\pi}\int_{\theta_1}^{\theta_2}\cos\theta\, d\theta \\
&= I\frac{\mu_0}{4\pi}\left(\sin\theta_2 - \sin\theta_1\right).
\end{aligned}
\qquad [4.1]
$$

In Eq. [4.1], μ_0=4π×10^{-7} NA^{-2} is the permeability of free space, τ is the displacement

vector from the wire segment, dl, to the point in space, $\hat{\tau}$ is the unit vector of τ, θ_1 and θ_2 are the angles between the point in space and the two ends of the wire segment, as illustrated in Fig. 4.2c.

4.1.2 The Notion of Coil Symmetry

Using a cylindrical coordinate system with a fixed coil radius, r, each vertex that defines the geometry of the coil in Fig. 4.2b has a specific location defined by coordinates (ϕ,z). If the geometry of each of the N_C coils in the array is defined by N_V connected vertices, the total number of parameters to be optimized is $2N_CN_V$. As the number of vertices defining a complete array of coils increases linearly with the number of coils in the array, constraints are placed on the resolution that can be employed in defining the coil deformations due to an increased computational load. To decrease both computational time and demand, it has become conventional to assume that RF coil arrays exhibit symmetry both within a coil and between coils. As illustrated in Fig. 4.3a, an individual coil can be fully symmetric, assume a mirrored symmetry from left to right, assume symmetry from the top down, or exhibit no symmetry at all. Similarly, all coils in the array, illustrated in Fig. 4.3b, can assume a full radial symmetry, have a mirrored symmetry about a single plane (such as the sagittal plane), or exhibit no symmetry at all. The birdcage array in Fig. 4.1a is an example of an array that assumes both full symmetry within each coil and a full radial symmetry between coils. Assuming such a fully symmetric array allows for the optimization to be simplified and performed on a single coil, with at most $2N_V$ parameters. For each iteration of an optimization algorithm, the coordinates of the N_V vertices in one coil are shifted to new locations, producing a unique B-field for the new geometry of the coil. The B-fields of the remaining N_C-1 coils are

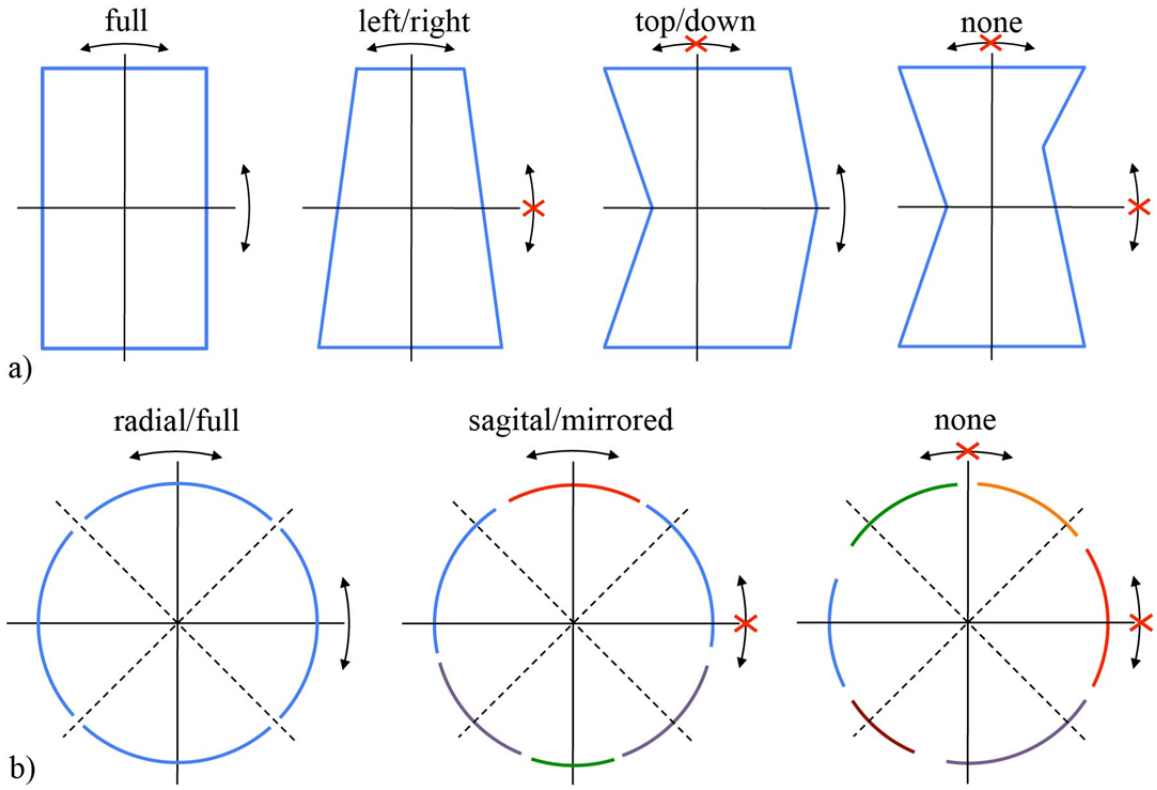

Figure 4.3: The types of symmetry that can be assumed a) within an individual coil and b) between all coils (when viewed from the top).

then simulated as a rotation of the B-field generated by the first coil around a cylinder. With such constraints on coil symmetry, the variables defining an RF coil array become the coil radius, the length of the coils, the number of coils, and the shape of the coils (rectangular, oval, butterfly, etc.).

When there is no symmetry assumed between coils, as shown in Fig. 4.3b, the total number of parameters to be optimized would be $2N_CN_V$, and the B-field for all N_C coils would need to be estimated in each iteration of an optimization algorithm. For the assumption of sagittal symmetry, the left and right halves of the array exhibit a mirrored symmetry, and thus the total number of parameters to be optimized would reduce to N_CN_V. However, because the current flows through each coil in a counter clockwise

direction, as illustrated in Fig. 4.2a, the B-fields for the coils on the right half of the array would not simply be a rotation of those on the left half. As such, the B-field for all N_C coils would still need to be estimated in each iteration of an optimization algorithm.

4.1.3 A New Perspective on RF Coil Design

Unlike birdcage RF coil arrays, the human brain is not fully symmetric, and ROIs are rarely in the very center of the brain. As such, almost all constraints on coil symmetry are relaxed in this dissertation, thereby allowing for each coil element in a phased array to be individually optimized for a given ROI. However, as it is becoming common for pMRI studies to use arrays with an increasingly larger number of coils, that are each defined by a greater number of vertices, the number of parameters to be optimized can become excessive when each coil has to be individually optimized. This dissertation therefore introduces a novel approach of using spatial normalization (Friston et al., 1995; Ashburner et al., 1999) to morph an array of coils into an optimal configuration with sine and cosine basis functions. In this approach, the number of parameters is limited to twice the number of basis functions, irrespective of the number of coils and vertices. Albeit the number of coils and vertices will affect the computation time for each iteration in the optimization algorithm, but the number of parameters to be optimized is dramatically decreased.

Almost all coil optimization studies use a cost function that minimizes the overall *g*-factor in SENSE reconstructed images, thereby maximizing SNR_{SE}. However, since the SENSE model utilizes coil B-field sensitivities for spatial localization, both the un-aliasing process and the correlations that were shown to be induced by that process in Chapter 2 (Bruce et al., 2011; Bruce et al., 2012; Bruce et al., 2013) are by definition

functions of coil geometry (Bruce et al., 2013; Bruce et al., 2014). As such, this dissertation also introduces a revised cost function to be used in the parameter estimation that, when minimized, produces an array of coils that has both an improved SNR_{SE} and a minimal influence of SENSE induced correlations in functional connectivity studies that analyze the SENSE reconstructed images.

4.2 A New Cost Function for Informed RF Coil Design

If the values for a single complex-valued aliased voxel, j, in each of N_C aliased coil images are placed in a vector, a_{jC}, the complex-valued weighted least squares estimation of the un-aliased voxel values, v_{jC}, by the SENSE model in Eq. [2.2] can be rewritten as

$$\begin{aligned} v_{jC} &= \left(S_{jC}{}^{H}\Psi^{-1}S_{jC}\right)^{-1} S_{jC}{}^{H}\Psi^{-1}a_{jC} \\ &= U_{jC}a_{jC}. \end{aligned} \qquad [4.2]$$

If the aliased voxel, j, is in the k^{th} row of the aliased coil images, with the PE direction oriented as anterior/posterior (sub-sampling from the bottom of the image to the top), then the A un-aliased voxel values in v_{jC} will be located in rows [k, $k+p_y/A$, $k+2p_y/A$, … $k+(A-1)p_y/A$]. When solving Eq. [1.11] for the geometry factor, g_j,

$$g_j = \frac{\mathrm{SNR}_{full,j}}{\mathrm{SNR}_{SE,j}\sqrt{A}} = \sqrt{\left(S_{jC}{}^{H}\Psi^{-1}S_{jC}\right)_{j,j}^{-1}\left(S_{jC}{}^{H}\Psi^{-1}S_{jC}\right)_{j,j}} \geq 1, \qquad [4.3]$$

the result is a vector of length A with a g-factor value for each of the A un-aliased voxels in Eq. [4.2]. The g-factor effectively measures the condition of the unfolding matrix, U_j, in Eq. [4.2] and provides a real-valued measurements of the noise amplification that results from an overlap of coil B-fields in each of the A un-aliased voxels in v_{Cj}. Theoretically, the maximal value of SNR_{SE} is unbounded, and $1/SNR_{SE}$ could approach

zero when an optimal coil geometry is achieved. The *g*-factor, however, is always unity in voxels that were not previously aliased, irrespective of the SNR in that voxel, and is a value that is no less than one when in a voxel that was previously aliased. This places a convenient lower bound in the optimization, and since a minimization of the *g*-factor simultaneously maximizes SNR_{SE}, it has become the de-facto metric for optimizing RF coil designs for SENSE imaging.

While the *g*-factor may be a real-valued measure of the noise amplification in images reconstructed by the SENSE model, the model itself is applied to complex-valued aliased voxel measurements. In most fcMRI studies, the SENSE reconstructed images are converted to magnitude-only images for analysis, but recent studies have shown that important biological information can be derived from the phase portion of a complex-valued time series (Rowe and Logan, 2004; Rowe and Logan, 2005; Rowe, 2005; Nencka et al., 2009; Menon et al., 2012), and thus the implications of the SENSE unfolding on both the real and imaginary components of the un-aliased voxels is necessary. Equivalent to the technique used in Chapter 2, the SENSE unfolding process in Eq. [4.2] can be represented in a real-valued form by stacking the real components of the complex-valued vectors $a_{jC}=a_{Rj}+ia_{Ij}$ and $v_{jC}=v_{Rj}+iv_{Ij}$ on top of the corresponding imaginary components, and representing the unfolding matrix, $U_{jC}=U_{Rj}+iU_{Ij}$, in a skew-symmetric form by

$$\begin{bmatrix} v_{jR} \\ v_{jI} \end{bmatrix} = \begin{bmatrix} U_{jR} & -U_{jI} \\ U_{jI} & U_{jR} \end{bmatrix} \begin{bmatrix} a_{jR} \\ a_{jI} \end{bmatrix},$$

or

$v_j=U_j\, a_j$.

Assuming the voxels in the vector a_j have an ideal identity covariance structure, the artificial covariance that is induced solely by the SENSE unfolding process between the voxels in v_j is

$$\Sigma_j = \mathrm{cov}(v_j) = U_j U_j^T. \quad [4.4]$$

The covariance matrix in Eq. [4.4] can be converted to a real-valued correlation matrix representing the induced correlation between the real and imaginary parts of the complex-valued reconstructed voxels by

$$\mathrm{corr}(U_j U_j^{\ T}) = D^{-1/2} U_j U_j^{\ T} D^{-1/2} = \begin{bmatrix} corr_{j,RR} & corr_{j,RI} \\ corr_{j,IR} & corr_{j,II} \end{bmatrix}, \quad [4.5]$$

where D is a diagonal matrix with elements drawn from the diagonal of $U_j U_j^T$. The four quadrants of the correlation matrix in Eq. [4.5] denote the correlations induced between the real components of v_{jC}, between the imaginary components of v_{jC}, and between the real and imaginary components of v_{jC}. It is of note that the artificially induced correlations in Eq. [4.5] are of no biological origin and have been shown in Chapter 2 to influence conclusions drawn in functional connectivity studies by making regions of the brain that were previously aliased with one another appear to be either correlated or uncorrelated when they are not (Bruce and Rowe, 2013; Bruce and Rowe, 2014). Since the unfolding matrix, U_j, is derived from coil B-field sensitivities, S_{jC}, and a covariance between coils, Ψ_C, it is therefore entirely dependent on coil-geometry. If the SENSE model is to be used for accelerating the acquisition of fcMRI data sets, then there is a natural need for coils to be optimized using a metric that not only minimizes the conventional *g*-factor in Eq. [4.3], but minimizes the theoretical SENSE induced correlations in Eq. [4.5] as well.

In a conventional RF coil design study, the *g*-factor is determined in each voxel within an ROI, and the geometry that exhibits an overall *g*-factor that is closest to one is deemed optimal for the given ROI. If the SENSE model induced no covariance between voxels, the $2A\times 2A$ correlation structure in Eq. [4.5] would be an identity matrix. A generalized likelihood ratio statistic for the degree to which voxels are uncorrelated can therefore be used as a metric for determining the overall correlation induced by SENSE about all voxels in an ROI (Rowe, 2003). To perform such a test, the $2A\times 2A$ covariance matrix for every voxel $j=[1,\ldots p]$ within an ROI, Σ_j, is first placed along the diagonal of a large block diagonal covariance matrix

$$\Sigma = \begin{bmatrix} \Sigma_1 & & 0 \\ & \ddots & \\ 0 & & \Sigma_p \end{bmatrix}. \qquad [4.6]$$

In a test for the degree to which voxels within the ROI are correlated with their previously aliased counterparts, the null-hypothesis assumes that the SENSE induced covariance in Eq. [4.6] is a strictly diagonal matrix, H_0: $\Sigma = diag(\Sigma)$, with off-diagonal terms $\Sigma_{jk}=0$, while the alternative hypothesis H_1: $\Sigma \neq diag(\Sigma)$ assumes that a covariance has been induced between previously aliased voxels j and k, $\Sigma_{jk}\neq 0$. Failure to reject H_0 would indicate that the voxels un-aliased by SENSE in Eq. [4.2] are independent, while a rejection of H_0 would denote a statistically significant covariance (or correlation) has been induced. If a matrix, Y, is comprised of the p aliased voxels within the ROI, X is a $p\times 2$ design matrix, and the maximum likelihood estimates of the coefficients, β, and the covariance, Σ, under the null and alternative hypotheses are

$$\tilde{\beta}^T = (X'X)^T X^T Y \quad \text{and} \quad \tilde{\Sigma} = \frac{1}{p} diag\left[(Y - X\tilde{\beta}^T)^T (Y - X\tilde{\beta}^T)\right]$$
$$\hat{\beta}^T = (X'X)^T X^T Y \qquad\qquad \hat{\Sigma} = \frac{1}{p}(Y - X\hat{\beta}^T)^T (Y - X\hat{\beta}^T),$$

then the generalized likelihood ratio statistic for dependence between voxels is

$$\begin{aligned}\lambda &= \frac{P(Y \mid \tilde{\beta}, \tilde{\Sigma}, X)}{P(Y \mid \hat{\beta}, \hat{\Sigma}, X)} \\ &= \frac{(2\pi)^{-\frac{p}{2}} \left|\tilde{\Sigma}\right|^{-\frac{p}{2}} e^{-\frac{1}{2} tr\tilde{\Sigma}^{-1} diag(Y - X\tilde{\beta})(Y - X\tilde{\beta})^T}}{(2\pi)^{-\frac{p}{2}} \left|\hat{\Sigma}\right|^{-\frac{p}{2}} e^{-\frac{1}{2} tr\hat{\Sigma}^{-1}(Y - X\hat{\beta})(Y - X\hat{\beta})^T}} \\ &= \left[\frac{\left|\tilde{\Sigma}\right|}{\left|\hat{\Sigma}\right|}\right]^{-\frac{p}{2}}.\end{aligned} \qquad [4.7]$$

The ratio in Eq. [4.7] of the strictly diagonal covariance matrix assumed in H_0, $\tilde{\Sigma}$, and the covariance matrix with SENSE induced off-diagonal elements in H_1, $\hat{\Sigma}$, simplifies to a matrix, R, with the overall correlation structure induced between voxels. After converting to a log-likelihood ratio for dependence, the statistic in Eq. [4.7] is further simplified to

$$\begin{aligned}\ln(\lambda) &= \ln\left[\frac{\left|\tilde{\Sigma}\right|}{\left|\hat{\Sigma}\right|}\right]^{-\frac{p}{2}} \\ &= \ln\left[\left|R\right|^{-\frac{p}{2}}\right] \\ &= -\frac{p}{2}\ln\left|R\right|.\end{aligned} \qquad [4.8]$$

If the $2A \times 2A$ correlation matrix for every voxel j=[1,…p] in the ROI, R_j = corr($U_j U_j^T$), are theoretically derived through Eq. [4.5] and placed along the diagonal of a larger block diagonal correlation matrix,

$$R = \begin{bmatrix} \text{corr}(U_1 U_1^T) & & 0 \\ & \ddots & \\ 0 & & \text{corr}(U_p U_p^T) \end{bmatrix} = \begin{bmatrix} R_1 & & 0 \\ & \ddots & \\ 0 & & R_p \end{bmatrix},$$

then based on the properties that the determinant of a block diagonal matrix is the product of the determinants of each block, and that the logarithm of a product is the sum of the logarithms, Eq. [4.8] simplifies to a scalar by

$$\begin{aligned} -\frac{p}{2}\ln\left|R\right| &= -\frac{p}{2}\ln\left[\prod_{j=1}^{p}\left|R_j\right|\right] \\ &= -\frac{p}{2}\sum_{j=1}^{p}\ln\left|R_j\right|. \end{aligned} \qquad [4.9]$$

If R_j is an identity matrix, then the determinant of the correlation induced about voxel v_j is one, and thus the contribution from that voxel, j, to the statistic in Eq. [4.9] is zero after taking the logarithm. By contrast, any increase in the strength of the correlations induced by SENSE will be exponentially weighted through the logarithm within the sum in Eq. [4.9], which is more appropriate than a simple linear combination of induced correlations since correlation strength increases quadratically.

For a cost function that appropriately combines both the traditional geometry factor and the SENSE induced correlations, the cost function of the *g*-factor is first defined by subtracting 1 from the average *g*-factor over the p voxels in the ROI,

$$H_g = \frac{1}{p}\sum_{j=1}^{p} g_j - 1.$$

Given the lower bound of the *g*-factor being one, H_g approaches zero when a unit *g*-factor is achieved. For a metric of the overall SENSE induced correlation in an ROI to be on the same order as H_g, the likelihood ratio statistic in Eq. [4.9] is scaled by $1/p^2$, defining the cost function for the correlations induced about all voxels in an ROI by the SENSE model as

$$H_{\mathrm{corr}_{SE}} = -\frac{1}{2p}\sum_{j=1}^{p}\ln\left|R_j\right|.$$

Like H_g, the cost function $H_{corr_{SE}}$ approaches zero when no correlation is induced by the SENSE model. As both cost functions H_g and $H_{corr_{SE}}$ approach zero when optimized, a joint cost function can be expressed as

$$H = w_g H_g + w_{corr_{SE}} H_{corr_{SE}}, \quad [4.10]$$

where w_g and $w_{corr_{SE}}$ are the weights for the *g*-factor and SENSE induced correlation cost functions respectively. These weights can be derived through a calibration study for each choice of N_C, A, and the size/location of the ROI. Such a calibration is described in the Methods section of the theoretical simulation to follow.

As the SENSE reconstruction process is not an orthogonal operation, the statistical properties of SENSE reconstructed images are altered by the un-aliasing process both within a voxel and between voxels. The *g*-factor provides a measure of the degree to which the overlap of coil B-field sensitivities amplifies the noise (increases the standard deviation) within each voxel of the reconstructed images. The minimization of H_g in Eq. [4.10] would therefore allow for an improved SNR_{SE} to be achieved in each voxel by diminishing the effects of the SENSE reconstruction process on the standard deviation of each individual voxel's time series. By contrast, a minimization of $H_{corr_{SE}}$ in Eq. [4.10] reduces the artificially induced correlation (or covariance) between voxels. When a collection of A voxels become highly correlated as a result of the SENSE un-aliasing process, it becomes increasingly difficult to deduce meaningful information from the time series of all A voxels. If, for example, the A voxels un-aliased by the SENSE model became perfectly correlated as a result of the process, then there would only be one time series worth of meaningful information for all of the A voxels together. As such, the lower the SENSE induced correlations, as achieved by minimizing $H_{corr_{SE}}$, the more

meaningful functional connectivity information can be obtained from the A un-aliased voxels given the same number of sub-sampled measurements.

4.2 Adapting Spatial Normalization to Morph an RF Coil Array

In many fMRI and fcMRI studies, data is collected for groups of subjects to find common trends in cognitive brain activity. Issues faced by these studies include the fact that each patient in the group could have a brain that is a different size and positioned differently in the scanner from one patient to the next. To achieve spatial normalization of the brain images for the entire group, statistical parametric mapping (SPM) uses cosine basis functions to fit the brain scans for each patient to a template image (Friston et al., 1993; Friston et al., 1995; Ashburner et al., 1999). This is done by first defining the shape and size of a template image of the brain, and then systematically morphing the acquired images for each subject in the grouped data until the spatial locations of the brain regions of all subjects are in the same location. An iterative Gauss-Newton nonlinear least squares estimation process is typically performed in which the residual squared difference between images from each subject and the template is minimized.

While there is no "template image" to morph an RF coil array onto, the basic concept of spatial normalization can be applied to optimizing RF coil arrays by treating the ideal g-factor and SENSE induced correlations within an ROI as a template. Ideally, there would be a unit g-factor in every voxel within the ROI, with an identity correlation structure induced by the SENSE reconstruction process, thereby achieving H=0 in Eq. [4.10]. To morph a cylindrical array of rectangular RF coils into an optimal arrangement using spatial normalization, the array of N_C=8 coils in Fig. 4.4a is "unrolled" onto a 2-

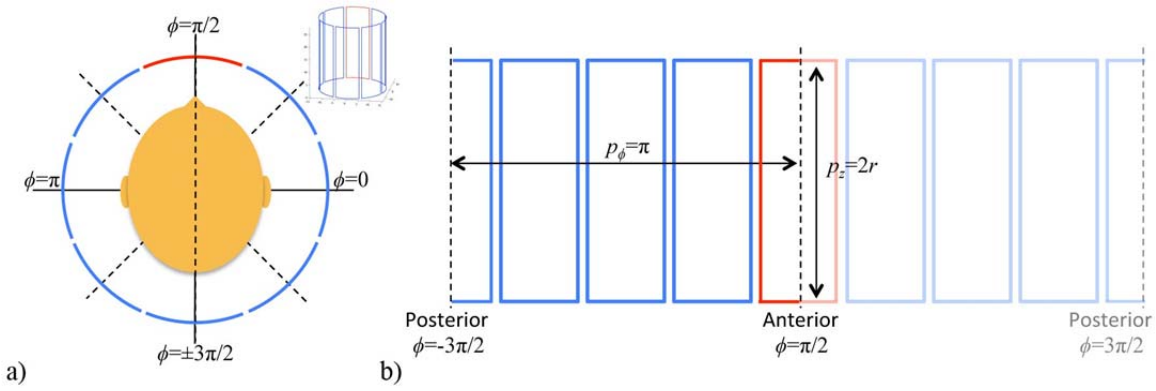

Figure 4.4: An array of N_C=8 rectangular coils arranged in a) 3-dimensional cylindrical coordinates and b) "unrolled" onto a 2-dimensional Cartesian plane, (ϕ,z).

dimensional plane in Fig. 4.4b with the horizontal dimension corresponding to the angle of displacement from the center of the first coil, ϕ, and the vertical dimension corresponding to the height of the coil, z. If the loop of each coil is defined by edges joined at a collection of vertices, each with coordinate locations (ϕ,z), then these vertices can be shifted into new locations through the spatial normalization process, checking the "fit" of the array with the ideal template conditions through Eq. [4.10].

At each (ϕ,z) location, spatial transformations are performed both vertically and horizontally through a linear combination of smooth cosine and sine basis functions. The choice of cosine and/or sine basis functions depends on the required behavior of the transformations at the boundaries. If points at the boundaries over which the transformation is performed are not allowed to shift, then a collection of sine basis functions should be used in the transformation. By contrast, if there are no such constraints placed on the boundaries, then a collection of cosine basis functions would be more appropriate. If there are no constraints on the symmetry of an RF coil array, then Fourier basis functions would be the most appropriate choice for transformations in the ϕ-dimension as it would invoke a wrap around condition at the boundaries.

As illustrated in Fig. 4.4a, the brain exhibits approximate bilateral/sagittal symmetry, making it reasonable to reduce the computational load by placing a symmetry constraint about the sagittal plane, as illustrated in Fig. 4.3b, where the left half of the array is a mirror image of the right half. This can be done by centering the anterior coil at the top of the array, $\phi=\pi/2$, as shown in Fig. 4.4b, and centering the posterior coil at the bottom of the array, $\phi=\pm 3\pi/2$. The horizontal period of the half-array in Fig. 4.4b is thus $p_\phi=\pi$, while the period of the z-dimension is defined as twice the coil radius, $p_z=2r$, which is the length of the coil. This effectively reduces the image to be morphed to the left half of Fig. 4.4b. With the array defined in this manner, deformations in the ϕ-dimension need to be constrained at the $\phi=-3\pi/2$ and $\phi=\pi/2$ boundaries, while there are no constraints on deformations in the z-dimension at any boundary. To constrain deformations in the ϕ-dimension, a collection of sine basis functions with a period of $p_\phi=\pi$ can be used such that the deformations are zero at the $\phi=-3\pi/2$ and $\phi=\pi/2$ boundaries. In addition to the boundary constraints in the ϕ-dimension, the basis functions have to also exhibit both symmetry and asymmetry about $\phi=0$. If the basis functions are all symmetric about $\phi=0$ then the deformed array will always exhibit a mirrored symmetry about the coronal plane as well as the sagittal plane. By contrast, if all basis functions are asymmetric about $\phi=\pi$, then the array can never exhibit coronal symmetry. Since the goal of this study is for the shape of the array to be defined by the size and location of the ROI, the optimization algorithm needs to be able to morph an array of rectangular coils into any shape, irrespective of whether or not the final array is symmetric or asymmetric about the coronal plane. As there are no constraints on the deformations in the z-dimension, the deformations can be defined using a collection of cosine basis functions. For a collection

of J_ϕ bases in the ϕ-dimension and J_z bases in the z-dimension, the 2-dimensional deformation fields are therefore defined with a combination of sine and cosine basis functions by

$$\begin{aligned} Q_\phi(\phi,z,j_\phi,j_z) &= \sqrt{\frac{2}{p_\phi}}\sqrt{\frac{2}{p_z}}q(\phi)\sin\left[\frac{\pi j_\phi \phi}{p_\phi}\right]\cos\left[\frac{\pi(j_z-1)z}{p_z}\right] \\ Q_z(\phi,z,j_\phi,j_z) &= \sqrt{\frac{2}{p_\phi}}\sqrt{\frac{2}{p_z}}\cos\left[\frac{\pi(j_\phi-1)\phi}{p_\phi}\right]\cos\left[\frac{\pi(j_z-1)z}{p_z}\right]. \end{aligned} \quad [4.11]$$

The windowing function, $q(\phi)$, in Eq. [4.11] is defined by

$$q(\phi)=\begin{cases} \sin\left[\frac{\varphi}{2}(\phi-\delta)\right], & \frac{-3\pi}{2}<\phi\le\frac{-3\pi}{2}+\frac{p_\phi}{\varphi} \\ 1, & \frac{-3\pi}{2}+\frac{p_\phi}{\varphi}<\phi<\frac{\pi}{2}-\frac{p_\phi}{\varphi} \\ -\sin\left[\frac{\varphi}{2}(\phi-\delta)\right], & \frac{\pi}{2}-\frac{p_\phi}{\varphi}\le\phi<\frac{\pi}{2} \\ 0, & \text{otherwise} \end{cases}, \quad [4.12]$$

and is designed to constrain the function Q_ϕ to zero when ϕ=-3π/2 and ϕ=π/2. In Eq. [4.12], the horizontal shift,

$$\delta=\frac{4p_\phi}{\varphi}\left[ceil(\frac{3\varphi}{8})-\frac{3\varphi}{8}\right],$$

centers both of the sine functions in $q(\phi)$ such that $q(\phi)$ tapers from zero at ϕ=-3π/2 and ϕ=π/2 to one at ϕ=-3π/2+p_ϕ/φ and ϕ=π/2-p_ϕ/φ, where φ is an even integer.

If T_ϕ and T_z are $J_z \times J_\phi$ coefficient matrices for deformations in the ϕ and z dimensions respectively, then the coordinates for each vertex, (ϕ,z), are morphed to a new set of vertex coordinates (ϕ_{new},z_{new}) by

$$\begin{aligned} \phi_{new} &= \phi-\sum_{j_z=1}^{J_z}\sum_{j_\phi}^{J_\phi}T_\phi(j_z,j_\phi)\cdot Q_\phi(\phi,z,j_\phi,j_z) \\ z_{new} &= z-\sum_{j_z=1}^{J_z}\sum_{j_\phi}^{J_\phi}T_z(j_z,j_\phi)\cdot Q_z(\phi,z,j_\phi,j_z). \end{aligned} \quad [4.13]$$

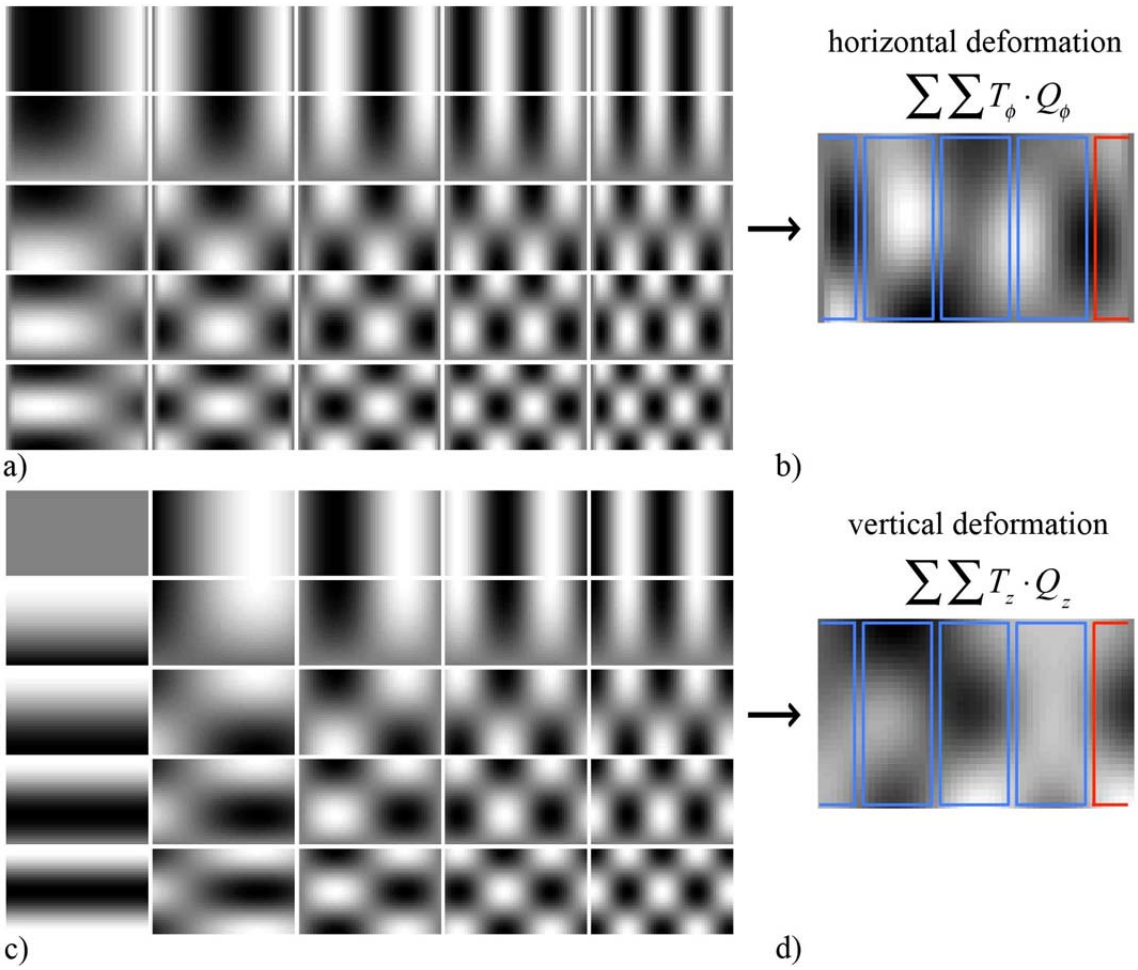

Figure 4.5: a) J_ϕ=5 and J_z=5 two-dimensional basis functions, Q_ϕ, b) weighted by coefficients stored in a matrix, T_ϕ, to achieve an overall combined horizontal deformation field applied to the vertices of a coil array, and c) two-dimensional basis functions, Q_z, d) weighted by coefficients stored in a matrix, T_z, to achieve an overall combined vertical deformation field applied to the vertices of a coil array. For horizontal deformations in a) and b), black deformations signify a shift to the left and white deformations signify a shift to the right. For vertical deformations in c) and d), black deformations signify a downward shift and white deformations signify an upward shift.

For a collection J_ϕ=5 and J_z=5 basis functions, the 2-dimensional deformations for the ϕ-dimension, Q_ϕ, are illustrated in Fig. 4.5a, which when combined using coefficients, T_ϕ, results in an overall deformation field for the ϕ-dimension in Fig. 4.5b. In both Fig. 4.5a and Fig. 4.5b, the black deformations signify shifts to the left while white deformations signify shifts to the right. Illustrated in Fig. 4.5c are the 2-dimensional deformations for the z-dimension, Q_z, which when combined using coefficients, T_z, results in an overall

deformation field for the z-dimension in Fig. 4.5d. Similarly in both Fig. 4.5c and Fig. 4.5d, the black deformations signify downward shifts while white deformations signify upward shifts.

As the $J_z \times J_\phi$ basis functions Q_ϕ and Q_z in Eq. [4.11] remain constant, the coefficient matrices, T_ϕ and T_z, are the parameters to be estimated in the optimization of an RF coil array through spatial normalization. In the morphing of brain images with SPM, an iterative application of Eq. [4.11] is performed in a Gauss-Newton algorithm to determine the least squared residuals between the updated and template images, and is thus performed in the same domain as the images themselves. For RF coil optimization, however, the parameters T_ϕ and T_z update the vertex coordinates of each coil in an array, B-fields are then approximated for each coil in the array using a technique such as Biot-Savart, and finally the cost function in Eq. [4.10] is evaluated to assess the geometry of that vertex shift. While the domain in which the parameters are applied differs by several nonlinear transformations to the domain in which the cost function is evaluated, the basic principle of SPM is upheld as the goal is to morph the array until the spatial normalization with a template image is achieved, as determined by H=0 in Eq. [4.10].

4.3 Theoretical Simulation

4.3.1 Methods

Setup

To simulate the optimization of an RF coil's geometry for specific brain regions, a conventional "birdcage" array of N_C=8 rectangular coils, illustrated in Fig. 4.6a, was used as an initial array to be morphed. The cylindrical array was given a radius of r=14 cm,

with each coil in the array being 28 cm ($2r$) in length, and the first coil (in red) was centered at $\phi=\pi/2$ in the anterior of the array. The physical geometry of each individual coil was described by a collection of $N_V=22$ connected vertices, each with a (ϕ,z) location. With $N_C=8$ coils, this implies a total of $2N_CN_V=352$ vertex coordinates to be optimized. As the 3-dimensional brain phantom in the center of the array in Fig. 4.6a exhibits approximate bilateral symmetry, the RF coil arrays in this dissertation are assumed to be symmetric about the sagittal plane. If conventional RF coil design studies (Chen et al., 2007) were to only assume sagittal symmetry, the vertices of each coil would be individually shifted and the number of coordinates that would need to be optimized would be $N_CN_V=176$. To improve upon this large number of parameters, the morphing of RF coil arrays into geometries optimized for specific brain regions is performed using spatial normalization in this dissertation with a collection of $J_\phi=5$ and $J_z=5$ two-dimensional basis functions used for the horizontal and vertical displacements. The coefficient matrices in Eq. [4.13], T_ϕ and T_z, are therefore both 5×5 in dimension, which leaves a total of 50 parameters to be optimized.

Regions of Interest

The overarching goal of this study is to develop RF coils that are optimized for specific regions of the brain that are not necessarily in the very center. To most effectively illustrate the ability to morph an RF coil array into an optimal arrangement using both spatial normalization and the cost function in Eq. [4.10], two ROIs were selected that are commonly investigated in both fMRI and fcMRI studies. The first ROI is the Default Mode Network (DMN) in Fig. 2.2b, which has become a very popular network of apparent functional connectivity observed when a patient is at rest (Raichle et

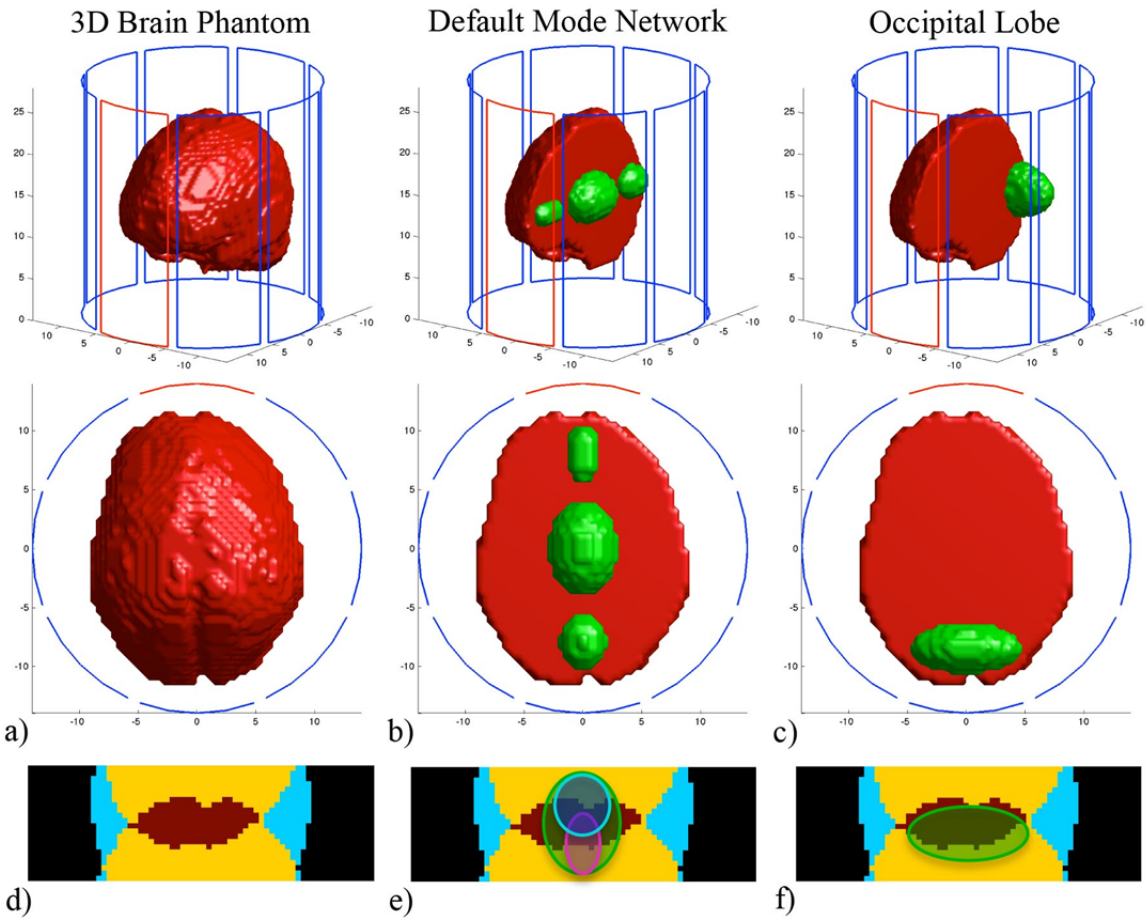

Figure 4.6: a) 3-dimensional brain phantom placed in a birdcage array of N_C=8 rectangular coils with ROIs representing b) the Default Mode Network, and c) the occipital lobe. d) The aliasing pattern through the center axial plane of the 3-dimensional brain phantom with an acceleration of A=3, with aliasing patterns of e) the Default Mode Network ROI and the f) occipital lobe ROI.

al., 2001; Raichle et al., 2007). Many fMRI and fcMRI studies on this network of brain regions have linked a lack of apparent connectivity between these regions with signs of Alzheimer's disease and autism, while signs of over activity in these regions have been linked with schizophrenia (Castelli et al., 2002; Just et al., 2004; Just et al., 2007; Buckner et al., 2008; Broyd et al., 2009; Assaf et al., 2010; Spencer et al., 2012; Lynch et al., 2013). Since the DMN spans a collection of regions along the center of the brain, the ROI for this study is defined by the three ellipsoids in Fig. 4.6b. These ellipsoids were selected to vary in shape and size along the center of the brain, and are slightly above the

center axial plane. The second ROI selected for this study is the occipital lobe (OCCIP) in the anterior region of the brain. Part of the visual cortex, various fMRI studies have associated functional activity within the occipital lobe with both epilepsy and seizures (Loiseau et al., 1991; Manford et al., 1992; Berg et al., 1999; Jallon et al., 2001; Taylor et al., 2003). The OCCIP ROI for this study is defined by the single ellipsoid in the posterior of the brain phantom in Fig. 4.6c. While both the DMN and OCCIP are in relatively well-defined regions of an individual's brain, not all subjects will have brains that are the same shape and size. As such, the ellipsoids that define the DMN and the OCCIP in Fig. 4.6 were chosen to encompass the general area of each ROI.

Sub-Sampling Scheme and Orientation

For this study, the PE direction was defined as anterior/posterior and sub-sampling was simulated with an acceleration factor of A=3. When the 3-dimensional brain phantom in Fig. 4.6a is sub-sampled by A=3, the aliasing pattern through the center axial plane is illustrated in Fig. 4.6d. In Fig. 4.6d, the blue region represents voxels with no aliasing, the yellow region represents voxels with a two-fold aliasing, and the red region represents voxels with a three-fold aliasing. This sampling scheme was selected because of the position of the ROIs. The three ellipsoids that form the DMN ROI span across the center of the brain from anterior to posterior and will therefore become aliased with one another when sub-sampling is performed, as illustrated in Fig. 4.6e. When un-aliased with SENSE, there will be an artificially induced correlation between regions that could be mistaken for functional connections within the DMN ROI when they are not. When sub-sampled by A=3, the OCCIP ROI will become aliased with the mid-brain region and the frontal lobe, as illustrated in Fig. 4.6f. Due to this aliasing pattern, any

activity within the OCCIP ROI could corrupt functional activation and connectivity maps in the mid-brain and frontal lobe, and likewise any functional activity in the aforementioned regions could corrupt functional activation and connectivity maps in the OCCIP ROI.

Magnetic Field Estimation

Throughout both the calibration of the cost function and the iterative optimization algorithm used in this study, every minor variation in the coefficient matrices, T_ϕ and T_z, in Eq. [4.13] results in a new set of coil vertex coordinates, and thus an entirely new coil geometry. As such, B-fields have to be estimated for every array that is generated. To estimate the B-fields for each coil, the cylindrical coordinates of the vertices that define each coil in the array, (ϕ,z), are first converted to Cartesian coordinates by $x=r\cos(\phi)$ and $y=r\sin(\phi)$. The 3-dimensional Cartesian array is then positioned in a 42×42×42 lattice with (x,y,z) coordinates ranging from $-r$ to r, such as that in Fig. 4.2b. With a unit current flowing through a single coil in a counter clockwise direction, the B-field generated by that coil at every point in the lattice is estimated by the Biot-Savart integration in Eq. [4.1]. Once the B-fields for all N_C=8 coils are determined, the *g*-factor and SENSE induced correlation cost functions in Eq. [4.10] are evaluated within the ROI's.

4.3.2 Calibration of the Cost Function

The two ROIs selected for this study are different in both size and shape, and will therefore be aliased with different regions of the brain after sub-sampling is performed. The SENSE un-aliasing process will therefore result in different *g*-factor and SENSE induced correlation values within each ROI. It is for this reason that the weights, H_g and

$H_{corr_{SE}}$, in Eq. [4.10] need to be calibrated for each ROI separately. To determine these weights, 10,000 random coil arrays were generated using J_ϕ=5 and J_z=5 2-dimensional basis functions with 5×5 coefficient arrays that were uniformly distributed,

$$T_{\phi/z} \sim U\left(-\frac{1}{J_{\phi/z}}, \frac{1}{J_{\phi/z}}\right). \qquad [4.14]$$

For each of the 10,000 trials, the randomly generated coefficients in Eq. [4.14] were used to shift the vertices of the rectangular array in Fig. 4.6a using Eq. [4.13], after which B-fields for each coil were estimated and finally the cost functions H_g and $H_{corr_{SE}}$ for both

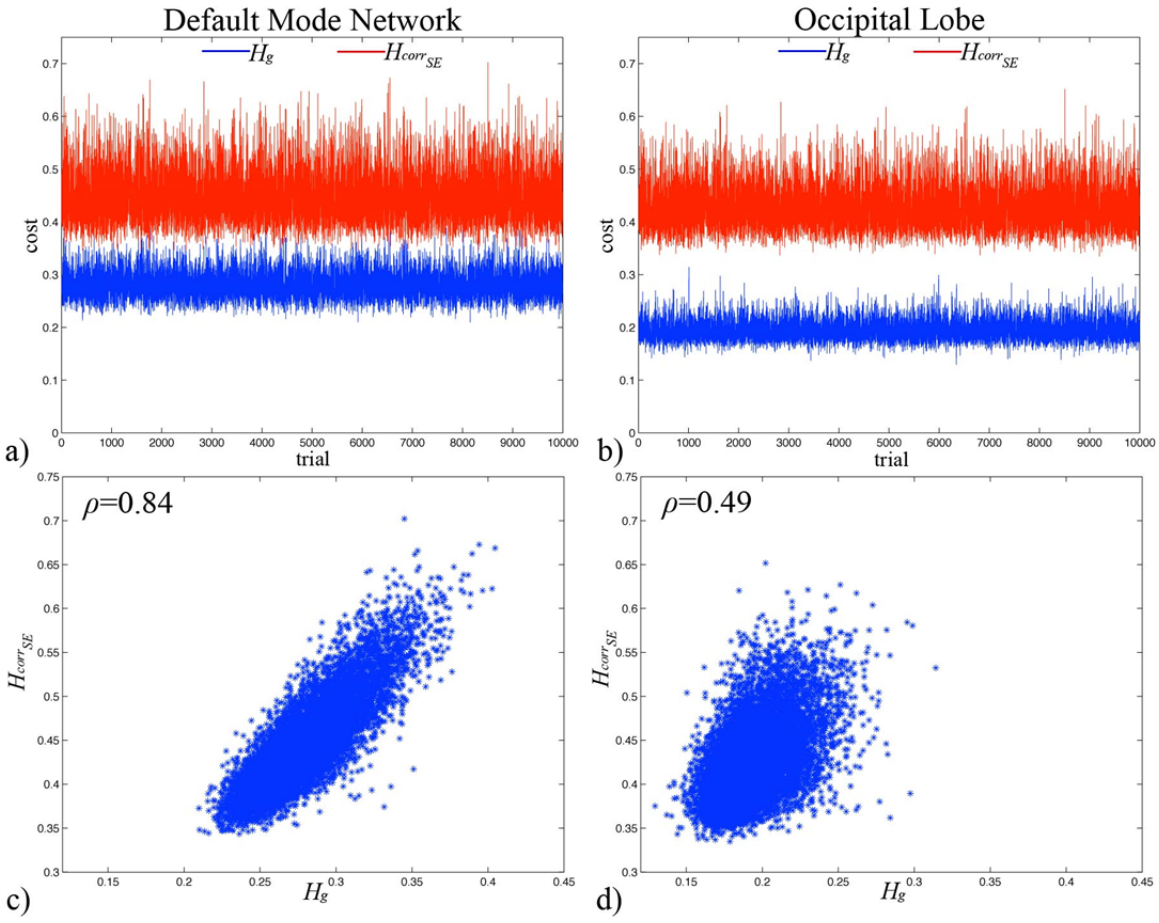

Figure 4.7: Variations in the cost functions H_g (blue) and H_{corrSE} (red) in each of 10,000 calibration trials for a) the DMN ROI and b) the OCCIP ROI, with scatter diagrams showing the relatively high linear correlation between the two cost functions, ρ, of c) the DMN ROI and d) the OCCIP ROI.

the DMN and OCCIP ROIs were evaluated. Plots of the two cost functions for the two ROIs over each of the 10,000 arrays are presented in Fig. 4.7. Upon observation in Fig. 4.7, it is apparent that arrays for each ROI that exhibit an increase in either H_g or $H_{corr_{SE}}$ are not always marked by a similar increase in the other function, but there is an apparent correlation between the two cost functions, ρ=corr(H_g, $H_{corr_{SE}}$), for both the DMN and for the OCCIP ROIs, as presented in Table 4.1. For this particular selection of N_C, A, $J_{\phi/z}$ and the locations of the two ROIs, $H_{corr_{SE}}$ is always greater in value and has a greater variability than H_g, and thus one would choose weights $w_g > w_{corr_{SE}}$ such that minor variations in $H_{corr_{SE}}$ do not overshadow significant variations in H_g. Using the methodology proposed by Bates and Granger (1969) for combining forecasting models, weights that account for the difference in variability between the two cost functions can be derived by

$$w_g = \frac{\sigma^2_{\mathrm{corr}_{SE}} - \sigma_{g,\mathrm{corr}_{SE}}}{\sigma^2_g + \sigma^2_{\mathrm{corr}_{SE}} - 2\rho\sigma_g\sigma_{\mathrm{corr}_{SE}}} \quad \text{and} \quad w_{\mathrm{corr}_{SE}} = \frac{\sigma^2_g - \sigma_{g,\mathrm{corr}_{SE}}}{\sigma^2_g + \sigma^2_{\mathrm{corr}_{SE}} - 2\rho\sigma_g\sigma_{\mathrm{corr}_{SE}}}. \qquad [4.15]$$

Table 4.1: Correlations between cost functions H_g and $H_{corr_{SE}}$ and weightings used the cost function $H=w_gH_g+w_{corr_{SE}}H_{corr_{SE}}$ for both the DMN ROI and OCCIP ROI.

ROI	ρ	w_g	$w_{corr_{SE}}$
DMN	0.84	0.775	0.225
OCCIP	0.49	0.818	0.182

From the 10,000 random coil arrays generated in this calibration study, the weights for the DMN and OCCIP ROIs are presented in Table 4.1. The linear correlation between the cost functions in Table 4.1, ρ=corr(H_g, $H_{corr_{SE}}$), is notably higher between the *g*-factor

and SENSE induced correlations for the DMN than that of the OCCIP ROI. This is because $H_{corr_{SE}}$ is considerably more variable than H_g for the OCCIP ROI by comparison to that of the DMN ROI. As such, the weighting of H_g through w_g for the OCCIP ROI is very high relative to $w_{corr_{SE}}$. While w_g for the DMN ROI is also much greater than $w_{corr_{SE}}$, the difference is not as great because the variability of $H_{corr_{SE}}$ is lower for the DMN ROI than that of the OCCIP ROI. If the selection of N_C, A, $J_{\phi/z}$ and the location of the ROI produced two cost functions that did not exhibit such a high correlation, the covariance term in Eq. [4.15] would be reduced and the weights would be primarily determined by the variances of the two cost functions.

4.3.3 Optimization with an Iterated Conditional Modes Algorithm

With the cost function weights in Table 4.1 inserted into Eq. [4.10], the arrays that minimized Eq. [4.10] for both the DMN and OCCIP ROIs were determined through a combination of a stochastic optimization approach and a deterministic Iterated Conditional Modes (ICM) optimization algorithm. Using the 10,000 arrays generated for both the DMN and OCCIP ROIs in the calibration process, the overall cost function in Eq. [4.10] was re-evaluated for each morphed array. From the 10,000 arrays, the N_{array}=15 arrays with the lowest overall cost were then inserted into the ICM algorithm in an attempt to further refine the optimization. When morphing an RF coil array with J_ϕ=5 and J_z=5 basis functions, the coefficient matrices, T_ϕ and T_z, comprise a total of 50 parameters to be optimized. The ICM algorithm is a deterministic algorithm that iteratively determines the configuration of the 50 parameters that maximizes the joint

probability of each parameter conditioned on the rest (Besag, 1986). For an arbitrary ROI, the ICM algorithm is performed using the following steps:

1) Generate a $J_\phi \times J_z$ array of initial coefficients for T_ϕ and a $J_\phi \times J_z$ array of initial coefficients for T_z.
2) Of the $2J_\phi J_z$ coefficients, vary the first coefficient over a grid of values while holding the other $2J_\phi J_z$ -1 coefficients constant.
3) Evaluate the cost function in Eq. [4.10] at each point on the grid in step 2).
4) Set the first coefficient to the value in 2) that minimized Eq. [4.10].
5) Move to the next coefficient.
6) Repeat steps 3)-5) until all coefficients have been individually optimized conditioned on the rest being held constant.
7) Refine the grid of values used in step 2).
8) Repeat steps 2)-7) until an appropriate level of convergence has been achieved.
9) Repeat steps 1)-8) for a total of N_{array} initial starting arrays, T_ϕ and T_z.

For both ROIs, the ICM algorithm was performed for the best N_{array}=15 initial starting arrays from the calibration trials. In each iteration, the coefficients were varied in step 2) by adding the starting value of the coefficient for that iteration to each of 10 values in a grid. For the first iteration, the 10 grid values varied uniformly between $-1/J_{\phi/z}$ and $1/J_{\phi/z}$, with the range incrementally reduced in each successive iteration. On average, the ICM algorithm reached convergence within 6 iterations of varying the 15 starting arrays. As the cost function in Eq. [4.10] is effectively defined over a 50-dimensional space, convergence to various local minima of Eq. [4.10] was achieved with the lowest of the 15 trials deemed the optimal coil geometry for this study. It is of note, however, that almost

all of the arrays that were subjected to the ICM algorithm resulted in geometries that shared the same basic design characteristics.

4.4 Results

Presented in Fig. 4.8 are the morphed arrays that were optimized for the DMN ROI. For a baseline comparison, the cost function in Eq. [4.10] was evaluated for imaging the DMN ROI using a conventional birdcage array in Fig. 4.8a. The overall cost produced by the birdcage array within the DMN ROI was H=0.332, which is a combination of an average g-factor cost of H_g=0.2987 and a SENSE induced correlation cost of $H_{corr_{SE}}$=0.4779. Presented in Fig. 4.8a is the g-factor profile throughout the center axial plane of the DMN ROI after a SENSE reconstruction with an acceleration factor of A=3, with the mean g-factor over each of the three regions of the DMN ROI within the center axial plane listed adjacent to the respective region. Of the 10,000 arrays generated in the calibration process, the array with the lowest overall g-factor in the DMN ROI is presented in Fig. 4.8b. For this array, the g-factor cost evaluated throughout the DMN ROI was H_g=0.2103, the cost of the SENSE induced correlation about the ROI was $H_{corr_{SE}}$=0.3748, and the combined cost of the array was H=0.2473. Upon observation, both the g-factor throughout the center plane of the DMN ROI and the mean g-factor within each of the three regions are noticeably lower than those of the birdcage array in Fig. 4.8a and the array with the lowest SENSE induced correlations in Fig. 4.8c. The combined vertical and horizontal deformations used to morph the array with a minimal g-factor is presented as a vector field under the unrolled morphed array in Fig. 4.8b. It is apparent that the anterior coil in red is still fairly rectangular in shape, such as that in the

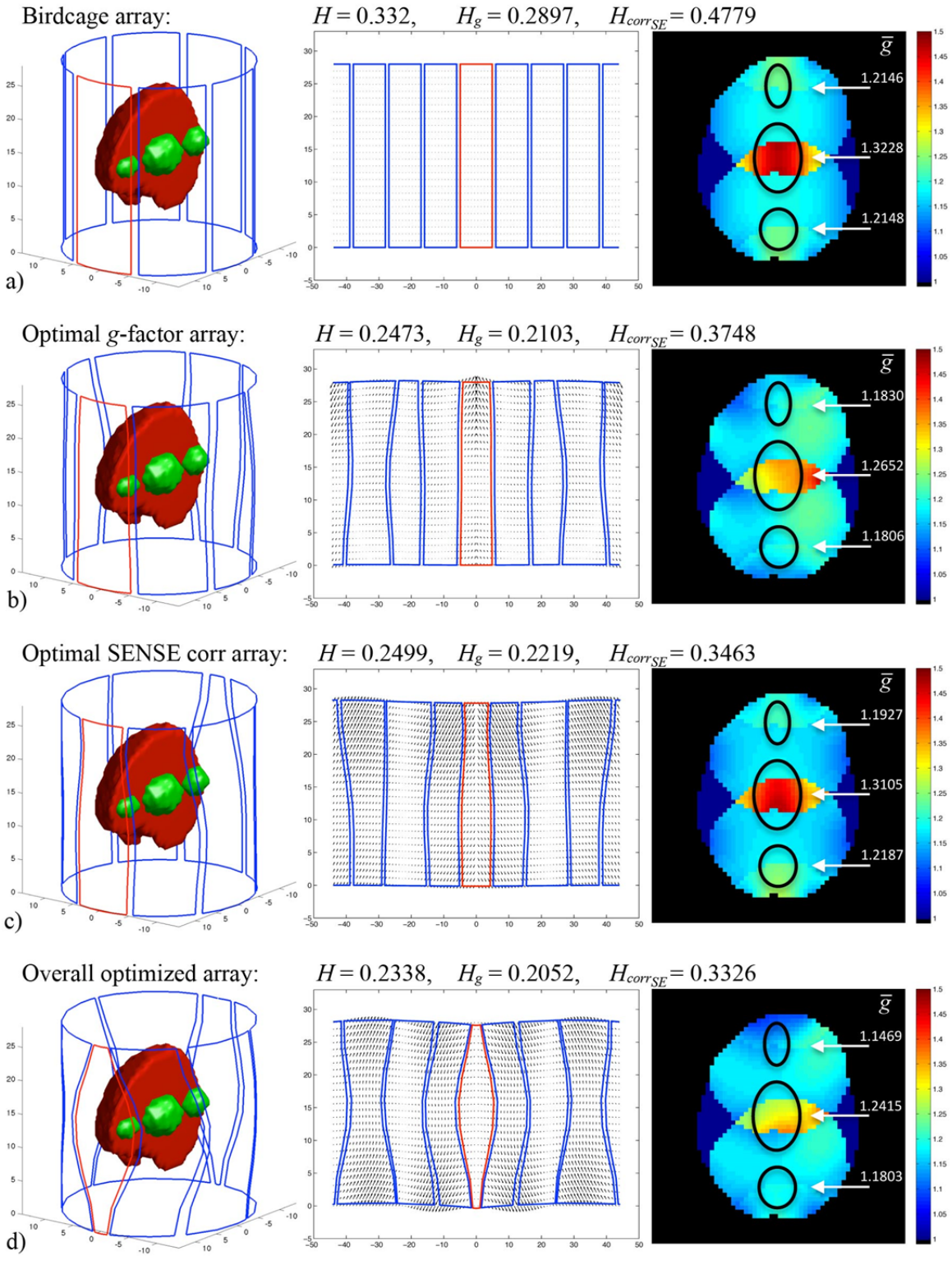

Figure 4.8: Coil geometry, spatial normalization deformation fields and the *g*-factor through the center axial plane of the DMN ROI for a) a birdcage array, arrays drawn from 10,000 random arrays in a calibration study that had b) a minimal *g*-factor cost, H_g, c) a minimal SENSE induced correlation cost, $H_{corr_{SE}}$, and d) an array derived through an ICM algorithm that minimizes the combined cost, H.

birdcage array in Fig. 4.8a, but the coils on the left and right as well as the anterior coil are all slightly wider in the center than at the top or bottom. Of the 10,000 calibration arrays, the array with the lowest overall SENSE induced correlation about the DMN ROI, $H_{corr_{SE}}$=0.3463, is presented in Fig. 4.8c, where the cost of the *g*-factor, H_g=0.2219, is slightly greater than the array with an optimal *g*-factor in Fig. 4.8b, but lower than the birdcage array in Fig. 4.8a. The deformation field that morphed the array to achieve a low overall SENSE induced correlation in Fig. 4.8c shows both anterior and posterior coils that are wider at the bottom than the top. Of the arrays that were subjected to the ICM algorithm, the array that simultaneously optimized the *g*-factor and SENSE induced correlations is presented in Fig. 4.8d. This array had an overall cost of H=0.2338, which is considerably lower than the conventional birdcage array in Fig. 4.8a, and also achieved lower costs for both the *g*-factor and SENSE induced correlations than those in Fig. 4.8b and Fig. 4.8c respectively. When comparing the *g*-factor through the center axial plane of the DMN ROI for the conventional birdcage array in Fig. 4.8a to that of the optimized array in Fig. 4.8d, it is apparent that the use of a conventional array with rectangular coils is not optimal for imaging the commonly investigated DMN ROI. An array with coils in the anterior and posterior that are wide in the center and very narrow near the top and bottom, and coils on the left and right that are narrower in the center than near the top and bottom clearly results in a lower *g*-factor throughout the DMN ROI, and the correlations induced by a SENSE reconstruction with A=3 are also significantly reduced.

Unlike the DMN ROI, the OCCIP ROI is only defined in one region in the anterior of the phantom, but becomes aliased with both the mid brain region and frontal lobe prior to a SENSE reconstruction with A=3. The arrays that were optimized for the

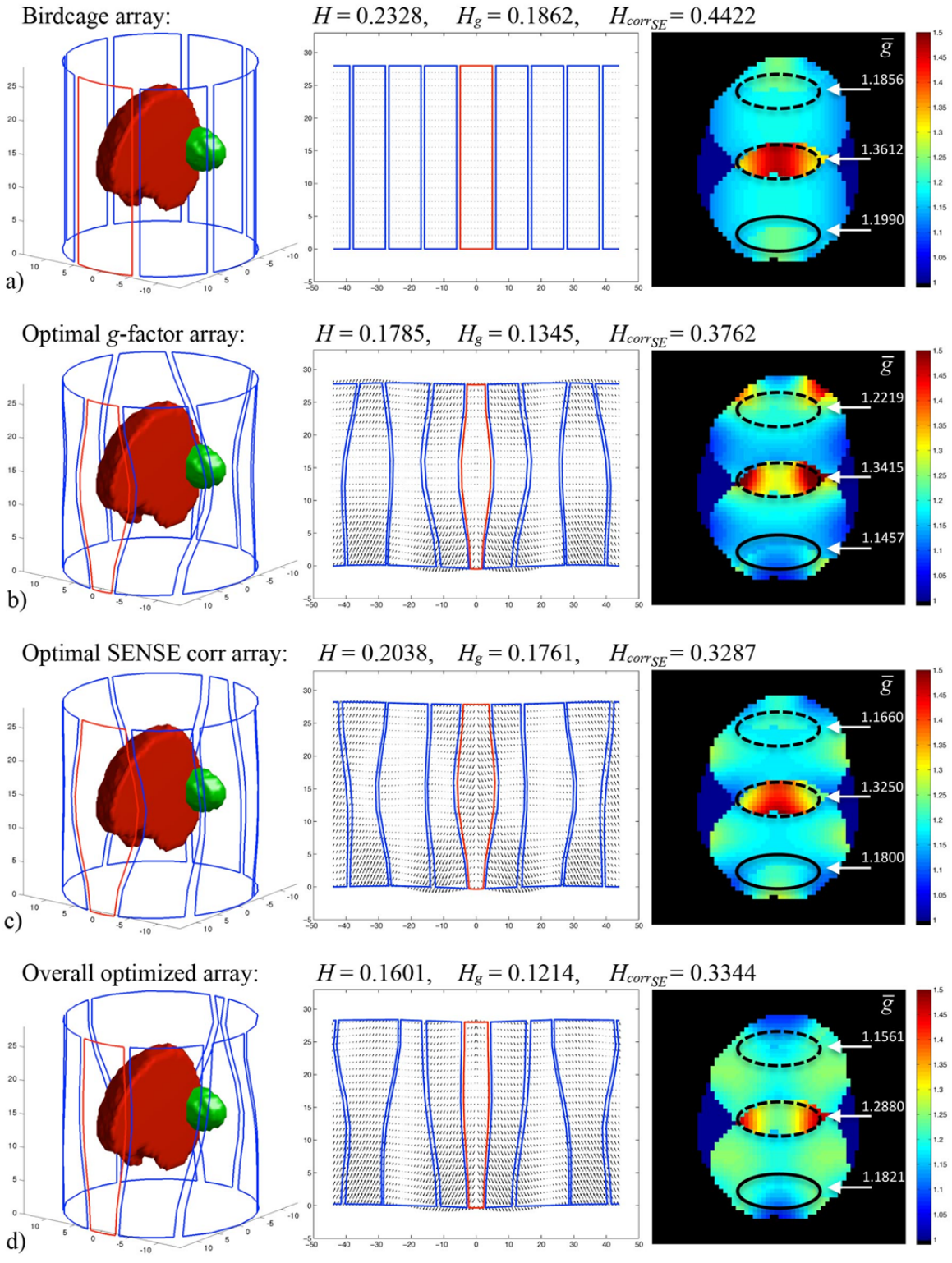

Figure 4.9: Coil geometry, spatial normalization deformation fields and the *g*-factor through the center axial plane of the OCCIP ROI for a) a birdcage array, arrays drawn from 10,000 random arrays in a calibration study that had b) a minimal *g*-factor cost, H_g, c) a minimal SENSE induced correlation cost, $H_{corr_{SE}}$, and d) an array derived through an ICM algorithm that minimizes the combined cost, H.

OCCIP ROI are presented in Fig. 4.9. The cost within the OCCIP ROI resulting from the use of a conventional birdcage array in Fig. 4.9a was estimated to be H=0.2328, with a g-factor cost of H_g=0.1862 and an overall SENSE induced correlation cost of $H_{corr_{SE}}$=0.4422. The g-factor throughout the center axial plane of the OCCIP ROI in Fig. 4.9a shows a mean g-factor within the ROI in the center plane to be 1.199, with the g-factor in the regions aliased with the ROI represented by dashed ovals. Of the 10,000 random arrays generated in the calibration study, the array with the lowest overall g-factor in the OCCIP ROI is presented in Fig. 4.9b. As the OCCIP ROI is in the posterior of the brain phantom, the anterior coil is narrowest in the center with the coils adjacent to the anterior coil wider in the center than near the top and bottom. Combined with a narrow posterior coil that is narrowest in the center, the overall cost of the g-factor for this array was H_g=0.1345, with the cost of the SENSE induced correlations being $H_{corr_{SE}}$=0.3762, and a combined cost of H=0.1785. It is of note in the g-factor throughout the center plane produced by the array in Fig. 4.9b that the mean g-factor within the OCCIP ROI itself is lower than that of any other array, but the mean g-factor within the regions aliased with the OCCIP ROI are not. Of the 10,000 random arrays generated in the calibration study, the array with the lowest overall SENSE induced correlation about the OCCIP ROI is presented in Fig. 4.9c. As with the array with a minimal g-factor in Fig. 4.9b, the coil in the anterior of the array in Fig. 4.9c is widest in the center and narrow near the top and bottom, but unlike the array with a minimal g-factor, the array with a minimal SENSE induced correlation also has a posterior coil that is widest in the center. This array resulted in an overall cost for the SENSE induced correlations of $H_{corr_{SE}}$=0.3287, with a g-factor cost of H_g=0.1761, and a combined cost of H=0.2038. Of

the arrays that were subjected to the ICM algorithm, the array that simultaneously optimized the *g*-factor and SENSE induced correlations in the OCCIP ROI is presented in Fig. 4.9d. This array had an overall cost of H=0.1601, which is considerably lower than the conventional birdcage array in Fig. 4.9a, and also achieved a lower *g*-factor cost than any other array in Fig. 4.9. Despite the mean *g*-factor in the center plane being lower within the OCCIP ROI in Fig. 4.9b than in Fig. 4.9d, the mean *g*-factor in the regions aliased with the ROI are lower for the array in Fig. 4.9d than any other array. To achieve such low *g*-factors and SENSE induced correlations in the OCCIP ROI, the array in Fig. 4.9d has very narrow anterior and posterior coils that are narrowest near the bottom, with coils adjacent to the anterior coil that are wider in the upper half than the lower half. It is interesting to note that the anterior coil becomes so narrow in the upper half that a bottleneck is formed, but as with the array optimized for the DMN ROI in Fig. 4.8d, the array that produced a favorable *g*-factor and SENSE induced correlation for the OCCIP ROI is by no means comprised of symmetric rectangular arrays.

4.5 Discussion

The use of multiple RF coils in a phased array has become common practice in fMRI and fcMRI studies where there are constraints on the spatial and temporal resolution of the data that can be acquired. In general, studies that develop RF coil arrays are predicated on two assumptions. First, the overarching goal of an optimized RF coil array is to achieve the maximum possible SNR throughout the image, and second, such a SNR results from using a symmetric array with coils that produce the most uniform B-fields throughout the volume. As almost all fMRI and fcMRI studies use generic RF coil arrays for imaging all regions of the brain, these two assumptions have appeared to be

justified. However, the increasing popularity of both fMRI and fcMRI has lead to many studies being performed on specific disorders that are associated with specific brain regions. As the human brain is not fully symmetric, and such regions of interest are not always in the very center, the assumption that RF coils need to be symmetric in traditional RF coil design studies are no longer fully justified. Additionally, with an estimation of correlations between brain regions being the mechanism for deducing regions with apparent functional connectivity, the fact that pMRI models such as SENSE induce artificial correlations between brain regions makes the use of maximizing the SNR as a sole optimization benchmark insufficient.

While the traditionally used *g*-factor and the correlations induced by the SENSE model are both functions of coil sensitivity profiles and the covariance between coils, the results outlined in this dissertation show that these two consequences of the SENSE un-aliasing process are not perfectly interconnected. The results of this study have illustrated through two different ROIs that the geometry of an RF coil array optimized for a minimal *g*-factor is not the same as the geometry of an RF coil array that induces a minimal correlation between voxels un-aliased by the SENSE model. It has been shown that a new cost function that combines the average *g*-factor in an ROI with a likelihood ratio test statistic for the degree to which the SENSE un-aliasing process induces a correlation about voxels in the ROI can be used to derive coil geometries that are more appropriate for fcMRI studies of the default mode network and the occipital lobe. Since the default mode network is a task-negative network, where functional activity is noted while a patient is at rest and is deactivated while the subject performs a task, the correlations induced by SENSE can make regions of the network appear to be activated when they are

not. As the occipital lobe becomes aliased with both the mid-brain and frontal lobe, any true cognitive activity within one of these regions could lead to false activation statistics within the other two regions due to the artificial correlations induced by SENSE between the three regions. In most fcMRI studies, an effort to reduce these correlations would be made through adjusted image reconstruction models, but the results of this dissertation indicate that the correlations induced about voxels in either of the two ROIs by the SENSE model can also be reduced with an adjustment to coil geometry. As such, studies that develop RF coil arrays for fMRI and fcMRI studies would be more effective when using a combined cost function, such as the one presented here.

Conventional birdcage arrays of rectangular receiver coils are mostly used to acquire images of the brain because the overlap of B-field sensitivities is relatively uniform and results in images with a uniform signal throughout the volume. Given that it is the overlap of coil B-fields that results in an amplification of noise in the SENSE reconstructed images, as measured through the *g*-factor, an ideal coil geometry would have B-field sensitivity profiles for each coil that resemble pieces of a pie, never overlapping and non-decreasing with distance from the coil. As such a geometry is almost impossible to achieve, there will always be an overlap of coil B-fields. For a birdcage array of rectangular coils that are all the same shape and size, these areas of overlap will be evenly spaced within an axial plane through the volume. However, with an individual coil's effective depth of sensitivity approximately equivalent to the coil's width, having coils of varying width and size can shift these areas of overlapping B-fields to different locations within the brain. By morphing a conventional birdcage array into different geometries, the results of this dissertation have indicated that a collection of

coils that vary in width can yield more optimal *g*-factor maps for a ROI in a specific location.

As more and more fcMRI studies are being conducted on patients with specific brain disorders, associated with specific brain regions, there is a natural need for purpose built coils. While the argument can be made that most patients will have brains differing in size and shape, an RF coil array designed through the methods outlined in this dissertation would be optimized for the general location of the ROI. Theoretically, a future study could be aimed at developing RF coils that are first optimized for general regions of the brain, but can be further deformed and optimized for specific patients. A study of that kind is well beyond the scope of this dissertation, but the principles outlined in this dissertation could be used for developing the initial array. Using spatial normalization with sine and cosine basis functions to morph a conventional birdcage array into an optimized geometry is a novel approach as it not only lowers the number of parameters to be optimized but also maintains "smoothness" between adjacent coils, preventing any overlap of coil edges. When morphing an array with spatial normalization is combined with the new cost function that simultaneously measures the *g*-factor and SENSE induced correlations, the RF coil geometries achievable through the methods outlined in this dissertation could achieve improved statistical properties in the images used in fcMRI studies by comparison to those achievable through conventional RF coil design approaches.

Chapter 5: Conclusion

Since the advent of noninvasive methodologies such as fMRI and fcMRI being used to observe cognitive brain activity, tremendous amounts of funding and effort have been devoted towards better understanding the human brain. Through mechanisms such as the BOLD contrast between oxygenated and deoxygenated hemoglobin, neuroscientists have been able to observe cognitive brain activity while a subject either performs a task in fMRI or remains at rest with fcMRI. As both fMRI and fcMRI make use of snapshot imaging techniques to observe fluctuations in the BOLD contrast in intervals on the order of 1-2 seconds, the acquired images generally have low spatial and temporal resolutions. To improve these resolutions, many studies have been aimed at devising methods of accelerating data acquisition through multi-coil pMRI techniques. Since the overarching goal in most of these studies is to accelerate data acquisition while maintaining a sufficient SNR, the statistical implications that image reconstruction with pMRI models can have on fMRI and fcMRI data are commonly overlooked. The work outlined in this dissertation has therefore been aimed at precisely quantifying the correlations that the two most commonly used pMRI reconstruction models, SENSE and GRAPPA, induce into the images that they reconstruct.

5.1 Summary of Presented Work

Most studies that explore the statistical implications of processing operations make use of time-consuming MCMC simulations that can only estimate the degree to which an operation changes the covariance structure of the acquired data. By representing each step necessary to carry out both the complex-valued SENSE and GRAPPA models

in terms of real-valued matrix operators, the degree to which the covariance of the originally acquired complex-valued data is modified by both individual operations and the collection of operations that comprise each model can be quantified both precisely and directly. Through the real-valued linear isomorphism of the complex-valued SENSE model derived in this dissertation, it has been shown that the process of un-aliasing a collection of aliased coil images into a full FOV composite image induces a correlation between voxels that were previously aliased. Through the real-valued linear isomorphism of the complex-valued GRAPPA model, it has been shown that the local correlation that the interpolation of missing spatial frequencies induces between spatial frequencies results in a global correlation between voxels after an inverse Fourier reconstruction. Since the GRAPPA model interpolates missing spatial frequencies using a truncated convolution kernel with weights derived from fully sampled coil sensitivities, these correlations are strongest in regions of the un-aliased image that were previously aliased, similar to those observed induced by the SENSE model. Unlike the SENSE model, however, there are additional low correlations induced by the GRAPPA model that exhibit a sinc structure within the rows and columns of the previously aliased voxels. When coupled with spatial filtering, as is commonly performed in most fMRI and fcMRI studies to improve the CNR, the correlations induced between previously aliased voxels by both the SENSE and GRAPPA models become spread to neighboring voxels in the vicinity of the previously aliased voxels.

The theoretical correlation structures induced by both the SENSE and GRAPPA models were validated through both theoretical MC simulations and experimentally acquired human subject data. The data reconstructed in the theoretical MC simulations

was generated with an identity covariance structure between voxels, and thus any correlations present between voxels of the reconstructed images would be a result of the two pMRI models. When estimated from the MC reconstructed time series, the theoretical correlations were clearly present both before and after the voxel time series were band pass filtered with a Hamming window to maintain frequencies between 0.01 and 0.08 Hz. These results suggested that if two previously uncorrelated voxels are spaced p_y/A apart when the PE direction is oriented as anterior/posterior in images reconstructed by the SENSE or GRAPPA models, the null hypothesis in an fcMRI study would be mistakenly rejected, assuming the voxels are functionally connected when they are not. In a time series of images acquired for a human subject, there is a true inherent covariance between voxels in the reconstructed images that fcMRI studies try to estimate and use to make inferences about functional connectivity. It was shown, however, that when two voxels are uncorrelated and spaced p_y/A apart in images that were fully sampled, that they become correlated when the same data set is reconstructed by SENSE and GRAPPA with A=3. As with the theoretical MC simulation, these correlations exceeded a threshold of ±0.35 (p≈0.05) after filtering each voxel's time series to the frequency spectrum commonly associated with functional connectivity. With the PE dimension oriented as anterior/posterior, these artificially induced non-biological correlations can align themselves with the commonly investigated default mode network. Similarly, if the PE dimension is oriented left/right, the artificially induced correlations will align themselves with the left and right hemispheres of the brain, potentially between regions such as the motor cortices. As both the default mode network and motor cortices are regions that are known to exhibit true biological correlations, the non-biological

correlations induced by the SENSE or GRAPPA models could either artificially accentuate or diminish these correlations, resulting in Type I or Type II errors in an fcMRI study.

Accounting for the correlations induced by the SENSE model could be performed through either improved reconstruction models or advances in MR hardware. As reconstruction models of this kind do not yet exist, the third component of this dissertation explored the degree to which informed RF coil designs could be used to improve the statistical implications of the SENSE model in specific brain regions. In conventional RF coil design studies, the *g*-factor is the de facto metric for optimization as it provides a measure of the SNR drop in SENSE reconstructed images. As both the *g*-factor and SENSE induced correlations are functions of coil B-field sensitivity profiles and the covariance between coils, they are both by definitions function of coil geometry. Through a novel application of a likelihood ratio test statistic for dependence between un-aliased voxels, a new cost function was derived for optimizing RF coils used to image specific regions of the brain with the SENSE model. A coil geometry that minimizes this cost function would not only exhibit a lower amplification of noise within an ROI, as measured through the *g*-factor, but would also have a reduced impact of SENSE induced correlations about the ROI when the reconstructed images are analyzed in an fcMRI study. To achieve such coil geometries, the constraints typically placed on coil symmetry were relaxed, and a conventional birdcage array of rectangular coils was morphed into optimal geometries using spatial normalization with a collection of sine and cosine basis functions. The proof of concept for such an optimization of RF coils was performed for both an ROI resembling the default mode network as well as an ROI within the occipital

lobe in a 3-dimensional human brain phantom. For both ROIs, it was shown that an array with a minimal *g*-factor does not necessarily have the same geometry as an array designed to minimize the correlations induced about the ROI by the SENSE reconstruction. The coil geometries that simultaneously minimized both the *g*-factor and SENSE induced correlations showed significantly improved statistics within the ROIs by comparison to those achievable through a conventional birdcage array. This suggests that while it may be convenient to use the same RF coil array for imaging all regions of the brain, such an array may not be optimal if the ROI is within a region that is aliased prior to a SENSE reconstruction. As most degenerative brain disorders are commonly associated with specific brain regions, it would therefore be more appropriate to make use of hardware that is purpose built for those regions.

5.2 Avenues of Future Work

5.2.1 Accounting for pMRI Induced Correlations

The real-valued linear isomorphisms presented in this dissertation for the complex-valued SENSE and GRAPPA models provide a perfect starting point for precisely quantifying the correlations induced by each model. At the very least, a neuroscientist or statistician analyzing fcMRI data that has been reconstructed with one of these pMRI models can use this framework to determine areas in which artificially induced non-biological correlations could result in misleading inferences. Ideally, pMRI models such as SENSE and GRAPPA would be able to accelerate data acquisition while simultaneously preserving the statistical properties of the acquired data. As such, future efforts could be devoted towards the development of new models that either induce lower

correlations or can simultaneously account for such correlations during the reconstruction process. Through Bayesian adaptations of either the SENSE or GRAPPA models, the artificially induced covariance structure, quantified through a framework such as the one presented in this dissertation, together with an estimate of the true covariance in fully sampled calibration data could be used as priors when reconstructing sub-sampled data. Such models would therefore be able to more accurately distinguish between correlations that are biological in nature and those that are artificially induced.

To further accelerate data acquisition, recent studies have developed "multi-band" image reconstruction models in which data acquisition is accelerated by simultaneously acquiring multiple slices of the volume at once. With models of this kind, the slice separation process induces correlations between voxels in the slice dimension, rather than in-plane correlations induced by models such as SENSE and GRAPPA. As such, it would be of interest to develop a linear isomorphism that can precisely quantify the correlations of multi-band methodologies (Rowe et al., 2013). Furthermore, more recent studies have combined multi-band imaging techniques with the traditional SENSE and GRAPPA models. With such a combination, the un-aliasing process would induce correlations both within each slice and between slices in a 3-dimensional structure. Artificially induced correlations with a structure of this kind can have significant implications in whole brain imaging where functional connectivity is estimated between all regions of the brain.

5.2.2 RF Coil Design

The methods outlined in the fourth chapter of this dissertation provide a novel means of using spatial normalization to derive RF coil geometries with optimized *g*-factor values and SENSE induced correlations within an ROI. The use of Biot-Savart to

estimate coil B-fields, however, is only applicable for coils used in lower field MRI scanners. As such, the use of a full-field electromagnetic solver, such as the HFSS software package, would be necessary for designing RF coils to be used in MRI scanners with higher field strengths. As fcMRI studies performed in different institutions will be conducted on patients in MRI scanners with a variety of field strengths, it would therefore be necessary for RF coils used for imaging a specific ROI to be optimized at each field strength. Additionally, the RF coil arrays presented in this dissertation made use of N_C=8 receiver coils for simplicity. As most current studies that employ pMRI techniques use phased arrays with anything up to 128 coils, it would be necessary to explore the statistical properties within an ROI of images reconstructed by SENSE with different numbers of coils. Moreover, the initial array morphed into optimal arrangements for the two ROIs in this dissertation used a single ring of rectangular coils placed around a cylinder, yet the idea can be adapted to morph either multiple tiers of coils placed above one another around a cylinder, or coils in a "soccer ball" shaped array. Finally, with each variation of coils designed for SENSE imaging in a specific ROI, the theoretical results of both this dissertation and future studies should be validated through the fabrication and application of a physical coil. Once a coil has been fabricated, the statistical properties within an ROI of both static phantoms and human subjects should be compared with those of a conventional birdcage array.

Appendix A: Estimation of the Coil and Voxel Covariance Structures

Consider a time series of N_{TR} complex-valued arrays of *k*-space that are $p_y \times p_x$ in dimension and acquired in each of N_C receiver coils. When sub-sampling is performed in the PE dimension by a factor of A, the data can be stored in a single array, K_C, that is $(p_y/A)\times p_x \times N_C \times N_{TR}$ in dimension. As the SENSE model is performed in the image domain, each $(p_y/A)\times p_x$ sub-sampled array in the N_C coils and N_{TR} TRs of the time series need to first be inverse Fourier reconstructed into an array of aliased images, Y_C, that is of the same dimension as K_C. To observe the covariance between voxels, the array Y_C is reshaped by stacking the rows of the $(p_y/A)\times p_x$ aliased image for each coil and each TR into vectors of length $(p_y/A)p_x$. The resulting array, V_C, is of dimension $(p_y p_x/A)\times N_C \times N_{TR}$ and ordered first by voxel, then by coil and finally by TR. In order to determine a real-valued representation of the complex-valued coil and voxel covariance structures, the real components of the aliased image vectors for all coils in V_C are stacked upon the imaginary components of the aliased image vectors for all coils in V_C, forming a real-valued array, V, that is of dimension $(p_y p_x/A)\times 2N_C \times N_{TR}$. The true covariance structure of a data array ordered in this fashion is $\Gamma = \Upsilon \otimes \Psi$, where Υ denotes the true covariance between voxels, and Ψ denotes the true covariance between coils. As the SENSE model typically assumes that there is no covariance structure between voxels in the reconstruction, the overall covariance of the data in V is simplified to $\Gamma = I_{rp} \otimes \Psi$, where $rp=(p_y p_x/A)$. This implies that the covariance between coils, Ψ, is the same for all voxels in the aliased images, and thus an initial estimate of Ψ can be achieved through

$$\hat{\Psi} = \frac{1}{N_{TR} \cdot rp} \sum_{t=1}^{N_{TR}} (V_t - \bar{V})^T I_{rp}^{-1} (V_t - \bar{V}). \qquad [A.1]$$

In Eq. [A.1], V_t denotes the $(p_y p_x/A)\times 2N_C$ array of aliased images, in real-valued vector form, for all N_C coils in the t^{th} TR, and $\bar{V}$ denotes the $(p_y p_x/A)\times 2N_C$ mean of V taken over the third dimension. With the array V organized in a real-valued form, with the real aliased voxel values for all coils stacked upon all imaginary aliased voxel values for all coils, the $2N_C\times 2N_C$ estimated coil covariance structure, $\hat{\Psi}$, in Eq. [A.1] is of the form

$$\hat{\Psi} = \begin{bmatrix} \hat{\Psi}_{RR} & \hat{\Psi}_{RI} \\ \hat{\Psi}_{IR} & \hat{\Psi}_{II} \end{bmatrix}. \qquad [A.2]$$

To observe the structure of the covariance structure in Eq. [A.2], $\hat{\Psi}$ was estimated from an experimental data set of a spherical phantom filled with an agar gel, acquired with N_C=8 coils, converted to a correlation matrix, and presented in Table A.1. While some studies may assume that $\hat{\Psi}$ is an identity matrix, it is apparent that the off-diagonal values presented in Table A.1 (and Table 2.1) are not zero, and thus the assumption that $\hat{\Psi}$ is an identity matrix cannot be made. When Ψ is estimated from complex-valued data and used in the complex-valued application of the SENSE model in Eq. [2.2], the structure in Eq. [A.2] is reformatted to being of the form

$$\hat{\hat{\Psi}} = \begin{bmatrix} \hat{\Psi}_{RR} & -\hat{\Psi}_{II} \\ \hat{\Psi}_{II} & \hat{\Psi}_{RR} \end{bmatrix}, \qquad [A.3]$$

where $\hat{\Psi}_{II}$ in Eq. [A.2] becomes $\hat{\Psi}_{RR}$, $\hat{\Psi}_{RI}$ in Eq. [A.2] becomes $-\hat{\Psi}_{II}$, and $\hat{\Psi}_{IR}$ in Eq. [A.2] becomes $\hat{\Psi}_{II}$. Based on the values in Table A.1, it is clear that the skew symmetric form of the covariance between coils in Eq. [A.3] is not the same as that estimated from real data, and thus a more accurate application of the SENSE model would employ the estimated covariance between coils in Eq. [A.2].

Table A.1: Coil correlation structure for a spherical agar phantom.

a) Correlation between real components of each coil (Ψ_{RR})

1	0.5804	-0.2306	-0.4294	0.212	0.133	0.0514	-0.1356
0.5804	1	0.0761	-0.5283	0.2969	0.2157	0.1433	0.0897
-0.2306	0.0761	1	-0.1689	0.3166	0.2146	0.2902	0.3102
-0.4294	-0.5283	-0.1689	1	-0.7171	-0.2353	0.2858	0.3901
0.212	0.2969	0.3166	-0.7171	1	0.4214	-0.2744	-0.3673
0.133	0.2157	0.2146	-0.2353	0.4214	1	0.2556	-0.365
0.0514	0.1433	0.2902	0.2858	-0.2744	0.2556	1	0.0414
-0.1356	0.0897	0.3102	0.3901	-0.3673	-0.365	0.0414	1

b) Correlation between imaginary components of each coil (Ψ_{II})

1	0.6508	0.0358	-0.4093	0.3945	0.3652	0.512	-0.4146
0.6508	1	0.2202	-0.55	0.3598	0.2584	0.397	-0.1637
0.0358	0.2202	1	0.0067	0.5803	0.5548	0.5023	0.0969
-0.4093	-0.55	0.0067	1	-0.0963	0.1701	0.1077	0.2011
0.3945	0.3598	0.5803	-0.0963	1	0.6803	0.4268	-0.2942
0.3652	0.2584	0.5548	0.1701	0.6803	1	0.6003	-0.2536
0.512	0.397	0.5023	0.1077	0.4268	0.6003	1	-0.3807
-0.4146	-0.1637	0.0969	0.2011	-0.2942	-0.2536	-0.3807	1

c) Correlation between real and imaginary components of each coil (Ψ_{RI})

0.0818	0.5241	0.5554	-0.0764	0.271	0.1971	0.2105	0.4473
-0.2906	0.0225	0.7617	0.0271	0.3325	0.2861	0.2049	0.3258
-0.5258	-0.7473	-0.009	0.7784	-0.1691	0.0438	-0.0735	0.3462
-0.1254	-0.1321	-0.7718	-0.3041	-0.6875	-0.6872	-0.587	0.0847
0.1001	-0.0353	0.4504	0.5238	0.471	0.6553	0.5654	-0.1971
0.1875	-0.0121	0.1825	0.2318	0.0359	0.2698	0.5223	-0.156
-0.136	-0.2451	-0.1278	0.0841	-0.3898	-0.4441	-0.118	0.4014
-0.7412	-0.5297	-0.2939	0.1013	-0.3829	-0.3757	-0.7552	0.4718

In addition to the inappropriate assumption that the covariance structure assumed by the complex-valued application of the SENSE model in Eq. [A.3] is equivalent to that in Eq. [A.2], the assumption that $\Upsilon = I_{rp}$ in Eq. [A.1] is also inappropriate. To illustrate that the acquired sub-sampled data does not have an identity voxel covariance structure,

the covariance between voxels can be found using the initial estimate of the covariance between coils in Eq. [A.1] by

$$\hat{\Upsilon} = \frac{1}{N_{TR} \cdot N_C} \sum_{t=1}^{N_{TR}} (V_t - \bar{V}) \hat{\Psi}^{-1} (V_t - \bar{V})^T . \qquad [A.4]$$

When $\Upsilon = I_{rp}$ is assumed, the covariance about the center voxel in an aliased image is presented in Fig. A.1a with A=1 and Fig. A.1b with A=3. When $\hat{\Upsilon}$ in Eq. [A.4] is estimated from a spherical phantom, the covariance estimated about the center voxel is presented in Fig. A.1c with A=1 and in Fig. A.1d with A=3. When comparing the estimated covariance structures in Figs. A.1a and A.1b to those in Figs. A.1c and A.1d, it is immediately apparent that the assumption of $\Upsilon = I_{rp}$ in Figs. A.1a and A.1b is inappropriate. To further validate that $\Upsilon \neq I_{rp}$, $\hat{\Upsilon}$ in Eq. [A.4] was also estimated from a human subject data set, and the covariance estimated about the center voxel of the human subject is presented in Fig. A.1e with A=1 and in Fig. A.1f with A=3. Once again, a

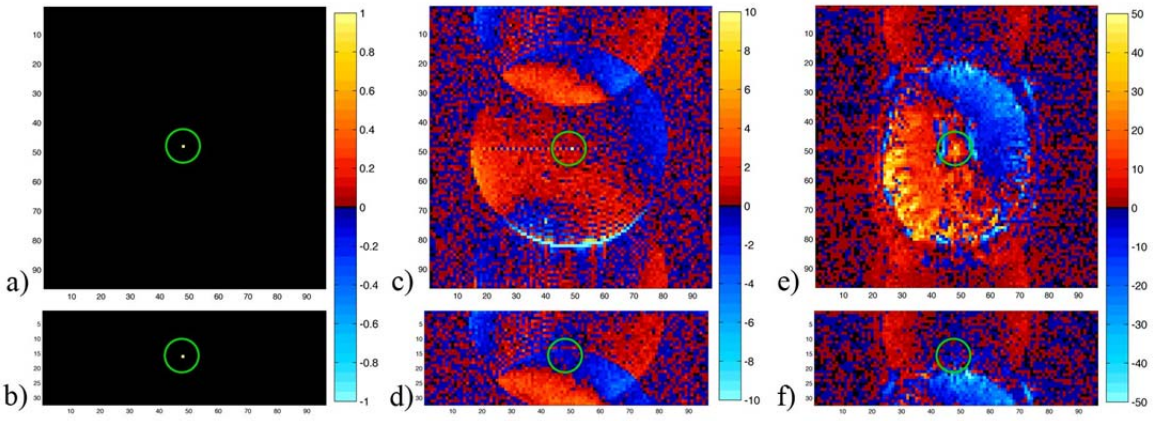

Figure A.1: An identity covariance, as assumed in the SENSE model, presented about the center voxel with a) A=1 and b) A=3, with the covariance estimated about the center voxel of a spherical phantom with c) A=1, and d) A=3, as well as the covariance estimated about the center voxel of a human subject with e) A=1 and f) A=3.

comparison between the identity covariance structures assumed in Figs. A.1a and A.1b to the estimated covariance structures for a human subject in Figs. A.1e and A.1f, illustrates that the assumption of $\Upsilon = I_{rp}$ in Figs. A.1a and A.1b is inappropriate.

As almost all applications of the SENSE model assume that $\Upsilon = I_{rp}$, and that the coil covariance structures in Eq. [A.2] and Eq. [A.3] are equivalent, a real-valued application of the complex-valued SENSE model for un-aliasing all voxels at once in Eq. [2.11] is

$$U = \left(S^T \left(I_{rp} \otimes \hat{\hat{\Psi}} \right)^{-1} S \right) S^T \left(I_{rp} \otimes \hat{\hat{\Psi}} \right)^{-1}. \qquad [A.5]$$

For a real-valued application of the complex-valued SENSE model for un-aliasing all voxels at once using coil and voxel covariance structures estimated from the data itself, Eq. [2.11] would be more appropriately defined by

$$U = \left(S^T \left(\hat{\Upsilon} \otimes \hat{\Psi} \right)^{-1} S \right) S^T \left(\hat{\Upsilon} \otimes \hat{\Psi} \right)^{-1}. \qquad [A.6]$$

The advantage of representing the SENSE unfolding operation in terms of the real-valued operator U in Eq. [2.11], Eq. [A.5] and Eq. [A.6] is that the un-aliasing process is performed on all aliased voxels in the aliased coil images at once, and more importantly, the correlations induced by that process can be precisely quantified. However, it is of note that the operator U in Eq. [A.5] is a block diagonal matrix with rp "unfolding" blocks of size $2A \times 2N_C$ along the diagonal. This is important because the matrix is very sparse and it allows for the SENSE un-aliasing process to be performed on a voxel-by-voxel basis if desired. While the assumptions in Eq. [A.6] are more mathematically correct than those in Eq. [A.5], the operator in Eq. [A.6] is a full matrix of size $2p_x p_y \times 2N_C(p_x p_y / A)$, and the only way in which a non-identity form of Υ can be applied is

through this formalism. To un-alias a 96×96 array of spatial frequencies, sub-sampled by a factor of A=2 in N_C=8 receiver coils, the unfolding matrix in Eq. [A.5] would be have 4608 diagonal blocks of size 4×16, and require 0.0003 GB of RAM to be stored in memory as a sparse array with double precision. By contrast, the full unfolding matrix in Eq. [A.6] would be 18432×73728 in dimension, and require 10.125 GB of RAM to be stored in memory as a full array with double precision. It has been shown in Bruce et al. (2012) that while Eq. [A.6] offers a more mathematically correct application of the SENSE model than under the typical assumptions in Eq. [A.5], the differences in the statistical properties of the reconstructed images are not significant enough to make the dramatic increase in computational resources worthwhile.

BIBLIOGRAPHY

Ashburner, J., Friston, K.J. Nonlinear spatial normalization using basis functions. Human Brain Map. 1999; 7: 24-266.

Assaf, M., Jagannathan, K., Calhoun, V.D., Miller, L., Stevens, M.C., Sahl, R., O'Boyle, J.G., Schiltz, R.T., Pearlson, G.D. Abnormal functional connectivity of default mode sub-networks in autism spectrum disorder patients. Neuroimage 2010; 53: 247-256.

Bandettini, P.A., Jesmanowicz, A., Wong, E.C., Hyde, J.S. Processing strategies for time course data sets in functional MRI of the human brain. Magn. Reson. Med. 1993; 30: 161–173.

Barry, R.L., Strother, S.C., Gore, J.C. Complex and magnitude-only preprocessing of 2D and 3D BOLD fMRI data at 7 T. Magn. Reson. Med. 2011; 3:867-871.

Bates, J., Granger, C. The combination of forecasts. Operations Research Quarterly 1969; 20: 451-468.

Berg, A.T., Shinnar, S., Levy, S.R., Testa, F.M. Newly diagnosed epilepsy in children: presentation at diagnosis. Epilepsia 1990; 40: 445-452.

Besag, J.E. On the statistical analysis of dirty pictures. J. of the Royal Stat. Soc. 1986; 48(3): 259-302.

Biswal, B., Yetkin, F.Z., Haughton, V.M., Hyde, J.S. Functional connectivity in the motor cortex of resting human brain using echo-planar MRI. Magn. Reson. Med. 1995; 34: 537-541.

Brau, A.C.S., Beatty, P.J., Skare, S., Bammer, R. Comparison of reconstruction accuracy and efficiency among autocalibrating data-driven parallel imaging methods. Magn. Reson. Med. 2008; 59: 382-395.

Breuer, F.A., Kannengiesser, S.A.R., Blaimer, M., Seiberlich, N., Jakob, P.M., Griswold, M.A. General formulation for quantitatice g-factor calculation in GRAPPA reconstruction. Magn. Reson. Med. 2009; 62: 739-746.

Broyd, S.J., Demanuele, C., Debener, S., Helps, S.K., James, C.J., Sonuga Barke, E.J. Default-mode brain dysfunction in mental disorders: a systematic review. Neurosci. Biobehav. Rev. 2009; 33: 279-296.

Bruce, I.P., Karaman, M.M, Rowe, D.B., A statistical examination of the SENSE reconstruction via an isomorphism representation. Magn. Reson. Imag. 2011; 29: 1267-1287.

Bruce, I.P., Karaman, M.M., Rowe, D.B. The SENSE-Isomorphism Theoretical Image Voxel Estimation (SENSE-ITIVE) model for reconstruction and observing statistical properties of reconstruction operators. Magn. Reson. Imaging. 2012; 30: 1143-1166.

Bruce, I. P., Rowe, D.B. Artificial correlations induced by SENSE and GRAPPA corrupt fcMRI conclusions. Intl. Proc. Magn. Reson. Med. 2013; 1229.

Bruce, I. P., Muftuler, L.T., Rowe, D.B. SENSE induced correlations are used to optimize RF coil design for specific fcMRI studies. Intl. Proc. Magn. Reson. Med. 2013; 2733.

Bruce, I. P., Muftuler, L.T., Rowe, D.B. Spatial normalization can morph RF coils into geometries optimized for fcMRI studies in specific brain regions. Intl. Proc. Magn. Reson. Med. 2014; 1328.

Bruce, I. P., Rowe, D.B. Quantifying the statistical impact of GRAPPA in fcMRI data with a real-valued isomorphism. IEEE Trans. Med. Imaging. 2014; 33(2): 495-503.

Buckner, R.L., Andrews-Hanna, J.R., Schacter, D.L. The brain's default mode network: anatomy, function, and relevance to disease. Ann. N.Y. Acad. Sci. 2008; 1124: 1-38.

Castelli, F., Frith, C., Happe, F., Frith, U. Autism, Asperger syndrome and brain mechanisms for the attribution of mental states to animated shapes. Brain 2002; 125: 1839-1849.

Chen, G., Muftuler, L.T., Ha, S.H., Nalcioglu, O. An optimization method for designing SENSE imaging RF coil arrays. J. Magn. Reson. 2007; 186: 273-281.

de Zwart, J.A., Ledden, P.J., Kellman, P., van Gelderen, P., Duyn, J.H. Design of a SENSE-optimized high-sensitivity MRI receive coil for brain imaging. Magn. Reson. Med. 2002; 47: 1218-1227.

Della-Maggiore, V., Chau, W., Peres-Neto, P., McIntosh A.R. An empirical comparison of SPM preprocessing parameters to the analysis of fMRI data. Neuroimage, 2002; 17: 19-28.

Deschpande, G., LaConte, S., Peltier, S., Hu, X. Integrated local correlation: A new method of local coherence in fMRI data. Human Brain mapping 2009; 30: 13-23.

Friston, K.J., Frith, C.D., Liddle, P.F., Frackowiak, R.S.J. Functional connectivity—The principal-component analysis of large (PET) data sets. J Cereb Blood Flow Metab 1993; 13: 5–14.

Firston, K.J., Ashburner, J., Frith, C.D., Poline, J.B., Heather, J.D., Frackowiak, R.S.J. Spatial registration and normalization of images. Human Brain Map. 1995; 5: 165-189.

Greicius, M.D., Krasnow, B., Reiss, A.L., Menon, V. Functional connectivity in the resting brain: A network analysis of the Default Mode hypothesis. PNAS, 2003; 100: 253-258.

Griffiths, D.J. Introduction to electrodynamics. Prentice Hall, 3rd Ed. 1999; 217.

Griswold, M.A. Advanced *k*-space techniques. Proc. 2nd Intl. Workshop Parallel Imag. Zurich, Switzerland, 2004; 16-18.

Griswold, M.A., Bruer, F., Blaimer, M., Kannengiesser, S., Heidemann, R.M., Mueller, M., Nittka, M., Jellus, V., Kiefer, B., Jakoob, P.M. Autocalibrated coil sensitivity estimation for parallel imaging. NMR Biomed. 2006; 19: 316-324.

Griswold, M.A., Jakob, P.M., Heidemann, R.M., Nittka, M., Jellus, V., Wang, J., Kiefer, B., Haase, A. Generalized Autocalibrating Partially Parallel Acquisitions (GRAPPA). Magn. Reson. Med. 2002; 47: 1202-1210.

Haacke, E.M., Brown, R., Thompson, M., Venkatesan, R. Magnetic resonance imaging: physical principles and sequence design. New York, NY, USA: John Wiley and Sons 1999.

Hahn, A.D., Nencka, A.S., Rowe, D.B. Improving robustness and reliability of phase-sensitive fMRI analysis using Temporal Off-resonance Alignment of Single-echo Timeseries (TOAST). Neuroimage 2009; 44: 742–752.

Hahn, A.D., Nencka, A.S., Rowe, D.B. Enhancing the utility of complex-valued functional magnetic resonance imaging detection of neurobiological processes through postacquisition estimation and correction of dynamic B_0 errors and motion. Human Brain Map. 2012; 33: 288-306.

Hahn, A.D., Rowe, D.B. Physiologic noise regression, motion regression, and TOAST dynamic field correction in complex-valued fMRI time series. Neuroimage 2012; 59: 2231-2240.

Heidermann, R.M., Griswold, M.A., Jakob, P.M. VD-AUTO-SMASH imaging. Magn. Reson. Med. 2001; 45: 1066-1074.

Huettel, S.A., Song, A.W., McCarthy, G. Functional magnetic resonance imaging. (2 ed.), Massachusetts: Sinauer, 2008.

Hyde, J.S., Jesmanowicz A., Froncisz W., Kneeland J.B., Grist T.M., Campagna N.F. Parallel image acquisition from noninteracting local coils. J. Magn. Reson. Med. 1986; 70: 512–517.

Jakob, P.M., Griswold, M.A., Edelman, R.R., Sodickson, D.K. AUTO-SMASH: a self calibrating technique for SMASH imaging. MAGMA 1998; 7: 42-54.

Jallon, P., Loiseau, P., Loiseau, J. Newly diagnosed unprovoked epileptic seizures: presentation at diagnosis in CAROLE study. Coordination Active du Peseau Observatoire Longitudinal de l' Epilepsie. Epilepsia 2001; 42: 464-475.

Jesmanowicz, A., Nencka, A.S., Li, S.J., Hyde, J.S. Two-axis acceleration of functional connectivity magnetic resonance imaging by parallel excitation of phase-tagged slices and half *k*-Space acceleration. Brain Connect 2011; 1: 81-90.

Just, M.A., Cherkassy, V.L., Keller, T.A., Minshew, N.J. Cortical activation and synchronization during sentence comprehension in high-functioning autism: evidence of underconnectivity. Brain 2004; 127: 1811-1821.

Just, M.A., Cherkassy, V.L., Keller, T.A., Kana, R.K., Minshew, N.J. Functional and anatomical cortical underconnectivity in autism: evidence from an FMRI study of an executive function task and corpus callosum morphometry. Cereb. Cortex 2007; 17: 951-961.

Jo, H.J., Saad, Z.S., Simmons, W.K., Milbury, L.A., Cox, R.W. Mapping sources of correlation in resting state fMRI, with artifact detection and removal. NeuroImage 2010; 52: 571-582.

Larkman, D.J., Nunes, R.G. Parallel magnetic resonance imaging. Phys Med. Biol. 2007; 52: 15-55.

Lauterbur P.C. Image formation by induced local interactions: Examples employing nuclear magnetic resonance. Nature 1973; 242: 190–191.

Lawrence, B.G., Crozier, S., Cowin, G., Yau, D.D. An inverse design of an open, head/neck RF coil for MRI. IEEE Trans. Biomed. Eng. 2002; 49: 1024-1030.

Loiseau, P., Duche, B., Loiseau, J. Classification of epilepsies and epileptic syndromes in two different samples of patients. Epilepsia 1991; 32: 303-309.

Lowe, M.J., Mock, B.J., Sorenson, J.A. Functional connectivity in single and multislice echoplanar imaging using resting-state fluctuations. Neuroimage 1998; 7: 119-132.

Lynch, C.J., Uddin, L.Q., Supekar, K., Khouzam, A., Phillips, J., Menon, V. Default Mode Network in children autism: Postermedial cortex heterogeneity and relationship with social deficits. Biol. Psych. 2013; 74: 212-219.

Manford, M., Hart, Y.M., Sander, J.W., Shorvon, S.D. National General Practice Study of Epilepsy (NGPSE): Partial seizure patterns in a general population. Neurology 1992; 42: 1911-1917.

Menon, R.S. Postacquisition Suppression of large-vessel BOLD signals in high-resolution fMRI. Magn. Reson. Med. 2002; 47: 1-9.

Muftuler, L.T., Chen, G., Hamamura, M.J., Ha, S.H. MREIT with SENSE acceleration using a dedicated RF coil design. Physiol. Meas. 2009; 30: 913-929.

Muftuler, L.T., Chen, G., Nalcioglu, O. An inverse method to design RF coil arrays optimized for SENSE imaging. Phys. Med. Biol. 2006; 51: 6475-6469.

Nencka, A.S., Hahn, A.D., Rowe, D.B. A Mathematical Model for Understanding STatistical effects of *k*-space (AMMUST-k) preprocessing on observed voxel measurements in fcMRI and fMRI. J. Neurosci. Meth. 2009; 181: 268–282.

Nencka, A.S., Hahn, A.D., Rowe, D.B. The use of three navigator echos in cartesian EPI reconstruction reduces Nyquist ghosting. Proc. Intl. Soc. Magn. Reson. Med. 2008; 16.

Nencka, A.S., Rowe, D.B. Image space correlations induced by k-space processes. Proceedings of the Organization for Human Brain Mapping, 2007; 13.

Ogawa, S., Menon, R. S., Tank, D. W., Kim, S. G., Merkle, H., Ellermann, J. M., Ugurbil, K. Functional brain mapping by blood oxygen level-dependent contrast magnetic resonance imaging. Biophysical Journal 1993; 64: 803–812.

Park, S., Park, J. Adaptive self-calibrating iterative GRAPPA reconstruction. Magn Reson Med. 2012; 67(6): 1721-1729.

Park, J., Zhang, Q., Jellus, V., Simonetti, O., LI, D. Artifact and noise suppression in GRAPPA imaging using Improved *k*-Space coil calibration and variable density sampling. Magn. Reson. Med. 2005; 53: 186-193.

Pruessmann, K.P., Weiger, M., Scheidegger, M.B., Boesiger, P. SENSE: Sensitivity Encoding for Fast MRI. Magn. Reson. Med. 1999; 42: 952–962.

Raichle, M.E., MacLeod, A.M., Snyder, A.Z., Powers, W.J., Gusnard, D.A., Shulman, G.L. A default mode of brain function. PNAS. 2001; 98(2): 676-682.

Raichle, M.E., Snyder, A.Z. A default mode of brain function: A brief history of an evolving idea. Neuroimage. 2007; 37: 1083-1090.

Roemer, P.B., Edelstein, A., Hayes, C.E., Souza, S.P., Mueller, O.M. The NMR phased array. Magn. Reson. Med. 1990; 16: 192-225.

Rowe, D.B. Significant fMRI neurologic synchrony using Monte Carlo methods. Monte Carlo Methods and Appl. 2003; 9(4): 267-285.

Rowe, D.B. Modeling both the magnitude and phase of complex-valued fMRI data. NeuroImage. NeuroImage 2005; 25: 1310-1324.

Rowe, D.B. Magnitude and phase signal detection in complex-valued fMRI data. Magn. Reson. Med. 2009; 62: 1356-1357.

Rowe, D.B., Logan, B.R. A complex way to compute fMRI activation. Neuroimage 2004; 23: 1078-1092.

Rowe, D.B., Logan, B.R. Complex fMRI analysis with unrestricted phase is equivalent to a magnitude-only model. Neuroimage 2005; 24: 603-606.

Rowe, D.B., Nencka, A.S., Hoffmann, R.G. Signal and noise of Fourier reconstructed fMRI data. J. Neurosci. Meth. 2007; 159: 361–369.

Rowe, D.B., Hahn, A.D., Nencka, A.S. Functional magnetic resonance imaging brain activation directly from *k*-space. Magn. Reson. Med. 2009; 27: 1370-1381.

Rowe, D.B., Nencka, A.S., Jesmanowicz, A., Hyde, J.S. Separation of two simultaneously encoded slices with a single coil. Intl. Proc. Magn. Reson. Med. 2013; 0123.

Sodickson, D.K., Manning, W.J. Simultaneous acquisition of spatial harmonics (SMASH): fast imaging with radiofrequency coil arrays. Magn. Reson. Med. 1999; 38: 591-603.

Spencer, M.D., Chura, L.R., Holt, R.J., Suckling, J., Calder, A.J., Bullmore, E.T., Baron-Cohen, S. Failure to deactivate the default mode network indicates a possible endophenotype of autism. Molec. Autism 2012; 3: 15.

Sporns, O., Tononi, G., Kötter, R. The human connectome: A structural description of the human brain. PLOS Comput. Biol. 2005; 1: e42.

Strother SC. Evaluating fMRI preprocessing pipelines. IEEE Eng. Med. Biol. Mag. 2006; 25: 27-41.

Taylor, I., Scheffer, I.E., Berkovic, S.F. Occipital epilepsies: identification of specific and newly recognized syndromes. Brain 2003; 126: 753-769.

Wang, S. SENSE performance of RF coil array at ultra-high fields. J. Med. Diagn. Meth. 2012; 1(2): 2168-9784.

Wang, Z., Wang, J., Detre, J.A. Improved data reconstruction method for GRAPPA. Magn. Reson. Med. 2005; 54: 738-742.

Weiger, M., Pruessmann, K.P., Leussler, C., Röschmann, P., Boesiger, P. Specific coil design for SENSE: A six-element cardiac array. Magn. Reson. Med. 2001; 45: 495-504.

Wooding, R.A. The multivariate distribution of complex normal variables. Biometrika 1956; 43: 212–215.

Xu, B., Wei, Q., Liu, F., Crozier, S. An inverse methodology for high-frequency RF coil design for MRI with de-emphasized B1 fields. IEEE Trans. Boimed. Eng. 2005; 52: 1582-1587.